Telecom-wavelength quantum memories in rare earth ion-doped materials for quantum repeaters

Falamarzi Askarani, Mohsen

DOI
10.4233/uuid:d418a98b-f2aa-4af3-b0e0-864875fcad2b

Publication date
2019

Document Version
Final published version

Citation (APA)
Falamarzi Askarani, M. (2019). *Telecom-wavelength quantum memories in rare earth ion-doped materials for quantum repeaters*. [Dissertation (TU Delft), Delft University of Technology]. https://doi.org/10.4233/uuid:d418a98b-f2aa-4af3-b0e0-864875fcad2b

TELECOM-WAVELENGTH QUANTUM MEMORIES IN RARE EARTH ION-DOPED MATERIALS FOR QUANTUM REPEATERS

Proefschrift

ter verkrijging van de graad van doctor
aan de Technische Universiteit Delft,
op gezag van de Rector Magnificus Prof.dr.ir. T.H.J.J. van der Hagen,
voorzitter van het College voor Promoties,
in het openbaar te verdedigen op woensdag 27 november 2019 om 10.00 uur

door

Mohsen FALAMARZI ASKARANI

Master of Science in Physics,
Sharif University of Technology, Tehran, Iran,
geboren te Esfahan, Iran.

Dit proefschrift is goedgekeurd door de promotoren.

Samenstelling promotiecommissie:

Rector Magnificus,	voorzitter
Prof. dr. W. Tittel,	Technische Universiteit Delft, promotor
Prof. dr. ir. R. Hanson,	Technische Universiteit Delft, promotor

Onafhankelijke leden:

Prof. dr. ir. L. M. K. Vandersypen	Technische Universiteit Delft
Prof. dr. S. D. C. Wehner	Technische Universiteit Delft
Prof. dr. ir. H. De Riedmatten	ICFO, Spanje
Prof. dr. P. Goldner	Institut de Recherche de Chimie Paris, Frankrijk

Printed by Gildeprint - Enschede

CONTENTS

1

INTRODUCTION

1.1. QUANTUM NETWORKS

Quantum networks [1, 2] are used to distribute entanglement among any set of its nodes. In such networks, quantum information is processed in computation nodes and transferred and distributed via communication channels. Optical fibres operating at telecommunication wavelength of around 1550 nm are appealing for the latter task due to their low transmission loss; rightly so, they are currently employed in classical networks. However, in a globe-spanning quantum network, transmission loss impedes quantum communication at distances exceeding a few hundred kilometers, thereby making a globe-spanning quantum network at a first glance impossible.

In current classical networks, distant nodes are linked by amplifying the transmitted signal at intermediate stations. This way, the intrinsic loss of the optical fibre can be overcome. Quantum states, on the other hand, cannot be perfectly copied or amplified, an instance of the famous No-Cloning Theorem [3]. Therefore, distributing quantum information over long distances requires a technology known as the quantum repeater [4].

Quantum repeater technology allows one to overcome the loss limitation by breaking down the whole distance span across the network into smaller, concatenated links, known as elementary links. These elementary links are designed such that entanglement, stored in their outer nodes, in two quantum memories [5], is heralded. Once all elementary links have established entanglement, operations can be performed such that entanglement is established between the outer nodes by entanglement swapping. Within an elementary link, when entanglement is generated, one of the states is stored in a quantum memory while the others are transmitted to measurement stations. Conditioned on a successful measurement, entanglement can be swapped between the stored states.

Thus, to realize a quantum repeater, the development of quantum memories is an indispensable task. Furthermore, to be compatible with telecom-wavelength communication channels, such memories should be desired to operate at such wavelength, and there are several strategies that can be employed to offer such compatibility. The first solution is to make use of quantum frequency conversion [6, 7], where the quantum memories work at a non telecommunication wavelength and the frequency converters are responsible for mapping the signals from memory wavelength to telecom-wavelength. The second is to use a wavelength non-degenerate entangled photon-pair source, in which one of the members of the generated photon-pair is at telecom wavelength and the other is compatible with the quantum memory; this makes use of a so-called absorptive quantum memory. The third, and most straightforward solution, at least theoretically speaking, is to build quantum memories compatible with telecom wavelength. In comparison, this seems to be the simplest as it does not demand the extra complexity required by both previous solutions. Furthermore, it underpins the development of all-telecom quantum networks, which could utilize cheap and off-the-shelf existing telecommunication equipments.

1.2. TELECOM-COMPATIBLE QUANTUM MEMORIES BASED ON RARE EARTH ION-DOPED MATERIALS

Rare earth ion-doped host materials are very promising to serve as quantum memories. They offer many interesting properties such as long optical and spin coherence time and broad absorption spectrum [8]. More interestingly, one of the rare earth ions, namely erbium, exhibits absorption at telecom-wavelength, a broad inhomogeneously-broadened absorption profile that can be tailored based on spectral hole burning [9, 10]. In addition, record optical coherence times exceeding 4 ms has been measured [11]. Therefore, an increasing amount of work has focused on the development of an erbium-based quantum memory.

In 2010, an erbium memory based on controlled reversible inhomogeneous broadening (CRIB) in a Er^{+3}:Y_2SiO_3 crystal has been reported by Lauritzen et al. with 0.25% efficiency and 600 ns storage time [12]. Using the same host material, Dajczgewand et al. showed a memory based on the revival of a silenced echo (ROSE) technique, with an efficiency of 30% and 16 μs storage time [13]. In 2015, quantum storage in an erbium-doped fibre, making use of the atomic frequency comb (AFC) technique, with 1% efficiency and a storage time of up to 50 ns [14] has been shown by our group. More recently, in 2019, AFC-based storage of qubits encoded into attenuated laser pulses has been reported using an Er^{+3}:Y_2SiO_3 nano-cavity with 0.2% efficiency and storage time of up to 10 μs [15].

Common to all of the above is the fact that none have simultaneously shown a quantum memory with high efficiency, long storage time, large storage bandwidth, and high fidelity. I would start saying that the efficiency in all studies was insufficient for creating workable quantum technology. It becomes clear that exploring other erbium-based materials and conducting more spectroscopic studies is highly required, which are two of the main topics of this work.

1.3. THESIS OVERVIEW

This thesis contains 7 chapters. In the presented chapter, I introduced the importance of telecom-compatible quantum memories. As briefly discussed, the only studied rare earth candidate for that is erbium in various materials. In the second chapter, I will describe the basic tools and knowledge required to understand the spectroscopic studies and quantum storage demonstrations. More specifically, I will discuss the concept of entanglement, its features and applications, various ensemble-based quantum memory protocols, and lastly, properties of rare earth ions and their related spectroscopic tools.

The third chapter contains my first spectroscopic study: it details optical decoherence and spectral diffusion in an erbium-doped silica glass fiber featuring long-lived spin sub-levels. In the fourth chapter, the use of an erbium-doped fibre as a quantum storage device in an entanglement distribution experiment is reported. In the fifth chapter, the second spectroscopic work is presented, which makes use of an erbium-doped crystal waveguide, and the sixth chapter describes a quantum storage demonstration using the same crystal waveguide. Lastly, I conclude my thesis and provide an outlook.

REFERENCES

[1] H. J. Kimble, *The quantum internet,* Nature **453**, 1023 (2008).

[2] S. Wehner, D. Elkouss, and R. Hanson, *Quantum internet: A vision for the road ahead,* Science **362**, eaam9288 (2018).

[3] W. K. Wootters and W. H. Zurek, *A single quantum cannot be cloned,* Nature **299**, 802 (1982).

[4] H.-J. Briegel, W. Dür, J. I. Cirac, and P. Zoller, *Quantum repeaters: the role of imperfect local operations in quantum communication,* Physical Review Letters **81**, 5932 (1998).

[5] A. I. Lvovsky, B. C. Sanders, and W. Tittel, *Optical quantum memory,* Nature photonics **3**, 706 (2009).

[6] B. Albrecht, P. Farrera, X. Fernandez-Gonzalvo, M. Cristiani, and H. De Riedmatten, *A waveguide frequency converter connecting rubidium-based quantum memories to the telecom c-band,* Nature communications **5**, 3376 (2014).

[7] A. Radnaev, Y. Dudin, R. Zhao, H. Jen, S. Jenkins, A. Kuzmich, and T. Kennedy, *A quantum memory with telecom-wavelength conversion,* Nature Physics **6**, 894 (2010).

[8] G. Liu and B. Jacquier, *Spectroscopic properties of rare earths in optical materials,* Vol. 83 (Springer Science & Business Media, 2006).

[9] R. M. Macfarlane, *High-resolution laser spectroscopy of rare-earth doped insulators: a personal perspective,* Journal of Luminescence **100**, 1 (2002).

[10] A. Szabo, *Observation of hole burning and cross relaxation effects in ruby,* Physical Review B **11**, 4512 (1975).

[11] T. Böttger, C. Thiel, R. Cone, and Y. Sun, *Effects of magnetic field orientation on optical decoherence in* Er^{3+}*:*Y_2SiO_5*,* Physical Review B **79**, 115104 (2009).

[12] B. Lauritzen, J. Minář, H. De Riedmatten, M. Afzelius, N. Sangouard, C. Simon, and N. Gisin, *Telecommunication-wavelength solid-state memory at the single photon level,* Physical Review Letters **104**, 080502 (2010).

[13] J. Dajczgewand, *Optical memory in an erbium doped crystal: efficiency, bandwidth and noise studies for quantum memory applications,* Ph.D. thesis, Université Paris-Saclay (2015).

[14] E. Saglamyurek, J. Jin, V. B. Verma, M. D. Shaw, F. Marsili, S. W. Nam, D. Oblak, and W. Tittel, *Quantum storage of entangled telecom-wavelength photons in an erbium-doped optical fibre,* Nature Photonics **9**, 83 (2015).

[15] I. Craiciu, M. Lei, J. Rochman, J. M. Kindem, J. G. Bartholomew, E. Miyazono, T. Zhong, N. Sinclair, and A. Faraon, *Nanophotonic quantum storage at telecommunications wavelength,* Physical Review Applied **12**, 024062 (2019).

2

BACKGROUND

In this chapter, first we detail the important optical properties of rare-earth ions in view of quantum memory. Second, we introduce several useful and widely-employed spectroscopic techniques, which are used for coherence measurements as well as lifetime measurements. The goal is to prepare the readers for the spectroscopic investigations described in chapters 3 and 5. Finally, we introduce essential elements for entanglement establishment in the view of quantum repeaters and then we discuss different quantum memory protocols and their characteristics to provide the necessary background for the quantum storage demonstrations reported in chapters 4 and 6.

Element	RE^{3+} ion	Electron configuration	Lowest energy level
^{21}Sc	Sc^{3+}	[Ar]$3d^0$	^{1}S$_0$
^{39}Y	Y^{3+}	[Kr]$4d^0$	^{1}S$_0$
^{57}La	La^{3+}	[Xe]$4f^0 5s^2 5p^6$	^{1}S$_0$
^{58}Ce	Ce^{3+}	[Xe]$4f^1 5s^2 5p^6$	^{2}F$_{5/2}$
^{59}Pr	Pr^{3+}	[Xe]$4f^2 5s^2 5p^6$	^{3}H$_4$
^{60}Nd	Nd^{3+}	[Xe]$4f^3 5s^2 5p^6$	^{4}I$_{9/2}$
^{61}Pm	Pm^{3+}	[Xe]$4f^4 5s^2 5p^6$	^{5}I$_4$
^{62}Sm	Sm^{3+}	[Xe]$4f^5 5s^2 5p^6$	^{6}H$_{5/2}$
^{63}Eu	Eu^{3+}	[Xe]$4f^6 5s^2 5p^6$	^{7}F$_0$
^{64}Gd	Gd^{3+}	[Xe]$4f^7 5s^2 5p^6$	^{8}S$_{7/2}$
^{65}Tb	Tb^{3+}	[Xe]$4f^8 5s^2 5p^6$	^{7}F$_6$
^{66}Dy	Dy^{3+}	[Xe]$4f^9 5s^2 5p^6$	^{6}H$_{15/2}$
^{67}Ho	Ho^{3+}	[Xe]$4f^{10} 5s^2 5p^6$	^{5}I$_8$
^{68}Er	Er^{3+}	[Xe]$4f^{11} 5s^2 5p^6$	^{4}I$_{15/2}$
^{69}Tm	Tm^{3+}	[Xe]$4f^{12} 5s^2 5p^6$	^{3}H$_6$
^{70}Yb	Yb^{3+}	[Xe]$4f^{13} 5s^2 5p^6$	^{2}F$_{7/2}$
^{71}Lu	Lu^{3+}	[Xe]$4f^{14} 5s^2 5p^6$	^{1}S$_0$

Table 2.1: Tripositive rare earth ions. The first column states the rare earth atoms with their atomic number. The electronic configurations are those for tripositive rare earth ions. Sc, Y, and Lu are triply ionized by taking electrons from $3d^1 4s^2$, $4d^1 5s^2$, and $5d^1 6s^2$ orbitals, respectively. All other ions are triply ionized by taking electrons from $4f^N 6s^2$ orbitals.

2.1. RARE EARTH ION-DOPED HOST MATERIALS

In the periodic table, the so-called *rare earth elements* correspond to the Lanthanides (starting from lanthanum (La) and ending with lutetium (Lu)) and also scandium (Sc) and yttrium (Y). Such elements, listed in Table. 2.1, are usually found as trivalent ions in naturally occurring minerals. The exceptional properties of rare-earth ions (REI) have led to extensive investigations of their applications in quantum technology [1, 2]. In particular, the long excited level lifetime of the optical transition in the $4f^N$ orbital is one of the unique properties of REIs.

In REIs, electrons in partially-filled $4f^N$ (N electrons) orbitals are well shielded from the surrounding environment by higher filled orbitals, namely $5S$ and $5P$, as illustrated in Fig. 2.1. These protected ions show interesting chemical and optical properties, which are very similar to those of free ions. One example of such properties is the typically narrow absorption linewidth of optical transitions of REIs.

2.1.1. ENERGY LEVEL STRUCTURE

The energy level structure of REIs, when doped into host materials, is a result of interactions between electron and nuclear spins exposed to internal and external fields in the host. The complete 4f-shell Hamiltonian of REIs is given by [1, 2]:

$$H = H_0 + H_C + H_{SO} + H_{CF} + H_{EZ} + H_{NZ} + H_Q + H_{HF} + H_{SHF}, \tag{2.1}$$

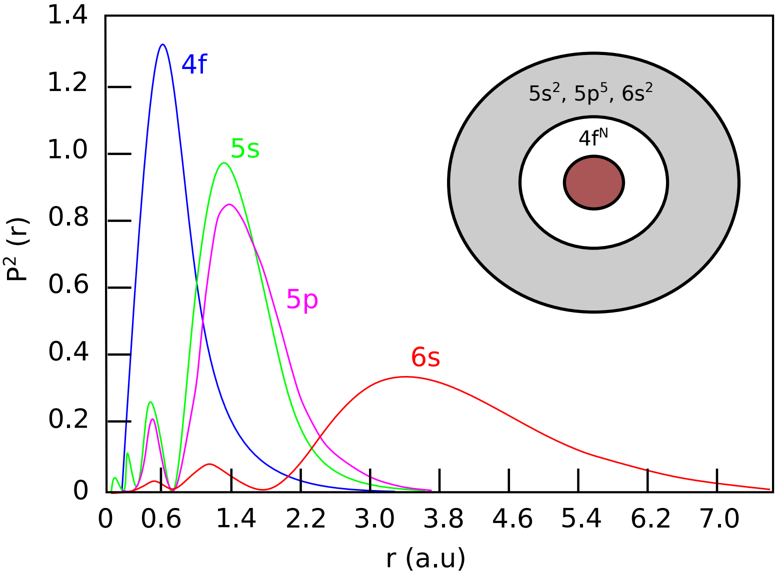

Figure 2.1: Radial charge densities for the electrons of the 4*s*, 5*p*, 5*s* and 6*s* shells for Gd^+, reproduced from [3]. Inset shows N electrons in the 4*s* shell, which are shielded by outer shells, namely 5*p* and 5*s*. 6*s* shell is an empty shell.

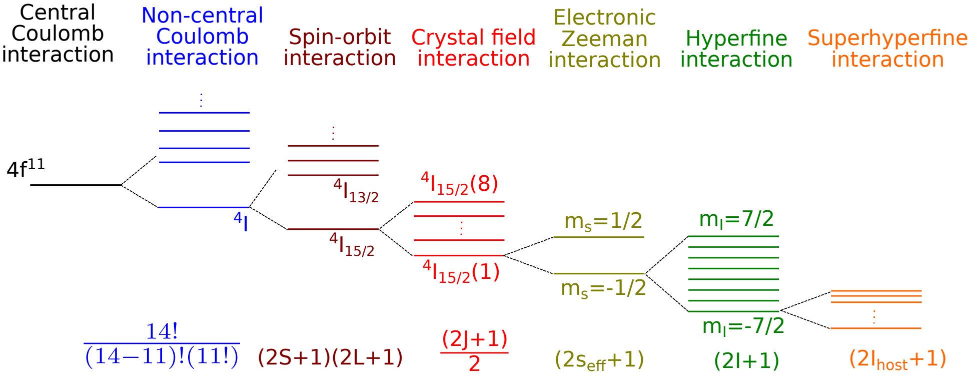

Figure 2.2: Level structure of erbium ions doped into a host material. Interactions and the number of levels for each group are stated.

where the Hamiltonian has been ordered from the strongest interaction (H_0) to the weakest interaction (H_{SHF}).

H_0 describes the kinetic energy and the potential energy, known as central Coulomb interaction, of all electrons around the nucleus. H_C represents the Coulomb repulsion between pairs of electrons, which is known as non-central Coulomb interaction. The former explains the degeneracy (n=4) of the $4f^N$ level whereas the latter is responsible for breaking this degeneracy into 14!/(14-N)!N! levels. It is noteworthy that there is an exception to this rule, namely Lu^{3+} since N is equal to 14 for its $4f^N$ orbital. The resultant levels are labeled as ${}^{2S+1}L$ (L and S, respectively, are total orbital angular momentum and total spin angular momentum), each of which is also (2S+1)(2L+1)-fold degenerate. H_{SO} ($H_{SO} \propto \vec{L}.\vec{S}$) represents spin-orbit coupling, which results from the interaction between the spin of the electron and the magnetic field generated by the orbit of the electron around the nucleus; the spin-orbit coupling splits ${}^{2S+1}L$ levels into J manifolds, also referred to as J multiplets, commonly written as ${}^{2S+1}L_J$, where S, L, and J are spin, orbital and total angular momentum, respectively. The term $H_0 + H_C + H_{SO}$ is usually referred to as free-ion Hamiltonian.

The first externally-imposed interaction is described by the H_{CF} term, the crystal-field Hamiltonian. This term expresses the interaction between the electrons and the electrostatic crystal fields created in the host, which leads to a further breaking of the degeneracy of each J multiplet. The resulting levels are known as crystal-field levels or Stark levels. The number of crystal field levels for the so-called non-Kramers ions, ions with even number of electrons, is $2J+1$. For Kramers ions, ions with an odd number of electrons, it is $(2J+1)/2$. In the case of Kramers ions, each of these levels is doubly-degenerate. In this thesis, we have studied erbium ions, which are Kramers ions.

H_{EZ} ($H_{EZ} \propto \vec{B} \cdot \vec{S}$, where $\vec{B}$ and $\vec{S}$ are the external magnetic field and the electronic spin, respectively) represents the electronic Zeeman interaction, i.e. the interaction between the spin of the electron and an externally applied magnetic field. H_{NZ} ($H_{NZ} \propto \vec{B} \cdot \vec{I}$, where $\vec{I}$ is the nuclear spin) is the nuclear Zeeman interaction due to the interaction between the nuclear spin and an externally applied magnetic field. Non-Kramers ions exhibit an enhancement in the nuclear Zeeman interaction, also known as pseudo-nuclear Zeeman interaction, which is due to a second-order perturbation created by the electronic Zeeman and hyperfine interactions [4].

H_Q ($H_Q \propto \vec{Q} \cdot \vec{L}$) is referred to as the quadruple interaction, an effect on nuclei with spin ($I \geq 1$), caused by the interaction between the electron momentum ($\vec{L}$) and the nuclear quadruple momentum ($\vec{Q}$). H_{HF} ($H_{HF} \propto \vec{S} \cdot \vec{I}$) and H_{SHF} ($H_{SHF} \propto \vec{S} \cdot \vec{I_{host}}$) are hyperfine and superhyperfine interactions, respectively. The former is caused by the interaction between the nuclear spin and the magnetic field generated by the spin of the electron. The latter is due to the interaction between the electronic spin of the ion and the surrounding magnetic field produced by the nuclear spin of the host element. In Fig. 2.2, the energy level structure of erbium ions doped into a host material, where each of the above-mentioned interactions is identified, is depicted.

2.1.2. HOMOGENEOUS AND INHOMOGENEOUS LINEWIDTH

Homogeneous linewidth

The energy-time uncertainty principle

$$\Delta E \times \Delta t \geq \frac{\hbar}{2} \tag{2.2}$$

states that the finite population lifetime (T_1) of an atomic state results in a finite spectral emission, or absorption line. This so-called intrinsic homogeneous linewidth (Γ_h) is defined as the spectral linewidth inside which an ion can absorb or emit radiation. In a perfect crystal, where all the ions are under identical conditions, the entire absorption spectrum would fall within one homogeneous linewidth, as depicted in Fig. 2.4a.

Noteworthy is the fact that the intrinsic homogeneous linewidth of an ion is associated to its coherence time (T_2), through a Fourier relation, given by

$$\Gamma_h = \frac{1}{\pi T_2}. \tag{2.3}$$

The upper bound of the coherence time is given by two times the population lifetime: $T_2 = 2T_1$ [2]. However, in practice, coherence times are usually smaller, i.e. $T_2 \leq 2T_1$, an effect of decoherence. The corresponding linewidth of the degraded coherence time is usually referred to as effective homogeneous linewidth ($\Gamma_{h(eff)}$) or homogeneously-broadened line. Hence, the effective homogeneous linewidth is given by

$$\Gamma_{h(eff)} = \frac{1}{2\pi T_1} + \frac{1}{2\pi T_2^*}, \tag{2.4}$$

where T_2^* is the pure dephasing time.

Homogeneous broadening: causes

The population lifetime-limited homogeneous linewidth is usually broadened by the environment's dynamical processes (decoherence). The optical transition frequencies of the REIs experience shift due to the environmental fluctuations caused by different processes such as spin-spin, spin-phonon, and spin-host interactions. The time-dependent random shift of the transition frequency of an ion by its surrounding environment is defined as spectral diffusion; spectral diffusion, therefore, yields homogeneous broadening and an effective homogeneous linewidth.

The dynamical processes contributing to the broadening of the REIs homogeneous linewidth [5–7] are given in the following equation.

$$\Gamma_{h(eff)} = \Gamma_{population} + \Gamma_{spin-spin} + \Gamma_{spin-phonon/TLS} + \Gamma_{spin-host} + \Gamma_{ISD}. \tag{2.5}$$

The first term, $\Gamma_{population} = \frac{1}{2\pi T_1}$, as discussed above, is the intrinsic cause of broadening. $\Gamma_{spin-spin}$ refers to the mutual spin-flip coupling (spin flip-flops), which may be either electronic spin-spin or nuclear spin-spin couplings. When two neighboring spins are resonant, the energy between them can be exchanged (an exchange often mediated by magnetic-dipole interaction) and a spin flip-flop occurs. An exception can also happen when two neighboring electronic or nuclear spins are not resonant and the energy difference between these two is supplied by a host nuclear spin. This effect causes fluctuations in the magnetic field of the environment surrounding the ions and results in linewidth broadening. Electronic spin flip-flops are usually one of the detrimental effects of coherence in Er-doped materials since erbium ions have a large magnetic dipole moment. In Tm-doped materials, on the other hand, electronic spin flip-flops are nonexistent since thulium ions have a quenched electronic spin; instead, nuclear spin flip-flops emerge as a cause of linewidth broadening.

There are methods to minimize the occurrence of spin flip-flops. Choosing a host material with a low concentration of REIs figures as one of them; a low concentration equates to an increased distance between neighboring ions, which, in turn, diminishes the strength of the interaction between their electronic and nuclear spins. This is due to the fact that the magnetic dipole-dipole interaction is inversely proportional to the distance cubed. The second option is to choose a host material whose elements feature zero or small nuclear magnetic moments. Finally, a third option is to apply a strong external magnetic field, which prevents the spin flipping by collectively polarizing the spins.

In Eq. 2.5, $\Gamma_{spin-phonon/TLS}$ is the coupling between phonons and REIs, which causes spin flips driven by phonons; phonons are the well-known lattice vibrational modes, which, in an amorphous lattice, are replaced by localized vibrational modes. Such modes exhibit a double-well potential structure and, therefore, are usually treated as two level systems (TLSs). Phonons can be absorbed, emitted, or scattered by ions, and various transitions can be coupled to phonons through different processes. These include the direct phonon process, the resonant two-phonon (Orbach) process, and the off-resonant two-phonon (Raman) process. At low temperatures, the number of available phonons at a specific energy is given by $exp(-\hbar\omega/K_B T)$, the Bose-Einstein distribution; at the same time, the phononic density of state at a given energy scales with ω^2 (here, $\hbar$, ω, K_B, and T are the Planck constant, phonon frequency, the Boltzmann constant, and temperature in Kelvin, respectively). Therefore, electronic spin transitions with small energy splittings are less prone to direct phonon coupling than those with large energy splittings, since the phonon density of states is much smaller. Nevertheless, the remaining two-phonon processes can still be detrimental.

In order to mitigate the effect of spin-photon coupling, an obvious solution is to reduce the temperature. Another trivial solution, in the case of electronic Zeeman levels, is to increase the applied magnetic field. However, as the magnetic field increases, the energy splitting of Zeeman levels also increases; this results in an increase in the phonon density of states. Interestingly, for relatively high magnetic fields, even though the photonic density of states is large, there are no phonons with such energy to occupy said energy levels [8]. Hence, such a situation could allow one to exclude the effect of phonon-driven spin flips [8].

The fourth term of Eq. 2.5, $\Gamma_{spin-host}$, represents two different effects; one is caused by the interaction between nuclear spins of REIs and host nuclear spins (host nuclear spin-REIs nuclear spin flip-flops) and the other is caused by host nuclear spin flips . The latter is either driven by phonons in crystals, TLSs in glassy materials, or another host nuclear spin (host nuclear spin flip-flops). Both effects lead to shifts in the transition frequency of REIs (linewidth broadening). These host nuclear spin flips may occur in hosts

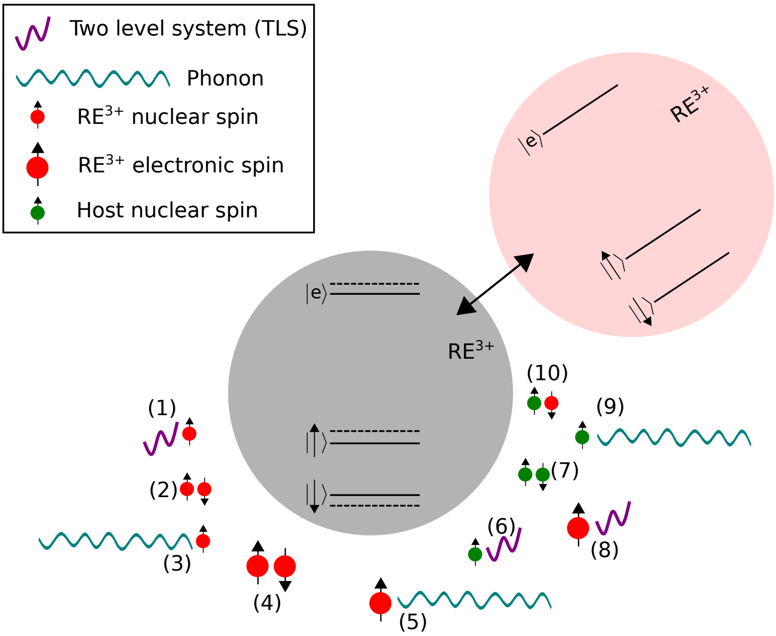

Figure 2.3: Schematic of dynamic processes affecting the homogeneous linewidth of REIs both in ordered and disordered host materials. The shifted transition frequencies of RE^{3+} in the gray circle, caused by spectral diffusion, have different sources, numbered from (1) to (10), as described in the text. The black arrow indicates the effect of ISD caused by neighboring, optically-excited RE^{3+}, shown in the pink circle, mediated by electric dipole interaction whereas the mechanisms numbered from (1) to (10) are mediated by magnetic dipole interaction. Big and small red circles represent nuclear and electronic spins of surrounding REIs and small green circles indicate nuclear spin of host ions. (1) to (10) represent, in order: nuclear spin flips driven by TLS; nuclear spin flip-flops; nuclear spin flips driven by phonons; electronic spin flip-flops; electronic spin flips driven by phonon; host nuclear spin flips driven by TLS; host nuclear spin flip-flop; electronic spin flips driven by TLS; host nuclear spin flips driven by phonons; and host nuclear spin-RE^{3+} nuclear spin flip-flops.

if the dopants are sufficiently strongly coupled to each other, e.g. lithium and niobium nuclear spins in a lithium niobate host crystal. Γ_{ISD}, which can also be identified as ion-ion interaction, represents the contribution of instantaneous spectral diffusion (ISD) [2], an intensity-induced decoherence effect, to the linewidth broadening. To understand the basic principle of ISD, it is useful to consider a simple case where two nearby ions (ion 1, with dipole moment of μ_1, and ion 2, with μ_2) are in their respective ground states and are coupled via dipole-dipole interaction, which is proportional to $\mu_1 \cdot \mu_2$. When one of them (say ion 2) is excited, it acquires an altered dipole moment due to the different g-factor of the excited state and the ground state. Hence, the initial dipole-dipole interaction is modified to $\mu_1 \cdot \mu_2^{'}$ ($\mu_2^{'}$ is the dipole moment of ion 2 in the excited state). This results in a shift in the transition frequency of ion 1, leading to the broadening of the homogeneous linewidth of ion 1. A low concentration host material can significantly diminish the influence of ISD by increasing the distance between neighboring ions and, thereby, decreasing the strength of ion-ion interaction.

A schematic of all above-mentioned dynamical processes is depicted in Fig 2.3. Note

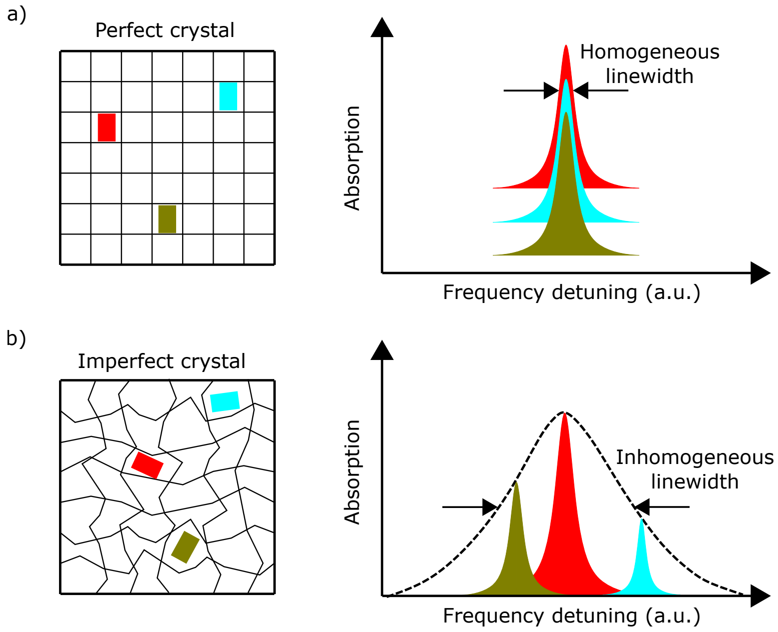

Figure 2.4: a) Homogeneous linewidth: absorption profile of a perfect crystal doped with REIs. b) Inhomogeneous linewidth: absorption profile of an imperfect crystal doped with REIs. The imperfections may be caused by, for example, stress and strain in the host crystal. The extreme case of an imperfect crystal can be seen as an amorphous lattice that possesses a large inhomogeneous linewidth. The figure is reproduced from [10].

that $\Gamma_{spin-spin}$ and $\Gamma_{spin-phonon}$ processes also affect lifetimes and coherence times of the ground state spin sub-levels; these processes are known as spin cross-relaxation [8] and spin-lattice relaxation [9], respectively.

Inhomogeneous linewidth

Static process, such as strain, stress, and defects lead to a slightly different local environment experienced by each ion in the host; this results in a different homogeneously-broadened absorption line for each ion and hence, inhomogeneous broadening. The inhomogeneously-broadened absorption profile, shown in Fig. 2.4b, is a summation over homogeneous linewidths of all the ions with slightly shifted central frequencies. It is worthwhile mentioning that these static processes are not decoherence processes. Inhomogeneous broadening in REI-doped host materials varies between a few hundreds of MHz up to a few THz, depending on the amount of disorder in the host material. Inhomogeneous broadening is advantageous in some photon-echo based quantum memory protocols, namely the atomic frequency comb (AFC) protocol, since it allows broadband quantum memories. Any electric field-sensitive spin transition can also be affected by the above-mentioned static processes and undergoes broadening, which can be seen as spin inhomogeneous broadening. However, such broadening is usually on a smaller scale compared to optical inhomogeneous broadening.

2.1.3. TWO- AND THREE-PULSE PHOTON ECHO

Decoherence and relaxation dynamics reduce optical coherence times and spin level' lifetimes, respectively. The former occurs on a shorter timescale, usually on the order of $> \mu$s, whereas the latter occurs on a longer timescale, usually on the order of > ms. Two commonly-used spectroscopic techniques, namely two-pulse photon echo (2PPE) and three-pulse photon echo (3PPE) [2, 11], are generally employed to diagnose shorter and longer timescale dynamics, respectively.

Two-pulse photon echo

In 2PPE, an optical $\Pi/2$ pulse initially excites the atoms into a superposition of the ground and excited state (an atomic coherence). During the following waiting time, the atoms start to dephase, due to the optical inhomogeneous broadening. After the waiting time, an optical Π pulse rotates the atomic dipole moments by 180 degrees, which reverses the phase evolution of the atoms. Hence, after a free evolution time that is equal to the time difference between the first and second pulse, complete rephasing happens and a coherent emission is emitted, known as a photon echo (see Fig.2.5). The photon echo intensity decays exponentially with the waiting time. The time over which the coherence decays to $1/e^2$ of its initial value determines the coherence time. In practice, this decay often becomes non-exponential [12], which is due to the time-dependent decoherence effect, spectral diffusion.

Three-pulse photon echo

In 3PPE, which is a modified 2PPE, three optical $\Pi/2$ pulses are used. The first two pulses create a population grating (a spectrally periodic structure) in the ground and excited state, and the third pulse stimulates the coherent emission, the photon echo. The 3PPE pulse sequence and its Bloch sphere representation are illustrated in Fig. 2.6. Unlike 2PPE, which gives information about coherence time, 3PEE is generally used to assess spectral diffusion and hence, coherence on a large time scale. Additionally, excited level lifetime and lifetimes of any present long-lived spin levels are extracted through 3PPE measurements.

A detailed description and application of 2PPE and 3PPE in the example of an erbium-doped fibre is discussed in chapter 3.

2.1.4. SPECTRAL HOLE BURNING

One of the well-known experimental techniques to perform optical and spin spectroscopy is spectral hole burning [13, 14]. Typically, this technique is employed to measure lifetimes of different levels or to study energy level difference. In addition, by means of spectral hole burning, any spectral features can be created. The way spectral hole burning works is simple. When a spectrally narrow laser (referred to as burning laser or pump laser), held at a fixed frequency, is shone on a medium with an inhomogeneously-broadened absorption spectrum, a spectrally narrow subset of atoms is excited and a spectral hole is created. The modified absorption spectrum can be probed using a tunable laser yielding the area, width or depth of the hole. The laser in this step is referred to as scanning laser. The measured area of the burnt hole decays exponentially with the increasing waiting time. The time over which the hole area decreases to $\frac{1}{e}$ of its initial

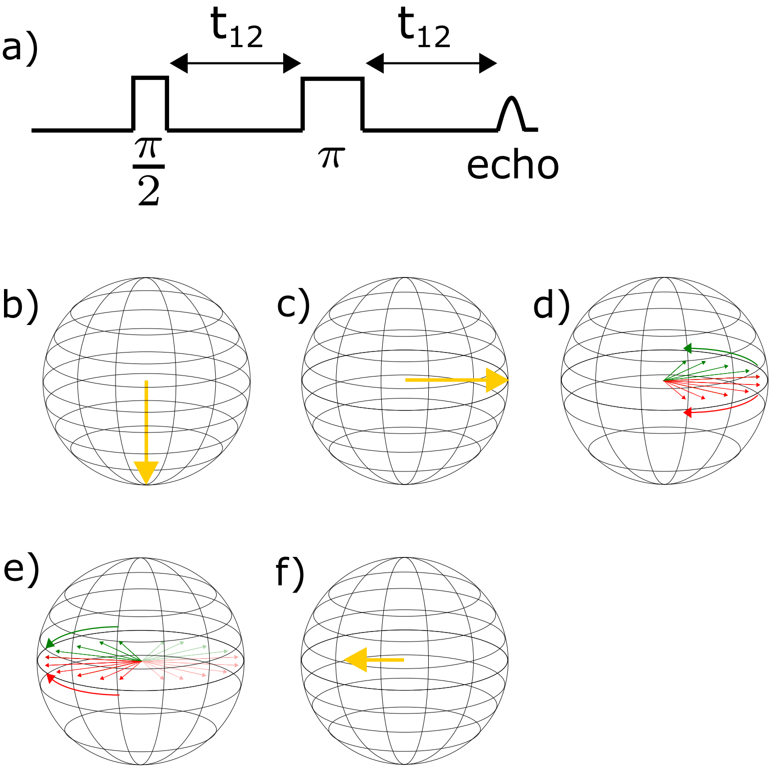

Figure 2.5: a) Two-pulse photon echo pulse sequence. The Bloch sphere representation of the two-pulse photon echo is depicted from b) to f). In b), atoms are in the ground state. In c), the first $\frac{\pi}{2}$ pulse moves atoms to a superposition of the ground and excited state. In d), atoms start dephasing. In e), the π pulse is applied to reverse the phase evolution of the atoms by 180 degrees in order to rephase atoms. In f), complete rephasing results in a coherent emission, a photon echo.

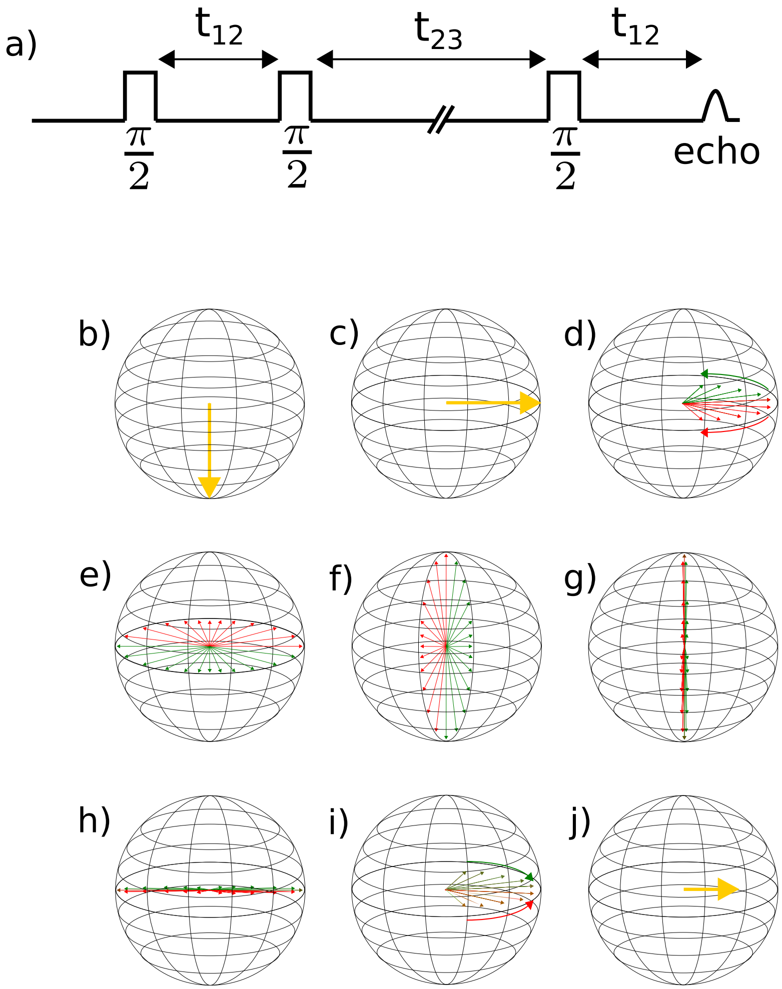

Figure 2.6: a) Three-pulse photon echo pulse sequence. The Bloch sphere representation of the three-pulse photon echo is depicted from b) to j). In b), atoms are in the ground state. In c), the first $\frac{\pi}{2}$ pulse moves atoms to a superposition of ground and excited state. In d), atoms start dephasing. In e), atoms are dephased. In f), the second $\frac{\pi}{2}$ pulse is applied to move the atoms to the ground and excited state depending on their frequency detunings and hence phase. In g), a population grating is created in the ground and excited states. In h), the third $\frac{\pi}{2}$ pulse is applied to stimulate the re-emission. In i), atoms are rephasing. In j), the complete rephasing leads to the emission of a photon echo.

value is the hole lifetime. Such an extracted lifetime can be the excited level lifetime or the lifetime of any other long-lived spin level. The former is referred to as transient spectral hole burning and the latter, persistent spectral hole burning.

Transient spectral hole burning
If the lifetime of the burnt hole is determined by the lifetime of the excited level, T_1, then the spectral hole burning is known as transient spectral hole burning [13].

Persistent spectral hole burning
If there is a chance that pumped atoms decay to another ground level, they are no longer resonance with the burning laser, and a persistent spectral hole [14] is created that lasts during the long-lived ground-state level used for optical pumping. In this case, the hole lifetime corresponds to the lifetime of a long-lived ground-state spin level. In REI-doped materials, either at zero or non-zero applied magnetic field, there usually exist such sub-levels, e.g. electronic or nuclear Zeeman or hyperfine sub-levels. The lifetime of these sub-levels, T_1^s, varies from milliseconds to days, depending on the REI as well as the host. These levels can be employed as population reservoir (referred to as shelving levels) or long-term storage sub-levels for optical quantum memories, which will be described later.

A set of conditions that allows one to extract the aforementioned information, e.g. side-hole and anti-hole structures, from persistent spectral hole burning are listed below:

- Inhomogeneous broadening of the absorption profile is much broader than the homogeneous linewidth ($\Gamma_{in} \gg \Gamma_h$).
- The splitting between the ground-state sub-levels is much larger than the homogeneous linewidth ($\delta \gg \Gamma_h$).
- Inhomogeneous broadening of the absorption profile is much broader than the splitting between the ground-state sub-levels ($\Gamma_{in} \gg \delta$).
- The lifetime of the ground sub-levels is much greater than the time required to populate these levels (($T_1^a \gg T_1/\beta$) (β is the branching ratio.).

To gain more insight into persistent spectral hole burning, let us consider a simple level structure with two sub-levels in the excited level and two in the ground level. In this example, we assume an ensemble of atoms without inhomogeneous broadening. As shown in Fig. 2.7a, the burning laser is resonant with the $\left|g_1\right\rangle \rightarrow |e_1\rangle$ transition, and the target atoms are pumped into $\left|g_2\right\rangle$ via $|e_1\rangle$. Lack of absorption of the $\left|g_1\right\rangle \rightarrow |e_1\rangle$ transition results in the creation of a depleted region in the absorption line, observed as a spectral hole (the central hole). Another depleted region (transparency) can be also seen as a side-hole in $\left|g_1\right\rangle \rightarrow |e_2\rangle$, which is detuned by Δe from the central hole. Also, the overpopulation in the ground-state sub-level $\left|g_2\right\rangle$ leads to the observation of two regions of increased absorption (anti-holes), detuned by Δg and Δg - Δe with respect to the central hole, respectively. See the lower panel of 2.7a for the hole configuration. It

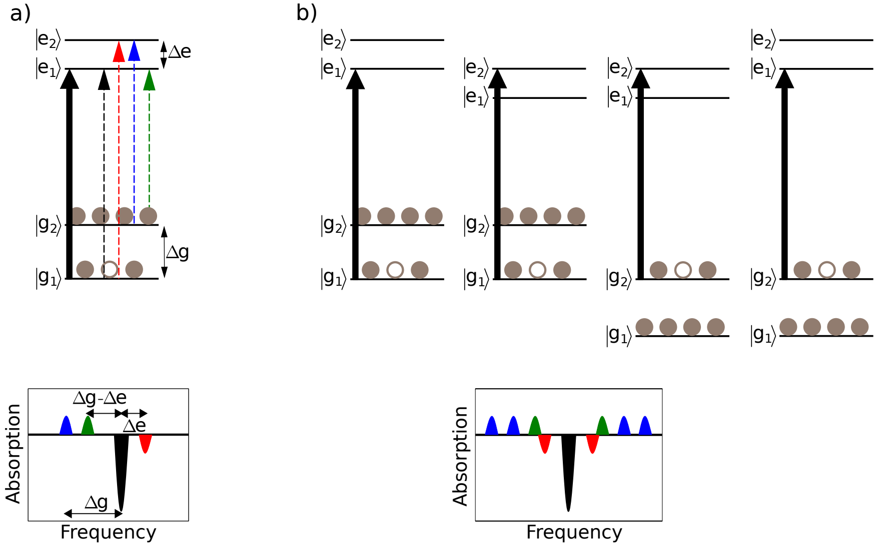

Figure 2.7: Persistent spectral hole burning performed in a four-level system. The solid arrow indicates the burning laser and the four dashed arrows represent the scanning transitions. a) An ensemble without inhomogeneous broadening. Two anti-holes are created due to the overpopulated transitions and a side-hole is created due to the depleted transition. b) An ensemble with inhomogeneous broadening. The burning laser is resonant with other transitions at the same time, which generates a mirrored hole pattern with respect to the central hole. Such hole and anti-hole pattern occurs only when the inhomogeneous broadening is much larger than the energy splitting between spin sub-levels ($\Gamma_{in} \gg \Delta_g \& \Delta_e$). Note that each of the four-level systems creates one central hole, one side-hole and two anti-holes similar to a), and convolution of all these is indicated in the lower panel of b). Figure is reproduced from [15].

can be seen that in addition to lifetime measurements, persistent spectral hole burning allows one to extract the energy splitting both the ground and excited levels. In an inhomogeneously-broadened media, the burning laser frequency is simultaneously resonant with many more transitions, which results in a symmetric hole pattern as shown in Fig. 2.7b.

Hole width limitations

The width of the burnt hole is ideally two times the homogeneous linewidth, assuming a Lorentzian shape of the linewidth, $\Gamma_{laser} < \Gamma_h$, and no power broadening [10]. However, there are many practical issues that make spectral holes broader.

One broadening effect is power broadening. When the laser intensity increases, the excitation rate of the ions increases. If the excitation rate is equivalent to the decay rate, so-called power broadening starts contributing. Increasing further the laser intensity leads to exciting ions that are slightly off-resonance with respect to the burning laser and thereby hole broadening.

Similar to the broadening effects of the homogeneous linewidth discussed above, spectral diffusion is an important source of large holes. Dynamical processes, causing spectral diffusion, usually occur over various timescales; it can be assessed by two- and three-pulse photon echo measurements.

2.2. LONG-DISTANCE QUANTUM COMMUNICATION

Photons at telecom wavelength are very well-suited to act as quantum information carriers for long distances due to their low loss in optical fibres, low coupling to the environment, and the fact that quantum information can be encoded into any of their degrees of freedom (e.g., polarization, frequency, orbital angular momentum, temporal modes). The encoding is carried out by preparing the photon's quantum state (once the degree of freedom is chosen) as a coherent superposition. In its simplest form, this superposition is over a two-dimensional complex Hilbert space and, therefore, involves two orthogonal states such as horizontal and vertical polarizations, or early and late temporal modes, which constitutes a *qubit* [16]; a quantum bit in analogy with a two level classical bit. For the experimental realizations conducted in this thesis, so-called time-bin qubits have been employed, which, in their general form, are written as:

$$|\Psi\rangle = \frac{1}{\sqrt{2}}(|e\rangle + e^{i\Phi}|l\rangle), \qquad 0 \le \Phi \le 2\pi, \tag{2.6}$$

where e and l stand for early and late temporal modes, respectively.

Generation, storage, transmission, and measurement of quantum information encoded into photons underpin the realization of quantum communication. In the following, we will discuss entanglement sources, quantum memories, entanglement swapping, and measurement apparatuses in view of these roles.

2.2.1. ENTANGLEMENT

A system is said to be entangled [17] if the state of the system cannot be described as the product of its individual constituent states. In particular, for a bipartite system, it can be written as:

$$\left|\Psi_{a,b}\right\rangle \neq |\Psi_a\rangle \otimes |\Psi_b\rangle\,. \tag{2.7}$$

Entangled particles manifest quantum correlation regardless of their separation.

ENTANGLEMENT CHARACTERIZATION

Presence of entanglement is certified by entanglement witnesses whereas the amount of entanglement is quantified by entanglement measures such as Von Neumann entropy and entanglement of formation.

Quantum state tomography

There are several tools to experimentally detect entanglement, each of which offers different entanglement evaluations. One of the most commonly-employed experimental technique is quantum state tomography (QST) [18, 19]. By preparing many identical copies of a given quantum state, projecting these onto different measurement bases, and acquiring statistically relevant results, QST enables one to infer the density matrix that describes said quantum state. From the reconstructed density matrix, it is possible to certify the presence of entanglement both qualitatively (using the fidelity of the prepared state with respect to the theoretically expected entangled state) and quantitatively (using the concurrence or the entanglement of formation of the prepared state).

CHSH Bell-inequality and non-locality

John Bell proved, in 1964 [20], that quantum mechanics cannot be described by local hidden variables; one of the most celebrated outcomes of his work was the so-called Bell-inequality, which stipulates a boundary between local and non-local theories. Evaluating this boundary experimentally is referred to as a Bell test, whose central point is to measure the quantity of correlation between measurements of the individual constituents of a bipartite system. Translation of the Bell-inequality into an experimentally feasible Bell test was introduced in 1969 by Clauser, Horne, Shimony and Holt [21], the so-called CHSH Bell-inequality test.

Violation of a CHSH Bell-inequality indicates the non-local nature of the measurement results and involves the evaluation of the S parameter,

$$S = |E_{x_1 x_2} + E_{x_1 y_2} + E_{y_1 x_2} - E_{y_1 y_2}|, \tag{2.8}$$

where $\mathrm{E}_{x,y}$ represents correlation coefficients between two space-like separated measurements, for which the outcomes can be +1 or -1, as shown in Fig. 2.8.

The maximum S parameter for any local theory is 2 ($S_{LHVT} \leq 2$, where $LHVT$ stands for local hidden variable theory), while quantum mechanics predicts a maximum of $2\sqrt{2}$. Violating CHSH Bell-inequality requires entangled states.

BELL-STATE MEASUREMENT

The goal of a quantum repeater is to allow distant parties to share entanglement and therefore to overcome the channel loss. Intrinsic to quantum repeaters is the concatenation of elementary links using an operation known as entanglement swapping. This operation requires two previously uncorrelated quantum states (in this case, qubits) to be projected onto one of the four maximally entangled bipartite states, also known as

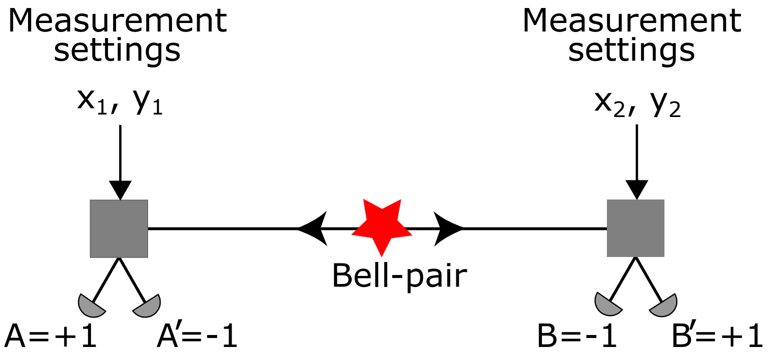

Figure 2.8: CHSH-Bell inequality violation. As an example, protective measurements, x_1, y_1, x_2 and y_2 can be observables $\hat{\sigma}_x$, $\hat{\sigma}_z$, $\frac{\hat{\sigma}_x+\hat{\sigma}_z}{\sqrt{2}}$ and $\frac{\hat{\sigma}_x-\hat{\sigma}_z}{\sqrt{2}}$, respectively, where $\hat{\sigma}_{x,z}$ are the Pauli X and Z operators.

Bell states. This projective measurement, the Bell-state measurement (BSM), can be conducted using linear optical devices (namely, an optical beam splitter), but with a maximum efficiency (excluding the detection efficiency) of 50% [22]. The core of the BSM is the two-photon interference effect, which ensures the erasure of the which-path information of the incoming photons. In the case of time-bin qubits, the four Bell states are as follows:

$$\begin{aligned} \left|\Phi^{\pm}\right\rangle &= \frac{1}{\sqrt{2}}(|ee\rangle \pm |ll\rangle) \\ \left|\Psi^{\pm}\right\rangle &= \frac{1}{\sqrt{2}}(|el\rangle \pm |le\rangle\,. \end{aligned} \tag{2.9}$$

To gain more insight into how a BSM can discriminate all four Bell-states, it is useful to consider different sets of possible outputs. In this scenario, the two photons are sent into the beam splitter's input ports, and the detectors are placed after its two output ports, as shown in Fig. 2.9. First, when two photons are detected in different output ports and at different times, this implies that the BSM has projected the input state onto either $|el\rangle$ or $|le\rangle$; it can be shown that, using the quantum mechanical description of the beam splitter transformation, this result indicates a projection onto the $|\Psi^{-}\rangle$ Bell state. Second, when two photons are detected in the same output ports at different times, once again it implies projection onto $|el\rangle$ or $|le\rangle$; however, this time the result indicates that a projection onto the $\left|\Psi^{+}\right\rangle$ Bell state has occurred. Third, when two photons are detected in the same output at the same time, this leads to a projection onto product state; either $|ee\rangle$ or $|ll\rangle$.

Results deduced from all the scenarios reveal that the maximum efficiency that can be achieved with a linear optics BSM is 50% [23]. Nevertheless, thanks to ancillary photons [24], the efficiency of the BSM can exceed 50%. It is also noteworthy to mention that an alternative to the above-discussed linear optics BSM is to utilize a two-qubit gate, which, in principle, can reach unit efficiency [25].

ENTANGLEMENT SWAPPING

The first step towards long-distance entanglement distribution is to realize teleportation of an entangled state, also referred to as entanglement swapping [26]. A simpler case would be teleportation of a qubit, see Fig. 2.9a, where an input quantum state is transferred from one party to another party using entanglement local operations and classical communication (LOCC) [22]. In entanglement swapping, the input quantum state (b) is entangled with another state (a); after measurement, classical communication, and unitary transformations, (d) which is now (b), is entangled with (a) – refer to Fig. 2.9b.

To understand the mathematics behind entanglement swapping, let us assume the initial state:

$$|\Psi_{abcd}\rangle = \left|\Phi^{+}_{ab}\right\rangle \otimes \left|\Phi^{+}_{cd}\right\rangle = \frac{1}{2}\left(|e_a e_b\rangle + |l_a l_b\rangle\right) \otimes \left(|e_c e_d\rangle + |l_c l_d\rangle\right). \tag{2.10}$$

Assuming the BSM is successful, which, as we have discussed previously, translates into a projection onto $\left|\Psi^{\pm}\right\rangle$, swapping can take place. Without loss of generality, let us say that the projection is onto $|\Psi^{-}\rangle$, which results in the following state:

$$|\Psi_{ad}\rangle = \left\langle \Psi^{-}_{bc} \middle| \Psi_{abcd} \right\rangle = \frac{1}{\sqrt{2}}\left(|e_a l_d\rangle - |l_a e_d\rangle\right) = \left|\Psi^{-}_{ad}\right\rangle. \tag{2.11}$$

It is important to note that the structure of the final entangled state is different from that of the initial individual entangled states: the final state is of the form of $|\Psi^{-}\rangle$ and the initial states were of the form of $\left|\Phi^{+}\right\rangle$. Fortunately, it can be shown that any Bell-state can be mapped onto another through unitary transformations; which unitary transformation is necessary will be determined by the BSM result. This is where the role of classical communication comes into play, since this result must be transmitted to the outermost parties, so that a correct mapping can be performed, and the parties share entanglement.

2.2.2. QUANTUM REPEATERS BASED ON ABSORPTIVE QUANTUM MEMORIES AND ENTANGLED PHOTON-PAIR SOURCES

To realize long-distance quantum communication, the total distance (end-node to end-node) has to be broken down into shorter links, so-called elementary links. This brings up the need for a new technology in quantum communications: quantum repeaters. Quantum repeaters allow interconnections between consecutive elementary links via a local measurement station, i.e., concatenated entanglement swapping links. One of the well-known architectures for quantum repeaters is based on entangled photon-pair sources and absorptive quantum memories [27].

A conceptual schematic of such a quantum repeater architecture is depicted in Fig. 2.10, which includes two elementary links connected via a local BSM. The way the quantum repeater works is as follows. After generation of entangled photon pairs in each elementary link (two per link), one member of each pair is sent through a long-length optical fibre towards the remote Bell-state measurement (BSM) station, while the other member is stored into an absorptive quantum memory. Conditioned on a successful BSM, entanglement is heralded between the two quantum memories, after LOCC, within

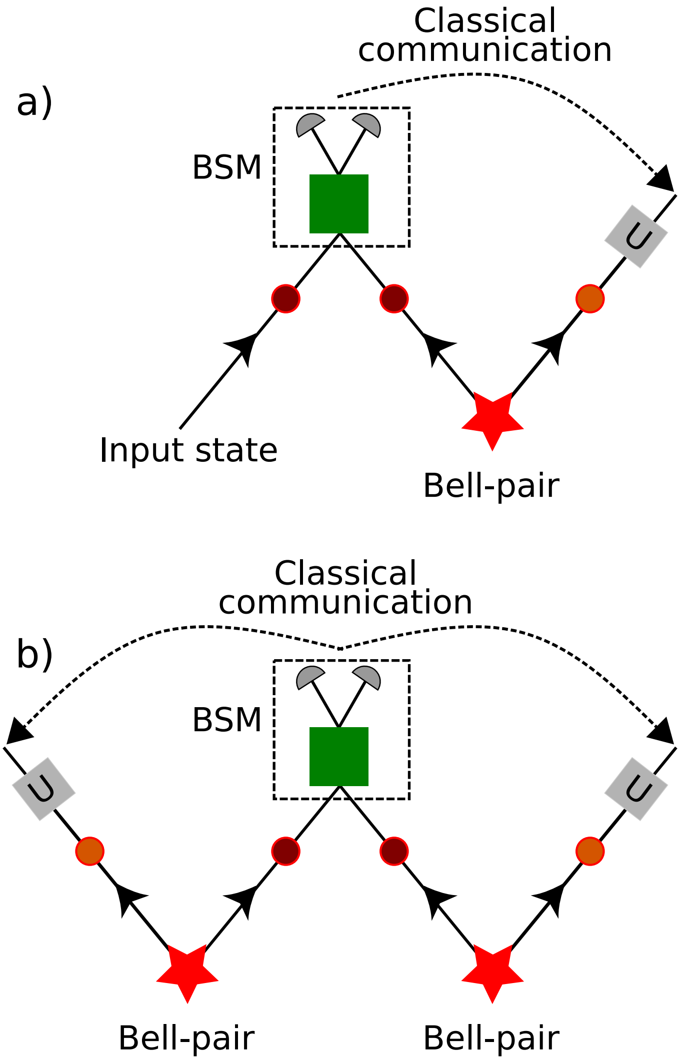

Figure 2.9: a) Qubit teleportation. b) Teleportation of entanglement (entanglement swapping).

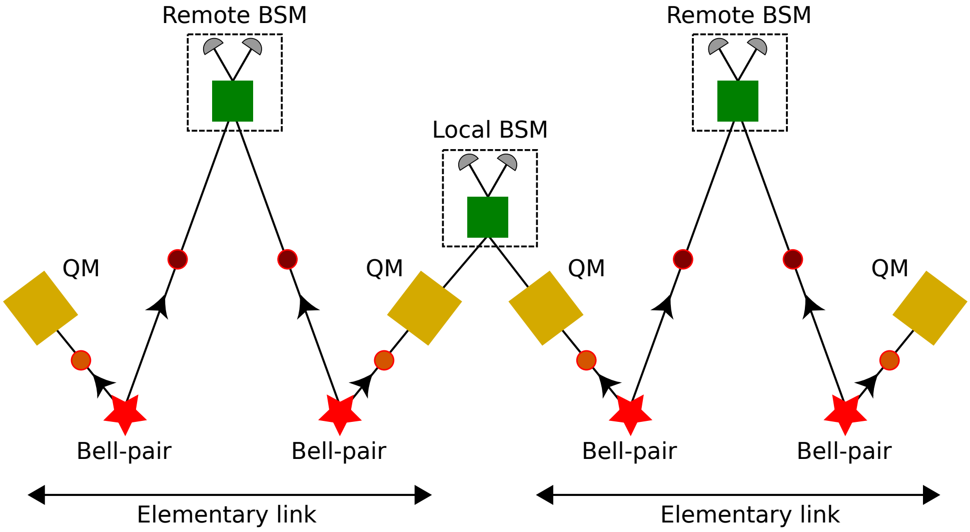

Figure 2.10: A quantum repeater based on absorptive quantum memories (QM) and entangled photon-pair sources (Bell-pairs).

each elementary link. Finally, a local BSM—located between the two elementary links—allows entanglement swapping to take place once again, and the states stored in the outermost quantum memories become entangled after LOCC. The addition of extra elementary links follows the same logic, but with increasing complexity due to the increasing number of entanglement generation, storage, and swapping steps.

As it will be discussed in more depth in the following sections, a very important feature of rare-earth ion-doped (REI-doped) materials, which is the focus of research in our group, is their broad spectrum; this, in turn, allows for *spectral multiplexing*, where the quantum states of multiple photons, occupying different spectral regions, can be stored in the quantum memory simultaneously. This salient feature is highly beneficial when one wishes to increase the rate of entanglement distribution across the repeater network [28]. Our group has been working towards a spectrally-multiplexed quantum repeater in which spectrally-multiplexed absorptive quantum memories [29] and spectrally-multiplexed entangled photon-pair sources based on spontaneous parametric down conversion (SPDC) [30] are the two building blocks.

Considering that the number of multiplexed spectral modes is high enough (preliminary studies show that $> 10^3$ modes would be a good starting point for ~ 100 km elementary links [27]), the entanglement generation rate per elementary link approaches unity at each trial; the rate of trials is determined by the repetition rate of the source. In this case, a spectrally-multiplexed quantum repeater would not require on-demand absorptive quantum memories, a necessary resource for temporally-multiplexed quantum repeater protocols. In fact, the only requirement for storage times in such a spectrally-multiplexed quantum repeater architecture would be for it to overcome the round-trip time between a quantum memory and the remote BSM within the elementary link.

2.3. ENSEMBLE-BASED OPTICAL QUANTUM MEMORIES

2.3.1. FIGURES OF MERIT

In order for a quantum memory to be applicable for a quantum repeater, its different characteristics have to meet specific requirements. These characteristics include, for example, storage time, efficiency, fidelity, multimode capacity, bandwidth, and wavelength, which are individually discussed below.

Storage time

In quantum repeaters, the entangled states must be stored in the quantum memories, placed at either end of the elementary link, until entanglement is established in the neighboring links and, ultimately, entanglement can be swapped all the way to the outermost parties. Storage time, as the name implies, is the time between the absorption and re-emission of the photons carrying the quantum state. The lower bound on the necessary storage time is determined in a spectrally-multiplexed quantum repeater by the total time necessary for the entanglement swapping procedure to take place within an elementary link; the entanglement swapping duration within an elementary link is calculated by the round trip time, i.e., the time necessary for a photon to reach the remote BSM station of an elementary link and for the heralding signal (classical communication) to reach the local node. As an example, for a 100km elementary link, the storage time is lower bounded by $T_s \geq 500\mu$s. This is in contrast with a general quantum repeater, where the storage times must meet the time necessary for entanglement to be established between the outermost parties, a much more stringent lower bound.

Efficiency

A quantum memory's efficiency is defined as the probability of a single-photon to be absorbed and re-emitted in the desire temporal mode, i.e., that corresponds to the predefined storage time.

In practice, it is always a challenge to reach unit efficiency. For the case of quantum repeaters, a highly efficient quantum memory translates into a higher entanglement establishment rate. It is discussed in [27] which quantum memories with 90% efficiency are sufficient to build a practical quantum repeater that would outperform the direct transmission through optical fibers. Also in [27], it is stated that "A reduction in the memory efficiency from 90% to 89% leads to an increase in the entanglement distribution time by 10-14%, depending on the repeater protocol"; in other words, the dependence of the entanglement distribution time on the quantum memory efficiency is quite significant.

Fidelity

For a device to be identified as a "quantum" memory, the fidelity must exceed the limit of a "classical" memory, which corresponds to fidelity of 2/3 [31]. Fidelity, by definition, indicates the closeness of two quantum states (ρ and $\rho_{\prime}$) and it is given by

$$F = tr\left(\rho\rho_{\prime}\right). \tag{2.12}$$

Even though the efficiencies of most quantum memories demonstrated to this day are still far from unity, the demonstrated values of fidelity are already above 90% and for REIs are above 99%.

Multimode capacity

Due to the presence of a multitude of absorbers, One of the merits of ensemble-based quantum memories is their capacity of storing many input photonic states simultaneously, a feature known as multiplexing capability. Even though spectral-multiplexing has been given more focus in this document, the multiplexing can also be achieved temporally (with a train of input photonic states), spatially, or with respect to polarization. The interplay between multimode capacity and increased entanglement distribution rate is intimate.

Bandwidth

The Bandwidth of a quantum memory is defined as the spectral window within which photons can be absorbed. For a spectrally-multiplexed quantum repeater, the higher the bandwidth, the higher the rate of entanglement distribution since more photonic modes could be absorbed simultaneously. Since the storage of an input state is intimately connected to the overlap between the memory's and photonic mode's bandwidths (the latter necessarily falling within the former), a broadband quantum memory also allows for rather short photonic pulses to be stored due to a Fourier relation. The shorter the pulse, the higher the repetition rate, and, thus, the entanglement distribution rate.

Wavelength

Up to now, extensive work has been conducted with various optical quantum memories, with operating wavelengths ranging from visible to telecom-wavelength. Presently, it is not clear which wavelength is the best choice for quantum repeater. Moreover, the operating wavelength of a quantum memory is also tied to the available photon sources and detectors. However, it is obvious that in order for quantum devices to be easily integrated into current classical networks, telecom-wavelength quantum memories are extremely attractive.

2.3.2. PROTOCOLS

ABSORPTIVE QUANTUM MEMORIES

If a quantum memory is able to store and re-emit an input photonic quantum state that has been prepared elsewhere, it is referred to as an *absorptive* quantum memory in contrast with *emissive* quantum memories, which will be defined later on. Absorptive quantum memories are interesting since they can be used in conjunction with an external Bell-pair source, for instance in the quantum repeater architecture presented in Fig. 2.10. They can be divided into two classes: optically-controlled; and engineered absorption memories. The former includes off-resonant Raman and electromagnetically induced transparency (EIT) quantum memories and the latter encompasses controlled-reversible inhomogeneous broadening (CRIB), gradient echo memory (GEM), and atomic frequency comb (AFC) quantum memories. Common to all absorptive quantum memory protocols is the need for a Λ-type energy level structure, which is presented in Fig. 2.11a.

Electromagnetically induced transparency and off-resonant Raman

Electromagnetically induced transparency (EIT) and off-resonant Raman coupling protocols share a few similarities, namely that the control field is applied simultaneously with the signal field and that both fields are off-resonant with respect to the excited state $|e\rangle$. Due to these similarities, the energy level structure for the EIT and off-resonant Raman protocols are presented together in Fig. 2.11a and b, respectively. Nevertheless, in the off-resonant Raman protocol, the detuning Δ between the signal field and the ground-to-excited state transition excited state and the state with which the fields are resonant is much larger, i.e., larger than the atomic inhomogeneous broadening. The difference causes the protocols to work under different conditions.

EIT [32] is created by simultaneous injection of a signal field close-to-resonant with the $|g\rangle \to |e\rangle$ transition and a control field close-to-resonant with the $|s\rangle \to |e\rangle$ transition, as shown in Fig. 2.11a. Consequently, a transparency window in the absorption profile is created within which the group velocity of the signal field is slowed down and, then, stopped for some controllable amount of time [32]. Such a transparency stems from a destructive quantum interference between two excitation paths ($|g\rangle \to |e\rangle$ and $|g\rangle \to |e\rangle \to |s\rangle \to |e\rangle$) experienced by the signal field. Storage of the quantum state encoded into the signal field is performed in spin coherence (so-called dark state) by adiabatically switching off the control field. Finally, re-emission is achieved by switching the control field back on. Energy level structure, storage and retrieval time sequence, and susceptibility configuration are shown in Fig. 2.11a, c, and d. In the EIT quantum memory protocol:

- Efficiency depends on the optical depth of the medium.
- Storage time is limited by the long-lived level (spin) coherence time.
- Bandwidth is determined by the transparency window linewidth, which is controlled by the Rabi frequency of the control field.
- Multimode capacity scales with the square root of optical depth.

The off-resonant Raman protocol [33] requires the application of a far off-resonant coupling field, which results in storage and retrieval of an input quantum state encoded in the signal field. Assuming that all atoms are initially in the ground state $|g\rangle$, the signal field is near-resonant with the $|g\rangle \to |e\rangle$ transition, and the strong control field is near the resonant with the $|s\rangle \to |e\rangle$ transition, as shown in Fig. 2.11b. In this protocol, both signal and coupling fields share the same virtual state, meaning $\omega_p - \omega_c = \omega_{gs}$. Therefore, the absorption of the signal field is performed via stimulated off-resonant Raman scattering. The simultaneous injection of signal and control fields does not create a transparency window, as it does in EIT, because of its far off-resonant nature. Nevertheless, similar to EIT, it creates a spin coherence. Adiabatically switching the control field off and on, after absorption, allows on-demand retrieval of the quantum state. Energy level structure, and storage and retrieval time sequence are shown in Fig. 2.11b and c. In the Raman quantum memory protocol:

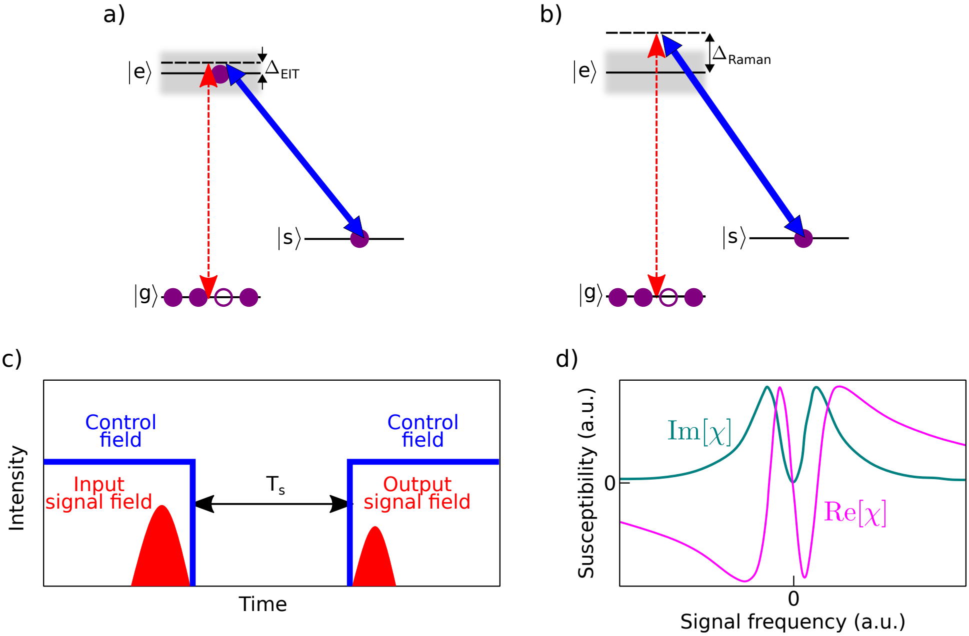

Figure 2.11: a) Energy level structure for the EIT protocol. b) Energy level structure for the off-resonant Raman protocol. c) Storage and retrieval time sequence in EIT and off-resonant Raman protocols. T_s represents the storage time, which is limited by the spin coherence time. d) Susceptibility experienced by the signal field as a function of its frequency detuning in the EIT protocol. Imaginary part and real part of the susceptibility usher absorption and dispersion, respectively. The transparency window, created around zero detuning, can be observed in the absorption spectrum.

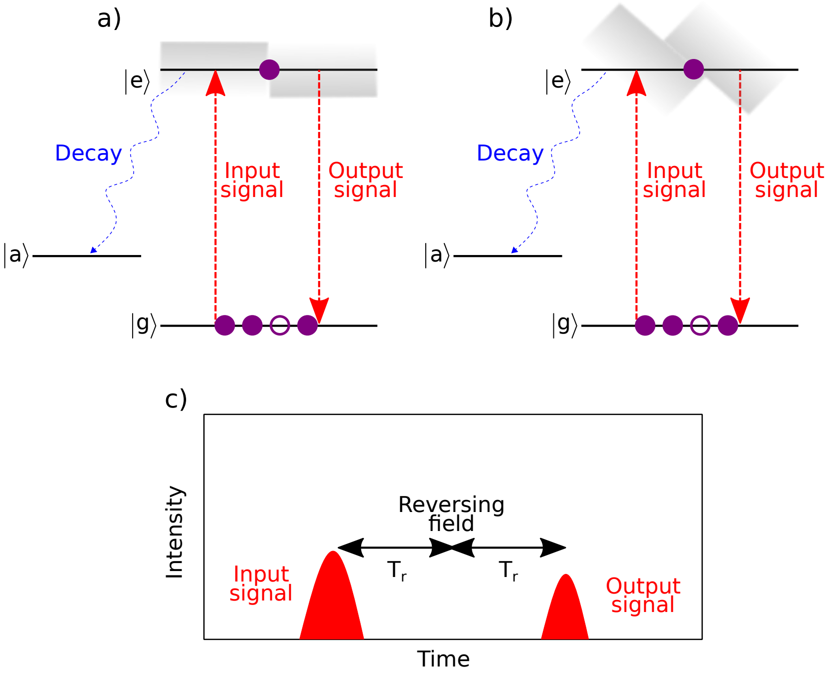

Figure 2.12: a) Energy level structure used for the CRIB protocol. b) Energy level structure used for the GEM protocol. c) Storage and retrieval time sequence in both protocols. T_s represents storage time limited by spin coherence.

- Efficiency depends on optical depth, signal field coupling, Rabi frequency of control field, detuning Δ_{raman}, and spin inhomogeneous broadening.
- Storage time is limited by the long-lived level (spin) coherence time.
- Bandwidth is determined by the bandwidth of the control field.
- Multimode capacity scales with the square root of optical depth.

Controlled-reversible inhomogeneous broadening and gradient echo memory

The controlled reversible inhomogeneous broadening quantum memory protocol [34, 35], known as CRIB, was the first protocol in which atomic inhomogeneous broadening was utilized and sought after instead of avoided. CRIB can be implemented in two different ways. When the external field varies transversely through the medium (the gradient is perpendicular to the input signal propagation), it is known as a transverse CRIB, and when the external field varies longitudinally through the medium (the gradient is parallel to the input signal propagation), it referred to as longitudinal CRIB or gradient echo memory (GEM) [36]. Again, due to their similarities, the energy level structure necessary for both is presented together in Fig. 2.12a and b.

CRIB requires an atomic ensemble with narrow spectral linewidth; in an ensemble exhibiting inhomogeneous broadening, this is achieved by optically pumping atoms with a transition outside this width into a long-lived shelving level ($|a\rangle$) through the excited state ($|e\rangle$). Then, an external electric, magnetic, or optical field is used to controllably broaden the narrow spectral line in a controlled manner into an inhomogeneously broadened line. The absorption of a photon creates an collective atomic excitation, whose mathematical description is that of a Dicke state [37]:

$$|\Psi(t)\rangle = \sum_{j=1}^{N} C_j e^{-i2\pi\delta_j t} e^{ikz_j} \left|g_1, g_2, ..., e_j, ..., g_N\right\rangle, \tag{2.13}$$

where N is the number of atoms, C_j is the excitation probability amplitude for each atom, δ_j is the frequency detuning of atom j with respect to the central frequency of the input signal, z_j is the position of atom j, and k is the wave number of the input signal. As stated in Eq. 2.13, each atom acquires a different phase ($\delta_j t$) depending on its frequency detunings imposed by the inhomogeneous broadening; consequently, the atoms start to dephase over time. However, owing to the controlled inhomogeneous broadening, by reversing the external field at $\mathrm{t} = \mathrm{T}_r$, atom j now experiences a reversed phase evolution of $-\delta_j(t - \mathrm{T}_r)$. Therefore, as can be seen from Eq. 2.13, at $\mathrm{t} = 2\mathrm{T}_r$ (defined as the storage time) the state rephases, leading to a coherent re-emission of a photon.

In transverse CRIB, the retrieval efficiency is limited to 54% in forward re-emission due to re-absorption of the re-emitted signal [34, 35]. Such a re-absorption process can occur since the same inhomogeneously-broadened absorption spectrum is created in each slice of the medium and the re-emitted signal traverses each slice. One technique to tackle this limitation is to trigger backwards re-emission [35, 38]. In this case, a spatial phase-matching condition is required and, in principle, re-emission can approach unit efficiency. At the same time, in GEM (or longitudinal CRIB), the retrieval efficiency can reach unity even for forward re-emission

since inhomogeneous broadening is different for each slice of the absorption medium. The storage and retrieval time sequence of both the CRIB and GEM protocols are shown in Fig. 2.12c. In the CRIB/GEM protocols:

- Efficiency depends on the optical depth of the medium.
- Storage time is limited by the atomic coherence time.
- Bandwidth is determined by the spectral linewidth of the absorption line after broadening.
- Multimode capacity scales linearly with optical depth.

It is important to note that the main limitation of the CRIB/GEM protocols is the high optical depth required for high efficiency. This is due to the fact that the optical depth of the initial absorption line is distributed over a broader spectral region, resulting in a reduced effective optical depth.

Atomic frequency comb

Quantum memories based on the atomic frequency comb (AFC) protocol [38] are the focus of this thesis and, consequently, this is the protocol described in more depth. It is interesting to note that it resembles the conventional three-pulse photon echo (3PPE) spectroscopic technique discussed in Section I of this chapter; the modification from 3PPE to AFC is the exclusion of the spontaneous emission from the excited state [39]. As the name implies, an AFC is a periodic comb structure in the spectral domain or, in other words, an evenly spaced spectral array of absorption peaks. The interaction of an incoming photon with such a structure leads to absorption followed by re-emission after a pre-defined storage time, as will be described below.

Similar to the CRIB/GEM protocol, an inhomogeneously-broadened absorption profile is necessary. It can be prepared through persistent spectral hole burning. Initially, all atoms are assumed to be in the ground state, which can be enforced by cooling down the ensemble. The atoms are then selectively pumped into a long-lived shelving level $|s\rangle$ through the excited state $|e\rangle$, where the selection is performed in the frequency domain. A detailed description of this specific technique is stated in the upcoming subsection. Before absorption of an input photon, the joint quantum state of the joint photon-atom system is as follows:

$$|1\rangle_{ph} \otimes \left|g_1, g_2, ..., g_j, ..., g_N\right\rangle_{at}. \tag{2.14}$$

If the single photon is absorbed, as depicted in Fig. 2.13, a collective atomic excitation is created. The resulting quantum state is, again, described by a Dicke state:

$$|0\rangle_{ph} \otimes \Big(|\Psi(t)\rangle = \frac{1}{\sqrt{N}} \sum_{j=1}^{N} C_j e^{-i2\pi\delta_j t} e^{ikz_j} \left|g_1, g_2, ..., e_j, ..., g_N\right\rangle \Big)_{at}. \tag{2.15}$$

Similar to the CRIB/GEM protocol, and due to the different frequency detuning of atoms with respect to the central frequency of the single photon, atoms accumulate different phases; for instance, atom j acquires $\delta_j t$. However, because of the periodic nature of the AFC structure, δ_j can be replaced by $m\Delta$, where Δ is the peak spacing of the AFC and m is an integer. It can be seen from Eq. 2.15 that, at time t = $1/\Delta$, the exponential term, which includes the accumulated phases, equals 1. This collective rephasing yields a coherent emission, expressed by Eq. 2.16 (also refer to Fig. 2.14c and d).

$$\begin{aligned} |0\rangle_{ph} \otimes \Big(|\Psi(t)\rangle = \frac{1}{\sqrt{N}} \sum_{j=1}^{N} C_j e^{-i2\pi m\Delta t} e^{ikz_j} \left|g_1, g_2, ..., e_j, ..., g_N\right\rangle \Big)_{at} \\ \xrightarrow{t=\frac{1}{\Delta}} |1\rangle_{ph} \otimes \left|g_1, g_2, ..., g_j, ..., g_N\right\rangle_{at}. \end{aligned} \tag{2.16}$$

The retrieval efficiency is dependent on several parameters, such as peak linewidth γ; peak spacing Δ; number of atoms participating in the AFC structure d_1 (optical depth); and remaining atoms not participating in the AFC structure d_0 (background optical depth). The ratio between the peak spacing and the peak linewidth is generally referred to as the finesse (F) of the AFC. The retrieval efficiency in the forward re-emission, for a Lorentzian line shape of the individual teeth, is given by

$$\eta = (\frac{d_1}{F})^2 e^{-\frac{d_1}{F}} e^{\frac{-7}{F^2}} e^{-d_0}. \tag{2.17}$$

The first term describes the collective re-emission, where higher $\frac{d_1}{F}$ translates into more atoms contributing to the re-emission. The second term reflects the impact of re-absorption

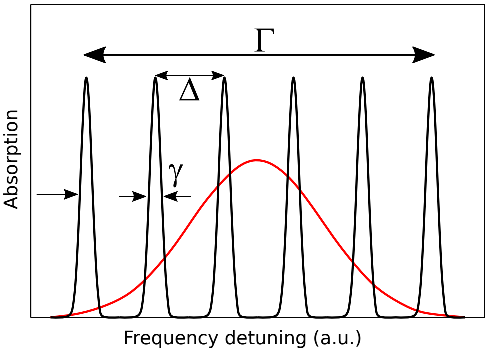

Figure 2.13: Incoming signal field, indicated by the red envelope, is absorbed in an AFC structure with a total bandwidth of Γ. γ corresponds to the linewidth of each peak, and Δ to the peak spacing.

of the re-emitted photon and, in contrast with the first term, higher optical depth and smaller finesse result in a reduction of the retrieval efficiency. The third term represents dephasing. The higher the finesse, the more distinct the spectral peaks are, in turn, the more valid the assumption of $\delta_j = m\Delta$. The last term corresponds to the impact of background optical depth, which leads to excessive loss in the re-emission process. Similar to the CRIB protocol, the maximum retrieval efficiency in the forward re-emission is upper bounded by 54% since there is always a trade-off between absorption and re-absorption.

This upper bound can, however, be overcome, and there are two well-known approaches to boosting the efficiency up to 100%. One solution is to force the photon to be re-emitted in the backward direction (backwards re-emission). This requires mode-matching condition, which can be satisfied by applying two optical π pulses between absorption and re-emission [38]. Additionally, this technique opens the door to on-demand re-emission, henceforth dubbed *full AFC* protocol, and depicted in Fig. 2.14a and b. After absorption, an initial π pulse maps the atomic coherence onto (long-lived) ground-state (spin) coherence. As long as there is no spin inhomogeneous broadening, coherence is maintained for as long as the spin coherence time. The following π pulse, applied after time T_s in the counter-propagating direction, transfers the population back to the excited state, but with a π phase difference in the re-phasing term; the photon is, then, re-emitted in the backward direction. It should be noted that, unlike forward re-emission, in this approach, the higher the optical depth, the higher the retrieval efficiency [38].

The second approach for increasing the retrieval efficiency is to place the medium inside an impedance matched cavity [40]. To achieve 100% absorption, the reflectivity of the cavity's end mirror R_2=1, and that of the front mirror (R_1) is adjusted in such a way that impedance matching is observed, i.e., $R_1 = R_2 e^{-\alpha L}$. Here, α, and L are the absorption coefficient, and the length of the medium, respectively (for a comprehensive description, see [41]).

In the AFC and full AFC protocols:

- Efficiency depends on the optical depth of the medium and the finesse of the comb structure.

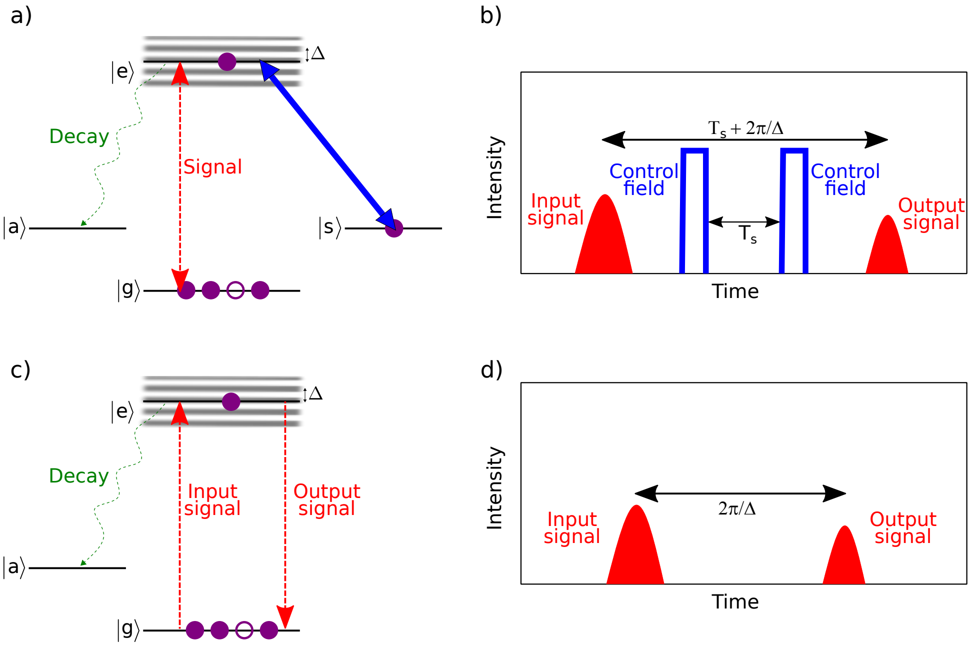

Figure 2.14: a) Energy level structure for the full AFC protocol. b) Time sequence of storage and retrieval in the full AFC protocol. The total storage time is T_s determined by spin coherence and the fixed delay, which is inversely proportional to the peak spacing in the AFC structure (Δ) . c) Energy level structure used for the AFC protocol (also known as two-level AFC protocol). d) Time sequence of storage and retrieval process in the AFC protocol.

- Storage time is limited by the atomic coherence time (AFC protocol) and ground-state level (spin) coherence (full AFC protocol).
- Bandwidth is limited by the splitting of the ground-state spin transition.
- Multimode capacity is independent of the optical depth.

Spectral tailoring

As mentioned previously, the preparation of a material such that it functions as CRIB or AFC quantum memory requires engineering of the inhomogeneously-broadened absorption profile. Spectral tailoring, which allows appropriate spectral features to be created, is associated to frequency-selective optical pumping; atoms exhibiting specific transition frequencies are excited and then decay to a long-lived ground-state level, the so-called shelving level. In the case of the AFC protocol, such frequency-selective optical pumping is carried out in a periodic manner (in the frequency domain), resulting in a frequency comb structure.

Comb-shaping of an inhomogeneously-broadened absorption profile usually depends on the energy splitting of ground state sub-levels. In Tm-doped materials, the energy splitting between such ground state sub-levels is typically on the order of tens to hundreds of MHz per Tesla [29], a rather small splitting that limits the achievable comb fi-

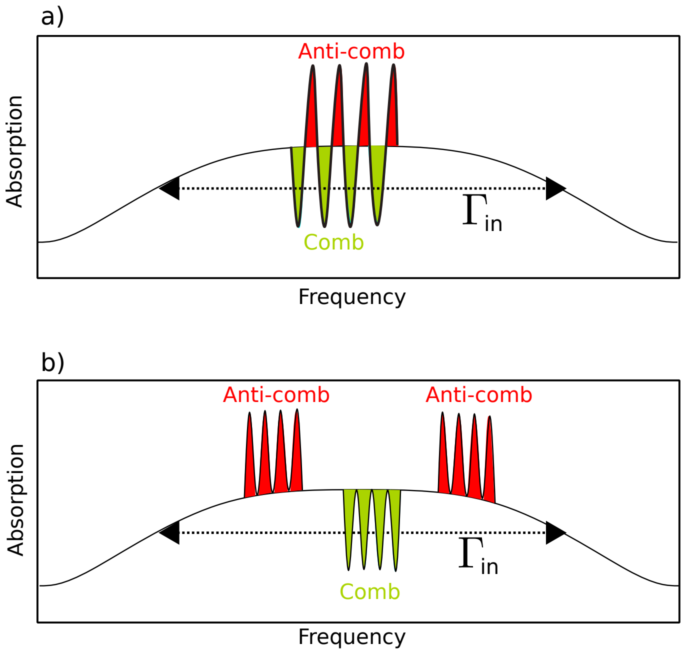

Figure 2.15: Spectral tailoring of an inhomogeneously-broadened absorption profile including one excited level and two ground state sub-levels. a) An AFC structure with finesse 2 is created in an ensemble of thulium atoms. b) An AFC structure with finesse 2 is carved into an ensemble of erbium doped into a host material.

nesse to 2 if the AFC bandwidth is broader than the splitting. This results in a minimum retrieval efficiency in forward direction of around 10% for a Lorentzian line-shape AFC. Due to the proximity between the long-lived shelving level and the initial level (in terms of energy and, thus, the frequency), optical pumping creates anti-holes within the engineered spectral feature. In other words, the population is removed from one trough (hole) and moved to the next crest (anti-hole) in the comb structure, as shown in Fig. 2.15a. Therefore, the final atomic frequency comb is an overlap of the comb and anti-comb structures with twice the optical depth of a single comb.

In Er-doped materials, the energy splitting between ground state sub-levels is quite large, reaching splittings of tens of GHz per Tesla; this is due to their stronger magnetic dipole moment compared to thulium [42]. In this case, the atoms that are pumped into the shelving level also produce anti-holes, but since they are moved outside of the bandwidth of the engineered structure, they will not be a part of the spectral feature of interest. Therefore, a comb structure with finesse $F > 2$ can be carved, as shown in Fig.2.15b.

EMISSIVE QUANTUM MEMORY

Off-resonant Raman scattering (DLCZ)

The DLCZ protocol, named after the authors of [43] where was is proposed, can be interpreted as either a quantum memory protocol or a quantum repeater architecture. Un-

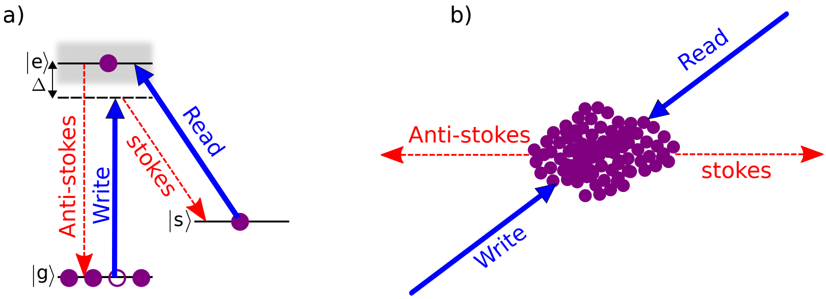

Figure 2.16: a) Energy level structure used for the DLCZ protocol. b) Direction of write/read pulses that are injected into the medium and stokes/anti-stokes photons which are emitted out of the medium.

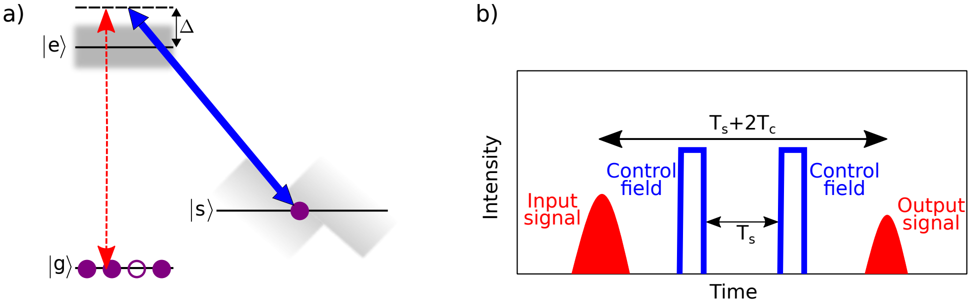

Figure 2.17: a) Energy level structure used for the Raman-GEM protocol. b) Storage and retrieval time sequence in Raman-GEM protocol. T_s and T_c represent storage time limited by spin coherence and the time difference between the incoming signal, and the first π pulse and the second π pulse and the output signal.

like the protocols discussed in the *absorptive quantum memories* section, DLCZ-based quantum memories are not absorptive (external) quantum memories in the sense that entanglement is generated between an optical excitation (a single-photon) and a single spin excitation in the media.

In this protocol, a so-called write pulse interacts off-resonantly (frequency Δ) into the $\left|g\right\rangle \rightarrow |e\rangle$ transition of the Λ-system. A Stokes photon is probabilistically emitted, whose detection heralds the presence of a single spin excitation. Then, after a time smaller than the spin coherence time, another pulse, the so-called read pulse, is sent to transfer the spin excitation into an anti-Stokes photon in a well-defined mode.

NEW PROTOCOLS

Raman-GEM

As previously discussed, the GEM protocol can provide up to 100% retrieval efficiency for a quantum memory. However, the storage time in this protocol is limited by the optical coherence time. In the so-called Raman-GEM protocol [44], this limitation is overcome by transferring atoms from the ground state $\left|g\right\rangle$ to a long-lived spin level $|s\rangle$ through an off-resonant virtual state, i.e., through Raman coupling. In addition, there is no need to perform the initialization step necessary for GEM, i.e., the creation of a narrow absorption line in the optical transition making use of optical pumping and a long-lived shelving level. Since broadening of the linewidth is only necessary for the spin transition, and not the optical transition as in the GEM, a magnetic field gradient is applied longitudinally to broaden the spin transition. This way, an off-resonant coupling field can transfer the incoming signal field into the already broadened spin transition for storage; by reversing the field, complete rephasing is ensured and, by applying the second control field, coherent re-emission takes place, as shown in Fig. 2.17. In Raman-GEM protocol:

- Efficiency depends on the optical depth of the medium.
- Storage time is limited by the spin coherence time (not the optical coherence time, as in usual GEM).
- Bandwidth is determined by the spectral linewidth of the initial line in the spin transition and the strength of the external magnetic field.
- Multimode capacity scales linearly with optical depth.

AFC-based DLCZ

The previously described DLCZ protocol relies on single photon-spin entanglement, which, at least in principle, prevents it to be suitable as a multiplexed quantum memory protocol and, thereby, also to find application in a multiplexed quantum repeater scenario. Therefore, integrating a multiplexed protocol, like AFC, with the conventional DLCZ protocol would overcome such a limitation. In AFC-based DLCZ [45], engineering of a periodic comb structure in the atomic transition is the initial step, as in the AFC protocol. Then, a write pulse interacts with the comb, exciting a small subset of the atoms, which subsequently create a Stokes photon. As a result, a single spin excitation is generated. Now, due to the longevity of the spin transition, the spin coherence can be maintained for as long as the spin coherence time, provided there is no spin inhomogeneous broadening. Again, after a time (ideally) smaller than the spin coherence time, a read pulse transfers back the single spin excitation into the excited state, which leads to the emission of an anti-Stokes photon.

In particular for temporal multiplexing, the main advantage of this protocol is the fact that the optical dephasing term that appears in Eq. 2.15, as described in the AFC protocol, allows encoding of the detection time of the Stokes photon into many temporal modes, resulting in a distinguishable spin wave excitation.

Rephased amplified spontaneous emission

Decoherence caused by spin inhomogeneous broadening in the DLCZ protocol limits the storage time determined by the time interval between the write and read pulses. The rephased amplified spontaneous emission (RASE) protocol [46] addresses this issue by considering only a two-level structure instead of the Λ-system considered so far. In RASE, a π pulse resonant with the atomic transition initially inverts the population between the filled ground state to the empty excited state. A small subset of atoms, ideally one, from the excited state decays down to the ground state through amplified spontaneous emission (ASE). Similar to the spin coherence heralded by the detection of a

Stokes photon, here, an atomic coherence is created that is in phase with the ASE photons. After the detection of the ASE, a second π pulse, the so-called rephasing pulse, is sent into the atomic transition, which allows reading out the atomic excitation through the detection of a rephased amplified spontaneous emission photon (RASE photon), an "echo" of the ASE photon. The RASE photons are temporally symmetric with respect to the moment of the rephasing π pulse and are quantum correlated with the ASE photons.

Revival of silenced echo

In echo-based quantum memory protocols such as AFC and CRIB/GEM, engineering of a section of the inhomogeneously-broadened absorption line of the medium through optical pumping is key, which limits the possibility of using the entire inhomogeneous broadening. In the revival of silenced echo (ROSE) protocol [47], the entire inhomogeneous broadening can be used and there is no need for an initial preparation step. This protocol starts with a two-level atomic structure, within which a weak input signal, resonant with the atomic transition, is absorbed in the medium. Atoms start dephasing due to the atomic inhomogeneous broadening and, similar to the conventional two-pulse photon echo technique, a π pulse is sent to rephase the coherence. This pulse should be sent in such a way that the phase-matching condition is not satisfied and the resultant photon echo is silenced, as the name of the protocol implies. However, a second π pulse is then employed, whose direction is chosen in such a way that a photon echo is enabled.

2.3.3. STATE-OF-THE-ART QUANTUM MEMORIES

Table 2.2 summarizes state-of-the-art absorptive quantum memories (EIT, Raman, CRIB and GEM, AFC, full AFC, and Raman-GEM) in terms of the previously discussed figures of merit, i.e., bandwidth, efficiency, and storage time. Additionally, the retrieving type, the commonly-used media, and the multimode capacity are mentioned. The table is an updated version of the one presented in [48].

Recent demonstrations of AFC-based DLCZ protocol have been implemented in two crystals, $^{151}\mathrm{Eu}^{3+}$:$\mathrm{Y_2SiO_5}$ and Pr^{3+}:$\mathrm{Y_2SiO_5}$, showing a quantum correlation between a single-photon and a single spin excitation up to 12 and 11 temporal modes, respectively [49, 50].

A recent memory demonstration of ROSE has been reported [51]. In this work, the authors showed storage of 7.8 photons per pulse with an efficiency of 30% for a storage time of 16 μs and for a bandwidth of 800 kHz. The signal-to-noise ratio (SNR) is measured to be 0.7, which clearly does not exceed the quantum memory bound.

Regarding emissive quantum memories based on DLCZ protocol, the highest retrieval efficiency and the longest storage time are reported as 76% and 0.2s, respectively, in a single experiment [52]. This experiment is implemented in a cold ^{87}Rb atomic ensemble incorporated in a 3D optical lattice that is confined in a ring cavity.

Protocol	**Retrieval**	**Medium**	**Max. BW (MHz)**	**Max. η (%)**	**Max. T_s (ms)**	**Multimode capacity**
EIT	On-demand	Cold or warm gas, solid state	10^2	85 [53]	10^3 [54]	Low
Raman	On-demand	Cold or warm gas, solid state	10^6	82 [55]	1.5×10^{-3} [56]	Low
CRIB/GEM	On-demand	REI-doped solid state, warm gas	10^2	80 [57]	0.2 [57]	Moderate
AFC	Pre-set	REI-doped solid state	10^3	56 [41]	5×10^{-3} [58]	High
Full AFC	On-demand	REI-doped solid state	10^2	12 [59]	1 [60]	High
Raman-GEM	On-demand	warm gas	10^1	87 [61]	1 [61]	Moderate

Table 2.2: Overview of discussed quantum memory protocols. State-of-the-art for each protocol is stated in terms of bandwidth, efficiency and storage time.

REFERENCES

[1] B. G. Wybourne, *Spectroscopic properties of rare earths,* (1965).

[2] G. Liu and B. Jacquier, *Spectroscopic properties of rare earths in optical materials,* Vol. 83 (Springer Science & Business Media, 2006).

[3] A. J. Freeman and R. Watson, *Theoretical investigation of some magnetic and spectroscopic properties of rare-earth ions,* Physical Review **127**, 2058 (1962).

[4] A. Abragam and B. Bleaney, *Electron paramagnetic resonance of transition ions* (OUP Oxford, 2012).

[5] Y. Sun, C. Thiel, R. Cone, R. Equall, and R. Hutcheson, *Recent progress in developing new rare earth materials for hole burning and coherent transient applications,* Journal of Luminescence **98**, 281 (2002).

[6] C. Thiel, T. Böttger, and R. Cone, *Rare-earth-doped materials for applications in quantum information storage and signal processing,* Journal of Luminescence **131**, 353 (2011).

[7] T. Böttger, C. Thiel, Y. Sun, and R. Cone, *Optical decoherence and spectral diffusion at 1.5 μm in $Er^{3+}:Y_2SiO_5$ versus magnetic field, temperature, and Er^{3+} concentration,* Physical Review B **73**, 075101 (2006).

[8] M. Rančić, M. P. Hedges, R. L. Ahlefeldt, and M. J. Sellars, *Coherence time of over a second in a telecom-compatible quantum memory storage material,* Nature Physics **14**, 50 (2018).

[9] R. Orbach, *Spin-lattice relaxation in rare-earth salts,* Proceedings of the Royal Society of London. Series A. Mathematical and Physical Sciences **264**, 458 (1961).

[10] G. C. Bjorklund, D. Haarer, J. Hayes, R. Jankowiak, W. Lenth, R. Macfarlane, W. Moerner, K. Rebane, L. Rebane, R. Shelby, *et al.*, *Persistent spectral hole-burning: science and applications*, Vol. 44 (Springer Science & Business Media, 2012).

[11] I. Abella, N. Kurnit, and S. Hartmann, *Photon echoes,* Physical review **141**, 391 (1966).

[12] W. Mims, *Phase memory in electron spin echoes, lattice relaxation effects in $CaWO_4$:Er, Ce, Mn,* Physical Review **168**, 370 (1968).

[13] R. M. Macfarlane, *High-resolution laser spectroscopy of rare-earth doped insulators: a personal perspective,* Journal of Luminescence **100**, 1 (2002).

[14] A. Szabo, *Observation of hole burning and cross relaxation effects in ruby,* Physical Review B **11**, 4512 (1975).

[15] S. Hastings-Simon, M. Afzelius, J. Minář, M. Staudt, B. Lauritzen, H. de Riedmatten, N. Gisin, A. Amari, A. Walther, S. Kröll, *et al.*, *Spectral hole-burning spectroscopy in $Nd^{3+}:YVO_4$,* Physical Review B **77**, 125111 (2008).

[16] B. Schumacher, *Quantum coding,* Physical Review A **51**, 2738 (1995).

[17] E. Schrödinger, *Discussion of probability relations between separated systems,* in *Mathematical Proceedings of the Cambridge Philosophical Society*, Vol. 31 (Cambridge University Press, 1935) pp. 555–563.

[18] K. Vogel and H. Risken, *Determination of quasiprobability distributions in terms of probability distributions for the rotated quadrature phase,* Physical Review A **40**, 2847 (1989).

[19] J. B. Altepeter, E. R. Jeffrey, and P. G. Kwiat, *Photonic state tomography,* Advances in Atomic, Molecular, and Optical Physics **52**, 105 (2005).

[20] J. S. Bell, *On the Einstein Podolsky Rosen paradox,* Physics Physique Fizika **1**, 195 (1964).

[21] J. F. Clauser, M. A. Horne, A. Shimony, and R. A. Holt, *Proposed experiment to test local hidden-variable theories,* Physical Review Letters **23**, 880 (1969).

[22] C. H. Bennett, G. Brassard, C. Crépeau, R. Jozsa, A. Peres, and W. K. Wootters, *Teleporting an unknown quantum state via dual classical and einstein-podolsky-rosen channels,* Physical Review Letters **70**, 1895 (1993).

[23] N. Lütkenhaus, J. Calsamiglia, and K.-A. Suominen, *Bell measurements for teleportation,* Physical Review A **59**, 3295 (1999).

[24] W. P. Grice, *Arbitrarily complete bell-state measurement using only linear optical elements,* Physical Review A **84**, 042331 (2011).

[25] Y.-H. Kim, S. P. Kulik, and Y. Shih, *Quantum teleportation of a polarization state with a complete bell state measurement,* Physical Review Letters **86**, 1370 (2001).

[26] M. Zukowski, A. Zeilinger, M. A. Horne, and A. K. Ekert, *"event-ready-detectors"bell experiment via entanglement swapping,* Physical Review Letters **71**, 4287 (1993).

[27] N. Sangouard, C. Simon, H. De Riedmatten, and N. Gisin, *Quantum repeaters based on atomic ensembles and linear optics,* Reviews of Modern Physics **83**, 33 (2011).

[28] C. Simon, H. De Riedmatten, M. Afzelius, N. Sangouard, H. Zbinden, and N. Gisin, *Quantum repeaters with photon pair sources and multimode memories,* Physical Review Letters **98**, 190503 (2007).

[29] N. Sinclair, E. Saglamyurek, H. Mallahzadeh, J. A. Slater, M. George, R. Ricken, M. P. Hedges, D. Oblak, C. Simon, W. Sohler, *et al.*, *Spectral multiplexing for scalable quantum photonics using an atomic frequency comb quantum memory and feed-forward control,* Physical Review Letters **113**, 053603 (2014).

[30] M. G. Puigibert, G. Aguilar, Q. Zhou, F. Marsili, M. Shaw, V. Verma, S. Nam, D. Oblak, and W. Tittel, *Heralded single photons based on spectral multiplexing and feed-forward control,* Physical Review Letters **119**, 083601 (2017).

[31] S. Massar and S. Popescu, *Optimal extraction of information from finite quantum ensembles,* Physical Review Letter **74**, 1259 (1995).

[32] M. Fleischhauer and M. D. Lukin, *Dark-state polaritons in electromagnetically induced transparency,* Physical Review Letters **84**, 5094 (2000).

[33] A. Kozhekin, K. Mølmer, and E. Polzik, *Quantum memory for light,* Physical Review A **62**, 033809 (2000).

[34] S. Moiseev and S. Kröll, *Complete reconstruction of the quantum state of a single-photon wave packet absorbed by a doppler-broadened transition,* Physical Review Letters **87**, 173601 (2001).

[35] B. Kraus, W. Tittel, N. Gisin, M. Nilsson, S. Kröll, and J. Cirac, *Quantum memory for nonstationary light fields based on controlled reversible inhomogeneous broadening,* Physical Review A **73**, 020302 (2006).

[36] A. L. Alexander, J. J. Longdell, M. J. Sellars, and N. B. Manson, *Photon echoes produced by switching electric fields,* Physical Review Letters **96**, 043602 (2006).

[37] R. H. Dicke, *Coherence in spontaneous radiation processes,* Physical review **93**, 99 (1954).

[38] M. Afzelius, C. Simon, H. De Riedmatten, and N. Gisin, *Multimode quantum memory based on atomic frequency combs,* Physical Review A **79**, 052329 (2009).

[39] N. Sangouard, C. Simon, J. Minář, M. Afzelius, T. Chaneliere, N. Gisin, J.-L. Le Gouët, H. de Riedmatten, and W. Tittel, *Impossibility of faithfully storing single photons with the three-pulse photon echo,* Physical Review A **81**, 062333 (2010).

[40] M. Afzelius and C. Simon, *Impedance-matched cavity quantum memory,* Physical Review A **82**, 022310 (2010).

[41] M. Sabooni, Q. Li, S. Kröll, and L. Rippe, *Efficient quantum memory using a weakly absorbing sample,* Physical Review Letters **110**, 133604 (2013).

[42] E. Saglamyurek, J. Jin, V. B. Verma, M. D. Shaw, F. Marsili, S. W. Nam, D. Oblak, and W. Tittel, *Quantum storage of entangled telecom-wavelength photons in an erbium-doped optical fibre,* Nature Photonics **9**, 83 (2015).

[43] L.-M. Duan, M. Lukin, J. I. Cirac, and P. Zoller, *Long-distance quantum communication with atomic ensembles and linear optics,* Nature **414**, 413 (2001).

[44] M. Hosseini, B. M. Sparkes, G. Campbell, P. K. Lam, and B. C. Buchler, *High efficiency coherent optical memory with warm rubidium vapour,* Nature communications **2**, 174 (2011).

[45] P. Sekatski, N. Sangouard, N. Gisin, H. De Riedmatten, and M. Afzelius, *Photon-pair source with controllable delay based on shaped inhomogeneous broadening of rare-earth-metal-doped solids,* Physical Review A **83**, 053840 (2011).

[46] P. M. Ledingham, W. R. Naylor, J. J. Longdell, S. E. Beavan, and M. J. Sellars, *Nonclassical photon streams using rephased amplified spontaneous emission,* Physical Review A **81**, 012301 (2010).

[47] V. Damon, M. Bonarota, A. Louchet-Chauvet, T. Chaneliere, and J.-L. Le Gouët, *Revival of silenced echo and quantum memory for light,* New Journal of Physics **13**, 093031 (2011).

[48] L. Ma, O. Slattery, and X. Tang, *Optical quantum memory based on electromagnetically induced transparency,* Journal of Optics **19**, 043001 (2017).

[49] C. Laplane, P. Jobez, J. Etesse, N. Gisin, and M. Afzelius, *Multimode and long-lived quantum correlations between photons and spins in a crystal,* Physical Review Letters **118**, 210501 (2017).

[50] K. Kutluer, M. Mazzera, and H. de Riedmatten, *Solid-state source of nonclassical photon pairs with embedded multimode quantum memory,* Physical Review Letters **118**, 210502 (2017).

[51] J. Dajczgewand, *Optical memory in an erbium doped crystal: efficiency, bandwidth and noise studies for quantum memory applications*, Ph.D. thesis, Université Paris-Saclay (2015).

[52] S.-J. Yang, X.-J. Wang, X.-H. Bao, and J.-W. Pan, *An efficient quantum light–matter interface with sub-second lifetime,* Nature Photonics **10**, 381 (2016).

[53] Y. Wang, J. Li, S. Zhang, K. Su, Y. Zhou, K. Liao, S. Du, H. Yan, and S.-L. Zhu, *Efficient quantum memory for single-photon polarization qubits,* Nature Photonics , 1 (2019).

[54] G. Heinze, C. Hubrich, and T. Halfmann, *Stopped light and image storage by electromagnetically induced transparency up to the regime of one minute,* Physical Review Letters **111**, 033601 (2013).

[55] J. Guo, X. Feng, P. Yang, Z. Yu, L. Chen, C.-H. Yuan, and W. Zhang, *High-performance raman quantum memory with optimal control in room temperature atoms,* Nature communications **10**, 148 (2019).

[56] D. England, P. Michelberger, T. Champion, K. Reim, K. Lee, M. Sprague, X. Jin, N. Langford, W. Kolthammer, J. Nunn, *et al.*, *High-fidelity polarization storage in a gigahertz bandwidth quantum memory,* Journal of Physics B: Atomic, Molecular and Optical Physics **45**, 124008 (2012).

[57] B. Sparkes, J. Bernu, M. Hosseini, J. Geng, Q. Glorieux, P. A. Altin, P. K. Lam, N. Robins, and B. Buchler, *Gradient echo memory in an ultra-high optical depth cold atomic ensemble,* New Journal of Physics **15**, 085027 (2013).

[58] N. Maring, K. Kutluer, J. Cohen, M. Cristiani, M. Mazzera, P. M. Ledingham, and H. de Riedmatten, *Storage of up-converted telecom photons in a doped crystal,* New Journal of Physics **16**, 113021 (2014).

[59] P. Jobez, I. Usmani, N. Timoney, C. Laplane, N. Gisin, and M. Afzelius, *Cavity-enhanced storage in an optical spin-wave memory,* New Journal of Physics **16**, 083005 (2014).

[60] P. Jobez, C. Laplane, N. Timoney, N. Gisin, A. Ferrier, P. Goldner, and M. Afzelius, *Coherent spin control at the quantum level in an ensemble-based optical memory,* Physical Review Letters **114**, 230502 (2015).

[61] Y.-W. Cho, G. Campbell, J. Everett, J. Bernu, D. Higginbottom, M. Cao, J. Geng, N. Robins, P. Lam, and B. Buchler, *Highly efficient optical quantum memory with long coherence time in cold atoms,* Optica **3**, 100 (2016).

3

OPTICAL DECOHERENCE AND SPECTRAL DIFFUSION IN AN ERBIUM-DOPED SILICA GLASS FIBER FEATURING LONG-LIVED SPIN SUBLEVELS

Lucile Veissier*, Mohsen Falamarzi*, Thomas Lutz, Erhan Saglamyurek, Charles W. Theil, Rufus L. Cone, Wolfgang Tittel

Understanding decoherence in cryogenically-cooled rare-earth-ion doped glass fibers is of fundamental interest and a prerequisite for applications of these material in quantum information applications. Here we study the coherence properties in a weakly doped erbium silica glass fiber motivated by our recent observation of efficient and long-lived Zeeman sublevel storage in this material and by its potential for applications at telecommunication wavelengths. We analyze photon echo decays as well as the potential mechanisms of spectral diffusion that can be caused by coupling with dynamic disorder modes that are characteristic for glassy hosts, and by the magnetic dipole-dipole interactions between Er^{3+} *ions. We also investigate the effective linewidth as a function of magnetic field, temperature and time, and then present a model that describes these experimental observations. We highlight that the operating conditions (0.6 K and 0.05 T) at which we previously observed efficient spectral hole burning coincide with those for narrow linewidths*

The results of this chapter have been published in Phys. Rev. B **94**, 195138 (2016).

*Equally contributing authors.

(1 MHz) – an important property for applications that has not been reported before for a rare-earth-ion doped glass.

3.1. INTRODUCTION

Cryogenically-cooled rare-earth-ion (REI) doped materials offer unique spectroscopic properties, such as narrow optical linewidths and long-lived shelving levels that allow for spectral tailoring of their inhomogeneously broadened absorption lines. These properties are required simultaneously in order to implement many of the potential applications of REI-doped materials, including optical quantum memories [1, 2], as well as classical and quantum signal processing [3, 4]. Compared to crystals, the properties of REI's in amorphous hosts are generally very different because of the intrinsic disorder of the environment. This disorder comes with some advantages, in particular larger inhomogeneous broadening that is required for high-bandwidth or spectrally multiplexed applications. Furthermore, the increased inhomogeneous broadening of electron and nuclear spin transitions can inhibit spin diffusion that leads to decoherence [5]. This reduction was a key factor in our recent observation of efficient optical pumping into Zeeman sublevels with spin lifetimes reaching 30 s in an erbium-doped fiber [6]. However, in addition to long-term storage mechanisms, another prerequisite for the above-mentioned applications is a narrow homogeneous linewidth. REI-doped amorphous materials generally exhibit much larger homogeneous linewidths at liquid helium temperatures compare to REI-doped crystalline hosts due to interactions with dynamic fluctuations in the environment that are traditionally modeled as bistable two-level systems (TLS) [7, 8].

Motivated by our recent observation of slow spin relaxation [6] in a weakly-doped erbium-doped fiber that has allowed storing members of entangled photon pairs [9], we now investigate coherence properties of such a fiber with special attention to the regime of low magnetic fields where long Zeeman lifetimes were observed. More precisely, we report the magnetic field and temperature dependence of the optical coherence using two pulse photon echo (2PPE) and three pulse photon echo (3PPE) techniques. The fiber studied here has very similar composition and Er-doping concentration as the one used in our previous studies [6, 9]. In particular, both fibers feature long-lived persistent spectral holes with very similar characteristics.

Our paper is organized as follows. First, we discuss the results of the 2PPE measurements including the observed non-exponential echo decays in the context of spectral diffusion. We then present a detailed analysis describing the observed behaviors that combines elements from theoretical and semi-empirical models that have been developed in the past for glassy and crystalline hosts. In agreement with results of previous studies [10, 11], we find that coupling with TLS significantly limits the coherence lifetimes to less than 1 μs even at high magnetic fields and temperatures as low as 600 mK. However, an important new finding is that the best coherence properties exist at weak magnetic fields of around 0.05 T that also correspond to the optimal configuration for persistent spectral hole burning in this material [6]. This result is highly desirable for applications requiring both long coherence times as well as long spin state lifetimes.

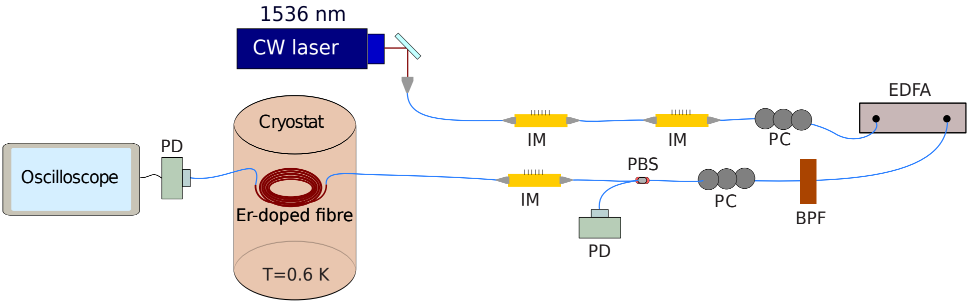

Figure 3.1: 2PPE (or 3PPE) experimental setup. CW laser, IM, PC, EDFA, BPF, PBS, and PD stand for continuous wave laser, polarization controller, erbium-doped fiber amplifier, band-pass filter, polarizing beam-splitter, and photodetector, respectively. See the text for the setup description.

3.2. EXPERIMENTAL DETAILS

Our fiber (INO Canada, S/N 404-28565) features an Er^{3+} doping concentration of 80 ppm and a length of 25 m. It is cooled to a minimum temperature $T = 600$ mK in an adiabatic demagnetization refrigerator, resulting in an optical depth of $\alpha L = 1.6$ at a wavelength $\lambda = 1536$ nm. Magnetic fields B of up to 2 T can be applied by means of a superconducting solenoid.

To perform the 2PPE (or 3PPE) measurements, we used two fiber-coupled electro-optic modulators to generate excitation pulses from a continuous wave external-cavity diode laser operating at $\lambda = 1536$ nm. The light was then amplified using an erbium-doped fiber amplifier (EDFA). In order to suppress spontaneously emitted and amplified light from the EDFA, we filtered the output in polarization with a polarizing beam-splitter, in frequency with a 1 nm band-pass filter, and in time using an additional intensity modulator before sending the excitation pulses into the Er^{3+}-doped fiber. The first pulse was 4 ns long, and the duration of the second (and third in case of 3PPE) pulse was 8 ns. All pulses emerging from the fiber were detected with an amplified photodetector (Newport AD-200xr) (a schematic of our experimental setup is shown in Fig. 3.1.). Since any persistent hole-burning will affect the echo signal strength, we ensured that the repetition period of the experiment exceeds the characteristic (magnetic field dependent [6]) persistence lifetime.

3.3. TWO-PULSE PHOTON ECHO MEASUREMENTS – ANALYSIS AND MODEL

The optical coherence properties of the fiber can be extracted from two-pulse photon echo measurements. In a 2PPE sequence, two short pulses, separated by a waiting time t_{12} are sent into an inhomogeneously-broadened ensemble of absorbers. This gives rise to the emission of an echo at time t_{12} after the second pulse. The variation of its intensity as a function of t_{12}

$$I(t_{12}) = I_0\, e^{-4\pi\Gamma_\mathrm{h} t_{12}} \tag{3.1}$$

reveals the homogeneous linewidth Γ_h (which is inversely proportional to the coherence lifetime: $\Gamma_\mathrm{h} = 1/(\pi T_2)$) assuming that all absorbers have the same coherence properties.

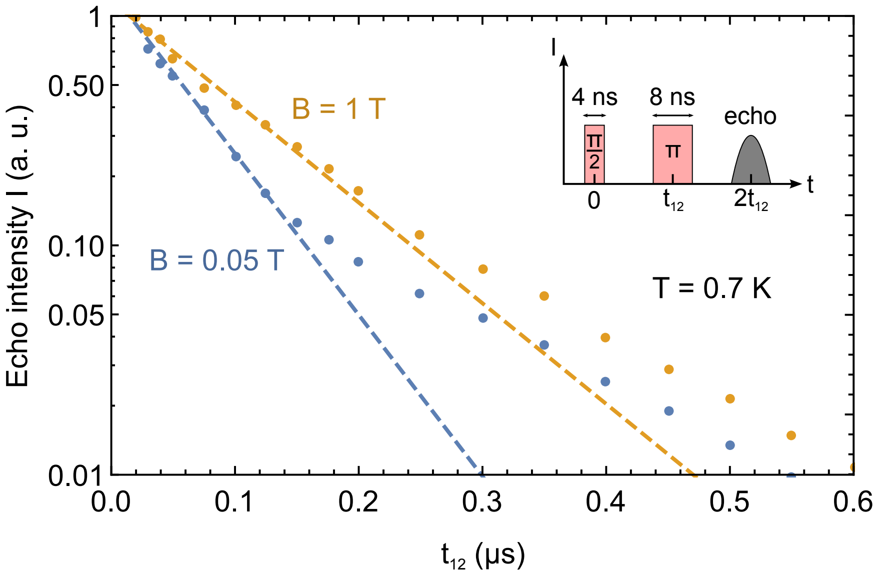

Figure 3.2: Two-pulse photon echo peak intensity as a function of the time delay between the two excitation pulses at $T = 0.7$ K for $B = 0.05$ T (blue dots) and $B = 1$ T (yellow dots). The pulse sequence is shown in the inset. The experimental data are fitted by a single-exponential function (dashed lines) with characteristic decay constants $T_2 = 247 \pm 14$ ns and $T_2 = 396 \pm 16$ ns.

Fig. 3.2 shows typical examples of the echo intensity as a function of the pulse separation t_{12} for $B = 0.05$ T and $B = 1$ T. The echo decays clearly show a non-exponential behavior: they deviate from a single exponential fit (see dashed lines) roughly at $t_{12} \geq 0.2$ μs, and feature a slower decay after this point. This differs from what has been observed in previous investigations of coherence properties in Er-doped fibers, where simple exponential decays were reported [11, 12] – most likely because the dynamic range of the echo decays was less in those past studies. In our case, the experimental echo decays can be fitted by the sum of multiple exponential functions, which could suggest several classes of ions with distinct coupling strengths to their environment, or several distinct perturbing processes. That is not a likely explanation for an amorphous host where a random distribution of different site environments would be expected.

Due to the amorphous nature of the fiber, we expect a broad, continuous distribution of coherence-limiting processes to affect the Er^{3+} ions. Of particular importance are changes in the local electric or magnetic field at the Er^{3+} ion position; they result in time-dependent shifts of its optical transition frequency – so-called spectral diffusion – which is taken into account by using an effective homogeneous linewidth Γ_{eff}. As depicted in Fig. 3.3, these shifts can arise due to interactions with neighboring TLS's (or tunneling modes) and Er-spins, each having two states with a certain energy splitting and randomly fluctuating between those states at a certain local rate [13, 14].

Two-level systems[7, 8] are intrinsic to amorphous materials and are present with a continuous distribution of flip rates R and energy splittings E that both depend on the asymmetry energy Δ, well separation L, and barrier energy V_0 (see inset of Fig. 3.3), as

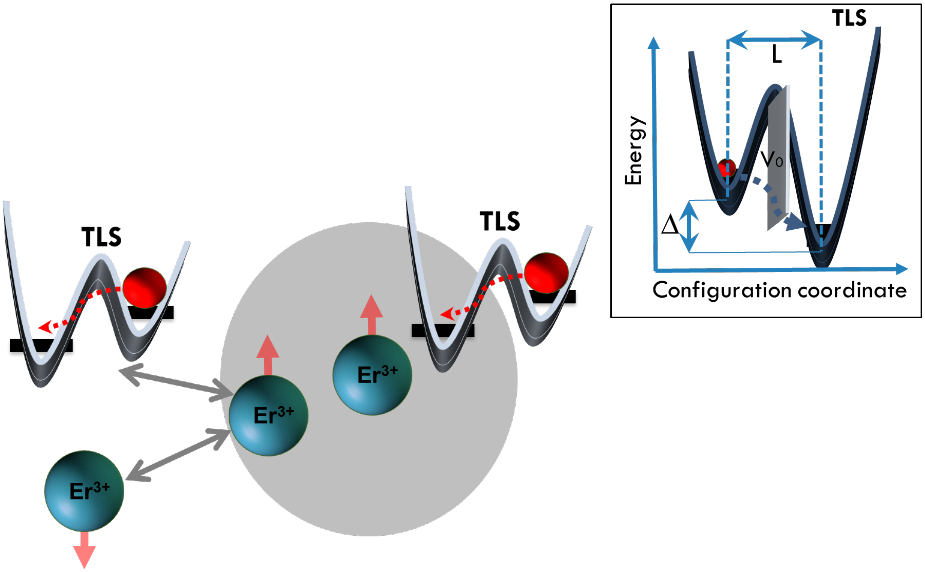

Figure 3.3: Spectral diffusion processes in a rare-earth ion doped glass. The local environments of the optically probed Er^{3+} ions in the center of the grey circle are perturbed by either direct interaction with fluctuations in the state of neighboring TLS (depicted on the right-hand side), or interaction with fluctuations in the state of other Er^{3+} spins in the local environment driven by TLS or another Er^{3+} ion. Inset: double-well potential-energy structure of the TLS, with asymmetry energy Δ, barrier energy V_0 and well separation L.

well as on the magnetic field in certain cases (so-called spin-elastic or magnetic TLS's) [11, 12, 15]. Thus, the calculation of the intensity of a 2PPE must include integration over a continuous distribution of rates and energy splittings:

$$I(t_{12}) = I_0 \int\int e^{-4\pi\Gamma_{\mathrm{eff}}(R,E,T,t)\,t_{12}}\, dR\, dE\,, \tag{3.2}$$

where

$$\Gamma_{\mathrm{eff}}(R,E,T,t) = \Gamma_0(T) + \Gamma_{\mathrm{SD}}(E,T)P(R,E)(1-e^{Rt})\,. \tag{3.3}$$

$\Gamma_0(T)$ is the intrinsic homogeneous linewidth (without spectral diffusion), and the spectral diffusion linewidth Γ_{SD} is given by

$$\Gamma_{\mathrm{SD}}(E,T) = \Gamma_{max}\, sech^2\left(\frac{E}{2kT}\right). \tag{3.4}$$

Here, Γ_{max} is the maximum possible linewidth broadening caused by spectral diffusion, k the Boltzmann constant, and T the temperature [16]. Furthermore, the probability distribution for finding a TLS with energy E and flipping rate R, $P(R,E)$, is given by

$$P(R,E) = \frac{1}{R\sqrt{1-R/R_{\mathrm{max}}(E)}}\,, \tag{3.5}$$

with $R_{\max}(E) \propto E^3 \coth\left(\frac{E}{2kT}\right)$ [17]. In the case of interactions with a magnetic TLS or the spin of another Er^{3+} ion, the energy E is given by $g\mu_B B$, where g is the effective g-value for the perturbing TLS or Er-ion, μ_B the Bohr magneton, and B the applied magnetic field. Using Eq. 3.2, one can fit the echo decays individually with Γ_{eff} by including the sum of five individual processes: spectral diffusion due to direct interaction of the optically resonant Er^{3+} ions with a non-magnetic (process 1) or magnetic (process 2) TLS; spectral diffusion due to interaction of the optically resonant Er^{3+} ions with a pair of coupled Er^{3+} spins in the environment (process 3) that randomly exchange spin states (Er^{3+}-Er^{3+} spin flip flops); and spectral diffusion due to interaction of the optically resonant Er^{3+} ions with a non-resonant Er^{3+} spin that is strongly coupled to a magnetic (process 4) or non-magnetic (process 5) TLS that drives spin flips (i.e. Er^{3+}-TLS flip flops). Due to the data set being limited in size and quality as well as computational complexity, we did not succeed in fitting all echo decays with one unique set of model parameters. However, as we will describe next, restricting the coherence-limiting processes to (1), (3) and (4), we were able to reproduce the magnetic field and temperature dependence of the single-exponential fits to our data shown in Fig.3.2 for the effective homogeneous linewidth $\Gamma_{\text{eff}}(B,T)$.

3.4. TEMPERATURE AND MAGNETIC FIELD DEPENDENCE OF THE EFFECTIVE HOMOGENEOUS LINEWIDTH

To extract the effective homogeneous linewidth as a function of magnetic field and temperature, we fit all measured echo decays using the single exponential function described in Eq. 3.2 (after replacing Γ_h with Γ_{eff}). These fits describe the coherence data over the first decade of the decays, thereby restricting the assessment of coherence-limiting processes to that region of the data; nevertheless, we should note that the first decade of the decay represents the dominant decoherence mechanisms that are primarily responsible for the performance in applications, with the different behaviors observed at longer times resulting from either higher-order processes and correlations or groups of minority ion sites in the material.

In Figs. 3.4 and 3.5 we plot examples of the experimentally obtained effective linewidth Γ_{eff} as a function of magnetic field for a fixed temperature and as a function of temperature for two different magnetic fields. In the case of varying magnetic field (Fig. 3.4), we observe two components. The first one is magnetic field independent and has been attributed to dephasing due to non-magnetic, or elastic, TLS [11, 12]. At 0.7 K its contribution to the Er^{3+} homogeneous linewidth in our fiber is roughly 0.75 MHz. The second component is magnetic field dependent: it dominates at small magnetic fields and is rapidly suppressed as the field increases. This behavior has been attributed to spectral diffusion due to the interaction of Er^{3+} ions with magnetic TLS [11, 12], or other Er^{3+} ions in the environment [15]. The latter process is regularly observed in Er^{3+}-doped crystals [18–20]. In the region of low magnetic field, we observe a local minimum at $B \approx 0.05$ T, followed by a local maximum at $B \approx 0.15$ T. This behavior is similar to what has been observed in Er^{3+}-doped crystals, such as Er^{3+}:$LiNbO_3$ and Er^{3+}:KTP [19, 20], and can be explained by the competition between two mechanisms: the interaction between Er^{3+} ions, which decreases with B, and the interaction between Er^{3+} ions and resonant TLS,

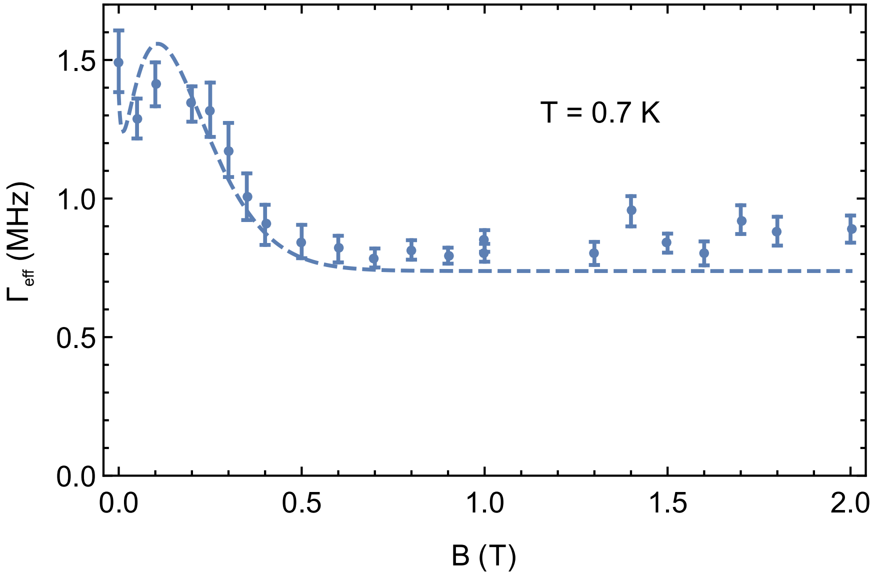

Figure 3.4: Magnetic field dependence of the effective homogeneous linewidth Γ_{eff} at $T = 0.7 \pm 0.05$ K. The dashed lines shows the theoretical prediction of Eq. 3.6 with the set of parameters in Table 3.1.

which increases with B according to the TLS density of states [6].

Investigating Γ_{eff} at low and high magnetic fields as a function of temperature (Fig. 3.5), we observe that both components increase nearly linearly with temperature. This agrees with the characteristic behavior of TLS-limited coherence [21], in which the effective linewidth is proportional to T^n, with values of n reported between 1 and 1.5 [11–13].

3.4.1. SPECTRAL DIFFUSION MODEL

Next, we fit the effective linewidths using a model that takes into account the three processes described previously (1, 3, and 4). Our model combines what has been proposed for amorphous media [21] and crystals (in particular in the case of Er:YSO [18]). We write the coherence lifetime as

$$T_2 = \frac{2\,(\Gamma_0 + \alpha_0 T^n)}{\Gamma_{\text{SD}} R} \left(\sqrt{1 + \frac{\Gamma_{\text{SD}} R}{\pi (\Gamma_0 + \alpha_0 T^n)^2}} - 1 \right). \tag{3.6}$$

Here, Γ_0 is the homogeneous linewidth at $T = 0$ K, α_0 is the constant describing the direct interaction with non-magnetic TLS (process 1), and $1 \leq n \leq 1.5$. The term $\frac{1}{2}\Gamma_{\text{SD}} R$ represents the shortening of the coherence lifetime through spectral diffusion caused by magnetic dipole-dipole interactions with surrounding Er^{3+} spins, which are flipped by neighboring Er-ions or TLS (processes 3 and 4). The associated flipping rate R can be described by

$$R(B,T) = \frac{\alpha_1}{\Gamma_{\text{S}}^0 + \gamma_{\text{S}} B}\, sech^2\left(\frac{g_{\text{env}} \mu_B B}{2kT}\right) + \alpha_2 B T. \tag{3.7}$$

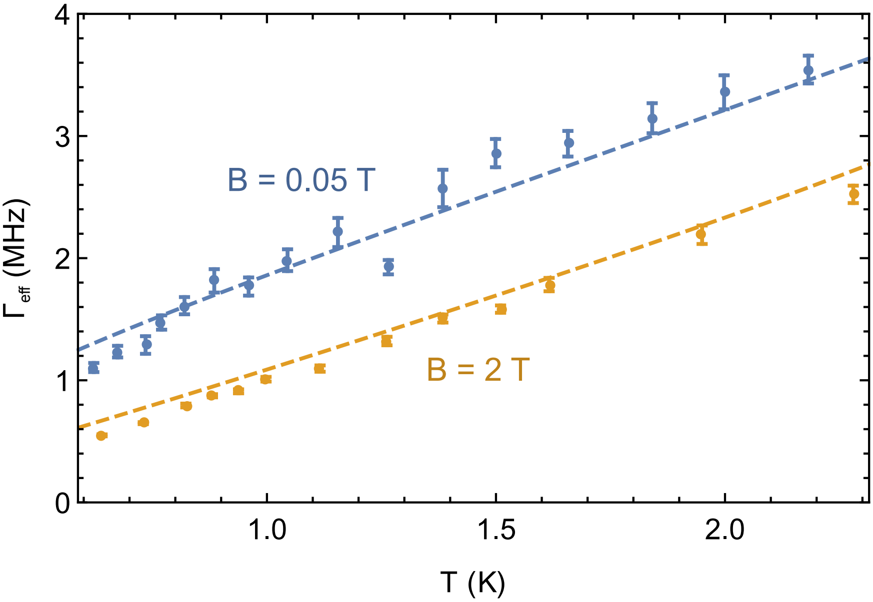

Figure 3.5: Temperature dependence of the effective homogeneous linewidth Γ_{eff} at $B = 0.05$ T and $B = 2$ T. The dashed lines shows the theoretical prediction of Eq. 3.6 with the set of parameters in Table 3.1.

The first term corresponds to spin flip-flops between Er^{3+} ions, with a coupling coefficient α_1 (process 3). We include broadening of the inhomogeneous linewidth Γ_{S} of the spin transition with magnetic field, i.e. $\Gamma_{S_0} = \Gamma_{\mathrm{S}}^0 + \gamma_{\mathrm{S}} B$, with $\Gamma_{\mathrm{S}}^0 = 1.5$ GHz and $\gamma_{\mathrm{S}} = 150$ GHz/T, as observed in our previous work on spin relaxation in erbium-doped fiber [6]. The second term corresponds to flip flops with magnetic TLS, with a coupling coefficient α_2 (process 4). While this effect is in some ways analogous to the coupling with phonons in crystals, we observed in the same previous work that it is proportional to B, i.e. does not have the same dependence on the magnetic field due to the difference in the density of states of the TLS [22]. The flip-flop rate increases with magnetic field for $B > 0.05$ T, which opposes the reduction of the linewidth Γ_{SD} with B, hence giving rise to the local maximum observed in the magnetic field dependence of the homogeneous linewidth (see Fig. 3.4). Fitting Eq. 3.6 to the magnetic field and temperature dependence of the homogeneous linewidth $\Gamma_{\mathrm{eff}}(B,T)$ results in the parameters listed in Table 3.1. The values of Γ_{S}^0 and γ_{S} have been fixed to the values found in our previous investigation of 1.5 GHz and 150 GHz/T, respectively [6].

The agreement between our model and the experimental data is exemplified by the data sets shown in Figs. 3.4 and 3.5. Furthermore, the value of 1.1 for the exponent n is in agreement with previous work [11–13], and the value of $g_{\mathrm{env}} = 14.4$, while large, is within the allowed range from 0 to 18 for the ${}^4\mathrm{I}_{15/2}$ levels of Er^{3+} ions [23–28]. We also note that the rate of Er^{3+} spin flips, characterized by α_1 and α_2, is on the order of MHz to GHz. However, our previous study of persistent spectral hole burning in a similar fiber established spin relaxation (i.e. spin flip) rates on the order of Hz [6]. We

Γ_0	(0.0 ± 0.5) MHz
α_0	(1.1 ± 0.5) MHz/T^n
n	1.1 ± 0.4
g_{env}	14.4 ± 1.6
$\alpha_1/\Gamma_{\text{max}}$	11 ± 5 GHz
$\alpha_2/\Gamma_{\text{max}}$	348 ± 42 (T K)$^{-1}$

Table 3.1: Parameters resulting from the 2-dimensional fit of Eq. 3.6 to $\Gamma_{\text{eff}}(B,T)$.

believe that this difference in behavior can be explained by the broad distribution of spin relaxation rates spanning the entire range from Hz to GHz. The coherence lifetime is limited by spectral diffusion that occurs at the fastest rate whereas the possibility for persistent spectral hole burning is determined by Er^{3+} ions with the slowest rates; in addition to causing spectral diffusion, the small fraction of rapidly relaxing ions leads the observed temperature-dependent limit on the maximum hole depth.

Overall, the coherence properties improve at low temperature and high magnetic fields, with an optimum of $\Gamma_{\text{eff}} = 0.55$ MHz at $T = 0.64$ K and $B = 2$ T (see Fig. 3.5). However, the broadening of the effective linewidth at magnetic fields around of 0.05 T (at which persistent spectral hole burning is possible) is small enough to allow linewidths of approximately 1 MHz at $T = 0.64$ K (see Fig. 3.5). This property has not been previously observed [10, 11], possibly due to differences in co-dopants (phosphorus in our fiber and lanthanum in the fiber studied in [10]). Another interesting observation is that the value for Γ_0 predicts a very narrow linewidth for $T \to 0$ K. However, this is only an extrapolation of our observations down to $T = 0.6$ K, and it is likely that other processes limit the linewidth to a constant value at lower temperatures.

3.5. THREE-PULSE PHOTON ECHO MEASUREMENTS – SPECTRAL DIFFUSION AT LONG TIMESCALES

Finally, to investigate spectral diffusion at timescales comparable to the excited-state lifetime of Er^{3+} (11 ms), 3PPE measurements were carried out at a temperature of $T = 0.76$ K. We chose two values of the magnetic field: $B = 0.06$ T for which the coherence lifetime exhibits a local maximum, and $B = 2$ T for which the effect of spectral diffusion due to Er^{3+}-Er^{3+} interaction is small and the coherence is limited by the interaction with TLS. For these measurements, the separation time t_{12} between the first two pulses was held constant at 50 ns and the echo intensity was measured as a function of the time t_{23} between the second and third pulse, with t_{23} varying between 0.001 ms and 35 ms. The echo intensity is given by

$$I(t_{12}, t_{23}) = I_0 \left\{ e^{-t_{23}/T_1} + \frac{\beta}{2} \frac{T_Z}{T_Z - T_1} \left(e^{-t_{23}/T_Z} - e^{-t_{23}/T_1} \right) \right\}^2 \times e^{-4\, t_{12} \pi \Gamma_{\text{eff}}(t_{12}, t_{23})}. \tag{3.8}$$

where I_0 is a scaling coefficient and β the branching ratio from the excited-level (with lifetime T_1) to the other Zeeman sublevel of the ground state (with lifetime T_Z) [18]. A fit to our data with $T_1 = 11$ ms yields the effective homogeneous linewidth Γ_{eff} that depends

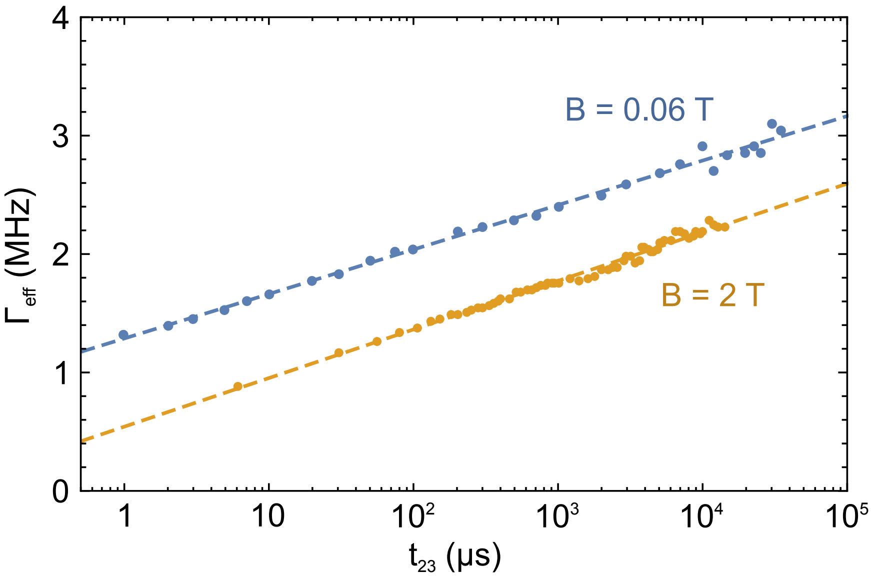

Figure 3.6: Effective homogeneous linewidth as a function of t_{23}, derived from 3PPE measurements at T = 0.76 K at B = 0.06 T (empty circles) and B = 2 T (filled circles). The experimental data is fitted by Eq. 3.8 with γ = 0.376 MHz/decade and 0.410 MHz/decade at B = 0.06 T and 2 T respectively.

on t_{12} and t_{23}.

The measurement results are shown in Fig. 3.6, which also includes fits of the expected logarithmic dependence of Γ_{eff} on t_{23} due to coupling to TLS in fiber [16, 29]:

$$\Gamma_{\text{eff}}(t_{12}, t_{23}) = \Gamma(t_0) + \gamma \log_{10}\left(\frac{t_{23}}{t_0}\right). \tag{3.9}$$

Here, $\Gamma(t_0)$ is the effective linewidth at the minimum value of $t_{12} + t_{23} \equiv t_0$, and γ is the coupling coefficient. The value of $\Gamma(t_0)$ is set to the one we measured in the 2PPE at the same magnetic field. We find excellent agreement for γ = 0.376 MHz/decade at B = 0.06 T and γ = 0.410 MHz/decade at 2 T. We find that, as in the case of short waiting times, our Er^{3+}-doped fiber features better coherence properties for small magnetic fields. Furthermore, effective linewidths at long waiting times barely improve when increasing the field to 2 T. This implies that spectral tailoring of the absorption profile with MHz resolution is possible even after large delays of up to hundreds of ms. In particular, this allows our fiber to be used as a quantum memory for light [9].

3.6. CONCLUSION

In conclusion, we have experimentally and theoretically investigated decoherence and spectral diffusion over a large range of timescales in an erbium-doped fiber similar to the one in which persistent hole burning has recently been demonstrated [6]. Our model combines the semi-empirical model framework developed for amorphous hosts, where spectral diffusion is caused by the interaction with two-level systems, and the theoretical framework successfully applied previously for Er^{3+}-doped crystals, where spectral diffusion is due to Er^{3+}-Er^{3+} magnetic dipole interactions. Most importantly, we found coherence lifetimes at small magnetic fields, at which Zeeman lifetimes can be as long as seconds, that are comparable to those at high magnetic fields. This is crucial for applications in the field of quantum information processing, in particular quantum memory for light [9].

3.7. ACKNOWLEDGMENTS

The authors thank Daniel Oblak and Neil Sinclair for discussions and acknowledge support from Alberta Innovates Technology Futures (AITF), the National Engineering and Research Council of Canada (NSERC), the US National Science Foundation (NSF) under award nos. PHY-1415628 and CHE-1416454, and the Montana Research and Economic Development Initiative. Furthermore, W.T. acknowledges support as a Senior Fellow of the Canadian Institute for Advanced Research (CIFAR).

REFERENCES

[1] W. Tittel, M. Afzelius, T. Chanelière, R. L. Cone, S. Kröll, S. Moiseev, and M. Sellars, *Photon-echo quantum memory in solid state systems,* Laser & Photonics Reviews **4**, 244 (2010).

[2] A. I. Lvovsky, B. C. Sanders, and W. Tittel, *Optical quantum memory,* Nature Photonics **3**, 706 (2009).

[3] C. W. Thiel, T. Böttger, and R. L. Cone, *Rare-earth-doped materials for applications in quantum information storage and signal processing,* Journal of Luminescence **131**, 353 (2011).

[4] E. Saglamyurek, N. Sinclair, J. A. Slater, K. Heshami, D. Oblak, and W. Tittel, *An integrated processor for photonic quantum states using a broadband light-matter interface,* New Journal of Physics **16**, 065019 (2014).

[5] C. Thiel, W. Babbitt, and R. Cone, *Optical decoherence studies of yttrium oxyorthosilicate Y_2SiO_5 codoped with Er^{3+} and Eu^{3+} for optical signal processing and quantum information applications at 1.5 microns,* Physical Review B **85**, 174302 (2012).

[6] E. Saglamyurek, T. Lutz, L. Veissier, M. P. Hedges, C. W. Thiel, R. L. Cone, and W. Tittel, *Efficient and long-lived Zeeman-sublevel atomic population storage in an erbium-doped glass fiber,* Physical Review B **92**, 241111 (2015).

[7] P. w. Anderson, B. I. Halperin, and C. M. Varma, *Anomalous low-temperature thermal properties of glasses and spin glasses,* Philosophical Magazine **25**, 1 (1972).

[8] W. A. Phillips, *Tunneling states in amorphous solids,* Journal of Low Temperature Physics **7**, 351 (1972).

[9] E. Saglamyurek, J. Jin, V. B. Verma, M. D. Shaw, F. Marsili, S. W. Nam, D. Oblak, and W. Tittel, *Quantum storage of entangled telecom-wavelength photons in an erbium-doped optical fibre,* Nature Photonics **9**, 83 (2015).

[10] R. M. Macfarlane, Y. Sun, P. B. Sellin, and R. L. Cone, *Optical decoherence in Er*$^{3+}$*-doped silicate fiber: evidence for coupled spin-elastic tunneling systems,* Physical Review Letters **96**, 033602 (2006).

[11] M. U. Staudt, S. R. Hastings-Simon, M. Afzelius, D. Jaccard, W. Tittel, and N. Gisin, *Investigations of optical coherence properties in an erbium-doped silicate fiber for quantum state storage,* Optics Communications **266**, 720 (2006).

[12] R. M. Macfarlane, Y. Sun, P. B. Sellin, and R. L. Cone, *Optical decoherence times and spectral diffusion in an Er-doped optical fiber measured by two-pulse echoes, stimulated photon echoes, and spectral hole burning,* Journal of Luminescence **127**, 61 (2007).

[13] M. M. Broer, B. Golding, W. H. Haemmerle, J. R. Simpson, and D. L. Huber, *Low-temperature optical dephasing of rare-earth ions in inorganic glasses,* Physical Review B **33**, 4160 (1986).

[14] J. L. Zyskind, E. Desurvire, J. W. Sulhoff, and D. J. D. Giovanni, *Determination of homogeneous linewidth by spectral gain hole-burning in an erbium-doped fiber amplifier with* GeO_2*:*SiO_2 *core,* IEEE Photonics Technology Letters **2**, 869 (1990).

[15] Y. Sun, R. L. Cone, L. Bigot, and B. Jacquier, *Exceptionally narrow homogeneous linewidth in erbium-doped glasses,* Optics Letters **31**, 3453 (2006).

[16] J. L. Black and B. I. Halperin, *Spectral diffusion, phonon echoes, and saturation recovery in glasses at low temperatures,* Physical Review B **16**, 2879 (1977).

[17] J. Jackle, *On the ultrasonic attenuation in glasses at low temperatures,* Zeitschrift fur Physik **257**, 212 (1972).

[18] T. Böttger, C. W. Thiel, Y. Sun, and R. L. Cone, *Optical decoherence and spectral diffusion at 1.5* μm *in* Er^{3+}*:*Y_2SiO_5 *versus magnetic field, temperature, and* Er^{3+} *concentration,* Physical Review B **73**, 075101 (2006).

[19] C. W. Thiel, R. M. Macfarlane, T. Böttger, Y. Sun, R. L. Cone, and W. R. Babbitt, *Optical decoherence and persistent spectral hole burning in* Er^{3+}*:*$LiNbO_3$*,* Journal of Luminescence **130**, 1603 (2010).

[20] T. Böttger, C. W. Thiel, Y. Sun, R. M. Macfarlane, and R. L. Cone, *Decoherence and absorption of* Er^{3+}*:*$KTiOPO_4$ *(KTP) at 1.5* μm*,* Journal of Luminescence **169, Part B**, 466 (2016).

[21] W. A. Phillips, *Two-level states in glasses,* Reports on Progress in Physics **50**, 1657 (1987).

[22] U. Buchenau, M. Prager, N. Nücker, A. J. Dianoux, N. Ahmad, and W. A. Phillips, *Low-frequency modes in vitreous silica,* Physical Review B **34**, 5665 (1986).

[23] H. Asatryan, R. Zakharchenya, A. Kutsenko, R. Babunts, and P. Baranov, *Electron paramagnetic resonance of* Er^{3+} *ions in a polycrystalline* α*-*Al_2O_3*,* Physics of the Solid State **49**, 1074 (2007).

[24] C. Ammerlaan and I. de Maat-Gersdorf, *Zeeman splitting factor of the* Er^{3+} *ion in a crystal field,* Applied Magnetic Resonance **21**, 13 (2001).

[25] T. Nolte, T. Pawlik, and J.-M. Spaeth, *EPR study of* Er^{3+} *in congruent* $LiNbO_3$*,* Solid state communications **104**, 535 (1997).

[26] D. Bravo and F. Lopez, *An electron paramagnetic resonance study of* Er^{3+} *in* $Bi_4Ge_3O_{12}$ *single crystals,* The Journal of chemical physics **99**, 4952 (1993).

[27] R. Reynolds, L. Boatner, C. Finch, A. Chatelain, and M. Abraham, *EPR investigations of* Er^{3+}*,* Yb^{3+}*, and* Gd^{3+} *in zircon-structure silicates,* The Journal of Chemical Physics **56**, 5607 (1972).

[28] A. Belyaeva, V. Eremenko, V. Pavlov, and A. Antonov, *Anisotropy of the g-tensor of the* Er^{3+} *ion in erbium-gallium garnet,* Optics and Spectroscopy **25**, 55 (1968).

[29] R. J. Silbey, J. M. A. Koedijk, and S. Völker, *Time and temperature dependence of optical linewidths in glasses at low temperature: Spectral diffusion,* The Journal of Chemical Physics **105**, 901 (1996).

4

ENTANGLEMENT AND NONLOCALITY BETWEEN DISPARATE SOLID-STATE QUANTUM MEMORIES MEDIATED BY PHOTONS

Marcel.li GRIMAU PUIGIBERT*, Mohsen FALAMARZI ASKARANI*, Jacob H. DAVIDSON, Varun B. VERMA, Matthew D. SHAW, Sae WOO NAM, Thomas LUTZ, Gustavo C. AMARAL*, Daniel OBLAK, Wolfgang TITTEL

Entangling quantum systems with different characteristics through the exchange of photons is a prerequisite for building future quantum networks. Proving the presence of entanglement between quantum memories for light working at different wavelengths furthers this goal. Here, we report on a series of experiments with a thulium-doped crystal, serving as a quantum memory for 794 nm photons, an erbium-doped fibre, serving as a quantum memory for telecommunication-wavelength photons at 1535 nm, and a source of photon pairs created via spontaneous parametric down-conversion. Characterizing the photons after re-emission from the two memories, we find non-classical correlations with a cross-correlation coefficient of $g_{12}^{(2)} = 53 \pm 8$*; entanglement preserving storage with input-output fidelity of* $\mathscr{F}_{IO} \approx 93 \pm 2\%$*; and non-locality featuring a violation of the Clauser-Horne-Shimony-Holt Bell-inequality with* $S = 2.6 \pm 0.2$*. Our proof-of-principle experiment shows that entanglement persists while propagating through different solid-state quantum memories operating at different wavelengths.*

This chapter has been submitted to Phys. Rev. Letter and posted on arXiv:1905.08184v2.

*Equally contributing authors.

4.1. INTRODUCTION

Entanglement is central to applications of quantum mechanics [1]. In particular, photon-mediated distribution of entanglement over different and widely spaced quantum systems underpins the creation of a future quantum network [2]. Various materials, devices and protocols are currently being studied towards this end [3–5], but, so far, there is no certainty about which elements will constitute its fundamental building blocks. However, it appears likely that they will operate within different wavelength regions, ranging from visible [6, 7] via near-infrared [8–13], to telecommunication wavelengths [14, 15]. This will allow leveraging the best properties of each device, and thereby offer heightened capabilities compared to a network consisting of identical quantum systems.

The development of such networks therefore creates a need, immediately and in the future, for hybridization experiments to bridge existing frequency and bandwidth mismatches. One example is linking quantum memories for light operating at different wavelengths through the exchange of photons. However, so far, only a few investigations have been reported [16–18], and none of them has included a quantum memory functioning at telecommunication wavelength.

In this work, we demonstrate entanglement between two atomic frequency comb (AFC)-based quantum memories [19] in ensembles of cryogenically-cooled rare-earth ions, one for 794 nm and one for 1535 nm wavelength photons. The first memory employs a thulium-doped lithium-niobate (Tm^{3+}:$LiNbO_3$) crystal, the second an erbium-doped fibre (Er^{3+}:SiO_2). Entanglement is created through the interaction with entangled photons created by spontaneous parametric down-conversion. Both memories allow buffering and re-emitting multiplexed quantum data in feed-forward-controlled spectral or temporal modes, either of which makes them suitable for quantum repeaters [20, 21]. It is significant that our experiment involves two classes of ions: Kramers and non-Kramers. Due to their specific electronic configurations, Kramer's ions are strongly coupled to the local magnetic environment while non-Kramer's ions are relatively immune to magnetic field fluctuations. These characteristics make Kramers ions strong candidates for quantum sensors while non-Kramers are generally more suitable for quantum memory with long storage time.

4.2. EXPERIMENTAL SETUP

Our experimental setup, outlined in Fig. 6.1 and further detailed in the Supplemental Material, consisted of four parts: a source of entangled photon pairs; two solid-state memories for light (one doped with thulium, and one with erbium); and a detection system comprising analyzers (including detectors), coincidence electronics and data processing software. Appropriate configuration of the source and detection system allowed measuring the cross-correlation function, reconstructing density matrices, and testing Bell inequalities with photon pairs before and after storage. To create time-bin entangled pairs of photons at 794 nm and 1535 nm wavelengths, short laser pulses at 523 nm and 80 MHz repetition rate (reference clock) were split by an unbalanced Mach-Zehnder (MZ) interferometer into early, e, and late, ℓ, temporal modes, and used to pump a non-linear crystal that is phase-matched for frequency non-degenerate spontaneous parametric down-conversion (SPDC). Assuming the annihilation of exactly one pump pho-

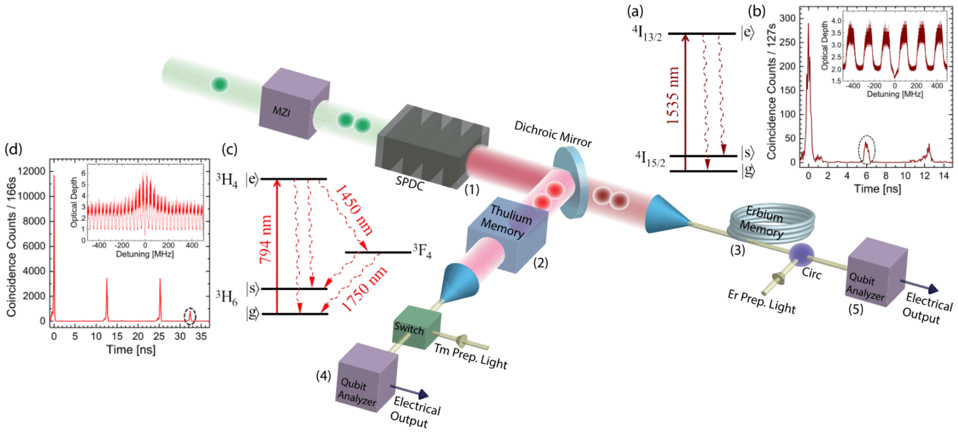

Figure 4.1: Photons from a photon-pair source (1) were directed to two different memories (2, 3), stored, and re-emitted. Analyzers (4, 5) allowed measuring the cross-correlation function, reconstructing density matrices, and testing a Bell inequality. A simplified erbium-level scheme is shown in (a). To create the AFC, erbium ions were frequency-selectively pumped from $|g\rangle$ via $|e\rangle$ into the long-lived level $|s\rangle$. The AFC peak spacing was ~166 MHz (yielding 6 ns storage time) and the total bandwidth was 8 GHz (the inset of (b) shows a 1-GHz-wide section). (b) shows the storage and retrieval of single photons at ~1535 nm wavelength in single temporal modes, heralded by the detection of 794 nm photons post-selected as coincidences with the reference clock signal (see the Supplemental Material). The coincidence peak at 0 ns is due to directly transmitted (non-stored) photons; the one at 6 ns (highlighted by a dashed circle) depicts stored and re-emitted photons. Photons created in subsequent pump laser cycles caused accidental coincidences at multiples of 12.5 ns. A simplified thulium level scheme is shown in (c). The AFC preparation was similar to that described for erbium. Equivalent measurements to those in (b) are shown in (d), but now for single photons at 794 nm heralded by detections of 1535 nm photons again post-selected. Note the accidental coincidence peaks at 12.5 and 25 ns. The whole AFC frequency range was 10 GHz (a 1-GHz-wide section is depicted in the inset), and the peak spacing ~31 MHz, resulting in 32-ns-long storage.

ton, the quantum state of the resulting photon pair is described by the so-called $|\phi^+\rangle$ Bell state

$$|\phi^+\rangle = \left(|ee\rangle + |\ell\ell\rangle\right)/\sqrt{2}, \tag{4.1}$$

where $|xy\rangle \equiv |x\rangle_{794} \otimes |y\rangle_{1535}$, with subscripts denoting each photon's wavelength[22]. The remaining pump light was removed, and the photons of different wavelengths were separated by a dichroic mirror and sent to separate rare-earth-ion-doped memories. In addition, their spectra were filtered to 8 GHz using an air-spaced etalon (for the 1535 nm photons) and 10 GHz using the inhomogeneously-broadened absorption line of Tm (for the 794 nm photons; see the Supplemental Material for details). We adjusted the paths of the photons such that their storage in the memories was temporally overlapped.

The Tm^{3+}:$LiNbO_3$ crystal, used for storing 794 nm photons, and the Er^{3+}:SiO_2 fibre, used for storing 1535 nm photons, were cooled to ~0.6 K and exposed to magnetic fields of 125 G and 1500 G, respectively. Under these conditions it is possible to tailor, by means of optical pumping, the inhomogeneously broadened absorption lines of each ensemble of rare-earth ions into a large number of spectrally equidistant absorption peaks separated by frequency Δ. This feature, known as an atomic frequency comb (AFC), was first described as a quantum memory in [19]. After a storage time $\tau = 1/\Delta$ the photon is re-emitted from the memory (for a short theoretical description of the storage protocol see the Supplemental Material). In our experiment, we prepared storage times of 32 ns and 6 ns, and memory bandwidths of 10 GHz and 8 GHz for the 794 nm and 1535 nm photons. Note that the short storage times were partly determined by the impossibility to independently optimize the magnetic fields to which the ensembles were exposed in a single cryostat (described in the Supplemental Material).

After re-emission, the photons were directed to analyzers consisting either of a short fibre or an interferometer featuring the same path-length difference as that acting on the pump pulses, and detected using superconducting nanowire single-photon detectors (SNSPDs) cooled to 0.8 K in a second cryostat. Finally, the resulting electronic signals were processed in a time-to-digital converter (TDC), and single-detector count rates as well as time-resolved coincidence count rates were recorded by a computer.

4.3. RESULTS

Initially, we characterized the source and the two memories individually. For this, we blocked the long arm of the pump interferometer such that the source produced pairs of photons in a single temporal mode. We measured the system storage efficiencies for heralded single photons for each memory, finding 0.1% for the Er-doped fibre and 0.4% for the Tm-doped crystal. Taking independently characterized input and output coupling efficiencies and transmission loss into account, the corresponding internal efficiencies were 0.5% and 2%. See Fig. 6.1 and Supplemental Material for more information.

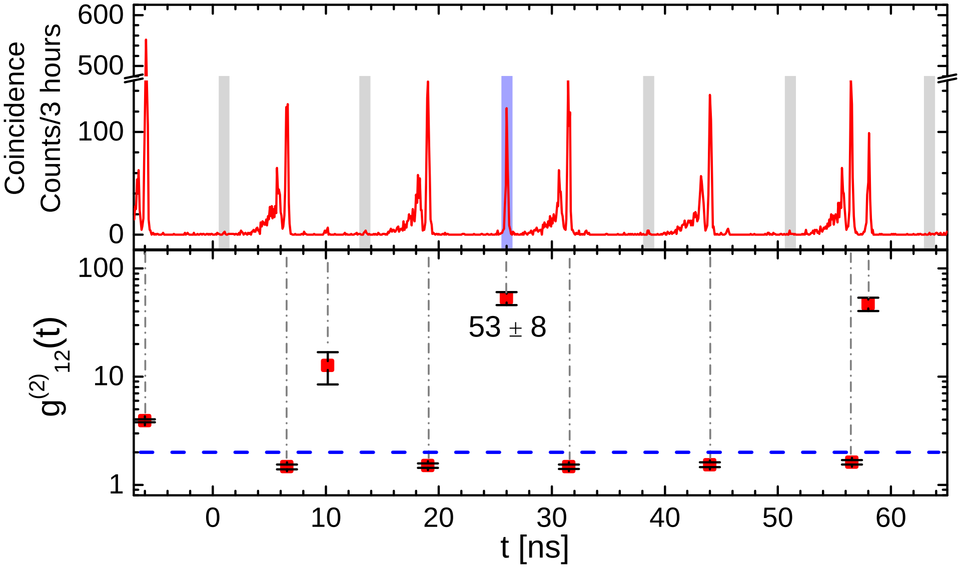

Figure 4.2: The upper panel shows the coincidence-detection histogram (within a 80 ps bin width) created by starting the TDC with the clock signal ANDed with re-emitted 1535 nm photon detection signals, and stopping it using all 794 nm photons detected after the Tm memory. In the lower panel, the red squares and the black error bars represent, respectively, $g^{(2)}_{12}(\delta t)$ and uncertainties (one standard deviation), calculated from the upper panel histogram. The blue-dashed line shows the maximum classical value of $g^{(2)}_{12}(\delta t) = 2$. Non-classical correlations between photons after storage can be seen at $\delta t = 26$ ns. (The rate R(26 ns) is highlighted using a blue bar, and R(26 ns + n · 12.5ns) using gray bars.) The points at $\delta t = 58$ ns and $\delta t = 10$ ns were caused by imperfections in the thulium AFC (see the Supplemental Material). The data at $\delta t = -6$ ns is due to transmitted (non-stored) 794 nm photons, and data at $\delta t = -6$ ns + n × 12.5 ns corresponds to accidental coincidences with transmitted 794 nm photons emitted in a subsequent pump laser cycle.

Then, with the long arm of the pump interferometer still blocked, we measured the cross correlation function $g_{12}^{(2)}(\delta t)$ of the photon pairs before storage in the memories (see the Supplemental Material for more information). Creating photons pairs using the highest pump power available, we found $g_{12}^{(2)}(0)$= 61±9, which exceeds the maximum value of 2 that is consistent with the assumption of classical fields [23] by 4.5 standard deviations (see Supplemental Material for additional measurements). This verifies the non-classical nature of the photon-pairs. Repeating the measurement with memories in place, we found $g_{12}^{(2)}(\delta t = 32\text{ ns} - 6\text{ ns} = 26\text{ ns})$=53±8 (shown in Fig. 4.2), where 32 ns and 6 ns denote the pre-set storage time of the thulium and erbium memories, respectively. This result demonstrates that non-classical correlations between the members of photon pairs were preserved during storage.

Next, we opened both arms of the pump interferometer, thereby creating the entangled state described in Eq. 4.1. We used two approaches to establish that the photons remain entangled after storage, and hence that we preserved the entanglement during storage in the distinct quantum memories.

First, we reconstructed the density matrices of the photon pairs before and after storage. This requires measuring a set of joint (bipartite) projectors (see Supplemental Material). Using a maximum likelihood estimation, the density matrices that best fit the measured projection probabilities were reconstructed; the results are shown in Fig 4.3. In turn, this allowed us to calculate the entanglement of formation, the purity, the fidelity of the measured states with the target state $|\phi^+\rangle$ in Eq. 4.1, and the fidelity between input and output states (see Supplemental Material for more information). These figures of merit, summarized in Table 4.1, confirm that the photons remained entangled.

Finally, we also performed a test of the CHSH Bell inequality [24], which states that the sum of four correlation coefficients $E(\alpha,\beta)$ is upper-bounded by two if the measurement results can be described by local theories:

$$S = |E(\alpha_1,\beta_1) + E(\alpha_1,\beta_2) + E(\alpha_2,\beta_1) - E(\alpha_2,\beta_2)| \leq 2.$$

Here, α_i and β_i denote different measurement settings – in our case phases set by analyzing interferometers. Using the data given in the Supplemental Material, we found S_{in}=2.52±0.02 before, and S_{out}=2.6±0.2 after storage, both of which significantly exceed 2.

Violating the CHSH Bell inequality (or any other Bell inequality) proves non-locality rather than entanglement. However, Bell tests allow certifying entanglement within a device-independent framework, that is without making assumptions about, e.g., the dimensions of the Hilbert spaces describing the individual quantum systems [25]. (Note that such certification requires the Bell test to be loophole free, while we made the common assumptions of fair sampling and no signaling.) As such, a Bell-inequality violation is a more stringent test of entanglement than finding positive values for the entanglement of formation.

	Entanglement of formation (%)	**Purity (%)**	**Fidelity with $|\phi^+\rangle$ (%)**	**Input-output fidelity (%)**
ρ_{in}	81.10±2.23	84.57±1.47	91.68±0.83	93.77±2.18
ρ_{out}	72.61±11.70	80.14±7.22	87.68±4.67	

Table 4.1: Values were calculated using the density matrices in Fig. 4.3, and uncertainties estimated using Monte-Carlo simulation.

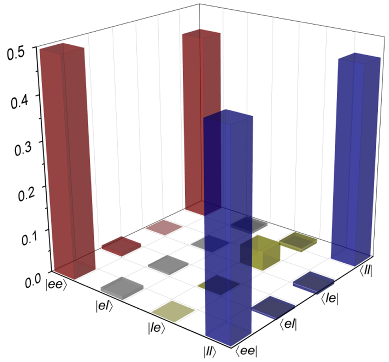

(a) ρ_{in} - before storage

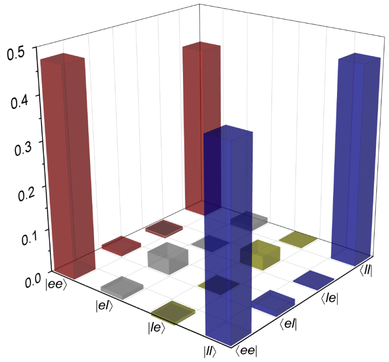

(b) ρ_{out} - after storage

Figure 4.3: Reconstructed density matrices of entangled time-bin qubits before and after storage. Only the real parts are shown (the absolute values of all imaginary parts are smaller than 0.023).

4.4. CONCLUSION AND DISCUSSION.

Our results show that entanglement persists while propagating through different solid-state quantum memories operating at different wavelengths. However, for future use in a quantum network, several factors must be improved. To increase the device efficiency and storage time of the memory for the 794 nm photons, the Tm^{3+}:$LiNbO_3$ crystal could be replaced by Tm^{3+}:$Y_3Ga_5O_{12}$ (Tm:YGG)[26], which features better coherence properties, inside an impedance-matched cavity [27]. Similarly, the erbium-doped fibre could be replaced by a ^{167}Er-doped Y_2SiO_5 crystal (Er:YSO) [28], again inside a cavity. For more information see the Supplemental Material.

4.5. ACKNOWLEDGEMENTS

The authors thank Erhan Saglamyurek and Neil Sinclair for discussions, and acknowledge funding through Alberta Innovates Technology Futures (AITF), the National Science and Engineering Research Council of Canada (NSERC), and the Netherlands Organization for Scientific Research (NWO). Furthermore, WT acknowledges funding as a Senior Fellow of the Canadian Institute for Advanced Research (CIFAR), and VBV and SWN partial funding for detector development from the Defense Advanced Research Projects Agency (DARPA) Information in a Photon (InPho) program. Part of the detector research was carried out at the Jet Propulsion Laboratory, California Institute of Technology, under a contract with the National Aeronautics and Space Administration (NASA).

REFERENCES

[1] R. Horodecki, P. Horodecki, M. Horodecki, and K. Horodecki, *Quantum entanglement,* Reviews of Modern Physics **81**, 865 (2009).

[2] S. Wehner, D. Elkouss, and R. Hanson, *Quantum internet: A vision for the road ahead,* Science **362**, eaam9288 (2018).

[3] A. I. Lvovsky, B. C. Sanders, and W. Tittel, *Optical quantum memory,* Nature Photonics **3**, 706 (2009).

[4] M. D. Eisaman, J. Fan, A. Migdall, and S. V. Polyakov, *Invited review article: Single-photon sources and detectors,* Review of Scientific Instruments **82**, 071101 (2011).

[5] N. Somaschi, V. Giesz, L. De Santis, J. Loredo, M. P. Almeida, G. Hornecker, S. L. Portalupi, T. Grange, C. Antón, J. Demory, *et al.*, *Near-optimal single-photon sources in the solid state,* Nature Photonics **10**, 340 (2016).

[6] B. Hensen, H. Bernien, A. E. Dréau, A. Reiserer, N. Kalb, M. S. Blok, J. Ruitenberg, R. F. Vermeulen, R. N. Schouten, C. Abellán, *et al.*, *Loophole-free bell inequality violation using electron spins separated by 1.3 kilometres,* Nature **526**, 682 (2015).

[7] M. P. Hedges, J. J. Longdell, Y. Li, and M. J. Sellars, *Efficient quantum memory for light,* Nature **465**, 1052 (2010).

[8] L. Li, Y. Dudin, and A. Kuzmich, *Entanglement between light and an optical atomic excitation,* Nature **498**, 466 (2013).

[9] Y. Yu, F. Ma, X.-Y. Luo, B. Jing, P.-F. Sun, R.-Z. Fang, C.-W. Yang, H. Liu, M.-Y. Zheng, X.-P. Xie, *et al.*, *Entanglement of two quantum memories via metropolitan-scale fibers,* arXiv preprint arXiv:1903.11284 (2019).

[10] E. Saglamyurek, N. Sinclair, J. Jin, J. A. Slater, D. Oblak, F. Bussieres, M. George, R. Ricken, W. Sohler, and W. Tittel, *Broadband waveguide quantum memory for entangled photons,* Nature **469**, 512 (2011).

[11] C. Clausen, I. Usmani, F. Bussières, N. Sangouard, M. Afzelius, H. de Riedmatten, and N. Gisin, *Quantum storage of photonic entanglement in a crystal,* Nature **469**, 508 (2011).

[12] L. Hanschke, K. A. Fischer, S. Appel, D. Lukin, J. Wierzbowski, S. Sun, R. Trivedi, J. Vučković, J. J. Finley, and K. Müller, *Quantum dot single-photon sources with ultra-low multi-photon probability,* npj Quantum Information **4**, 43 (2018).

[13] V. Krutyanskiy, M. Meraner, J. Schupp, V. Krcmarsky, H. Hainzer, and B. Lanyon, *Light-matter entanglement over 50 km of optical fibre,* npj Quantum Information (2019).

[14] E. Saglamyurek, J. Jin, V. B. Verma, M. D. Shaw, F. Marsili, S. W. Nam, D. Oblak, and W. Tittel, *Quantum storage of entangled telecom-wavelength photons in an erbium-doped optical fibre,* Nature Photonics **9**, 83 (2015).

[15] J.-H. Kim, T. Cai, C. J. Richardson, R. P. Leavitt, and E. Waks, *Two-photon interference from a bright single-photon source at telecom wavelengths,* Optica **3**, 577 (2016).

[16] M. Lettner, M. Mücke, S. Riedl, C. Vo, C. Hahn, S. Baur, J. Bochmann, S. Ritter, S. Dürr, and G. Rempe, *Remote entanglement between a single atom and a bose-einstein condensate,* Physical Review Letters **106**, 210503 (2011).

[17] N. Kalb, A. A. Reiserer, P. C. Humphreys, J. J. Bakermans, S. J. Kamerling, N. H. Nickerson, S. C. Benjamin, D. J. Twitchen, M. Markham, and R. Hanson, *Entanglement distillation between solid-state quantum network nodes,* Science **356**, 928 (2017).

[18] N. Maring, P. Farrera, K. Kutluer, M. Mazzera, G. Heinze, and H. de Riedmatten, *Photonic quantum state transfer between a cold atomic gas and a crystal,* Nature **551**, 485 (2017).

[19] M. Afzelius, C. Simon, H. De Riedmatten, and N. Gisin, *Multimode quantum memory based on atomic frequency combs,* Physical Review A **79**, 052329 (2009).

[20] N. Sinclair, E. Saglamyurek, H. Mallahzadeh, J. A. Slater, M. George, R. Ricken, M. P. Hedges, D. Oblak, C. Simon, W. Sohler, *et al.*, *Spectral multiplexing for scalable quantum photonics using an atomic frequency comb quantum memory and feed-forward control,* Physical Review Letters **113**, 053603 (2014).

[21] C. Simon, H. De Riedmatten, M. Afzelius, N. Sangouard, H. Zbinden, and N. Gisin, *Quantum repeaters with photon pair sources and multimode memories,* Physical Review Letters **98**, 190503 (2007).

[22] J. Brendel, N. Gisin, W. Tittel, and H. Zbinden, *Pulsed energy-time entangled twin-photon source for quantum communication,* Physical Review Letters **82**, 2594 (1999).

[23] A. Kuzmich, W. Bowen, A. Boozer, A. Boca, C. Chou, L.-M. Duan, and H. Kimble, *Generation of nonclassical photon pairs for scalable quantum communication with atomic ensembles,* Nature **423**, 731 (2003).

[24] J. F. Clauser, M. A. Horne, A. Shimony, and R. A. Holt, *Proposed experiment to test local hidden-variable theories,* Physical Review Letters **23**, 880 (1969).

[25] V. Scarani, *The device-independent outlook on quantum physics,* Acta Physica Slovaca **62**, 347 (2012).

[26] C. W. Thiel, N. Sinclair, W. Tittel, and R. Cone, Tm^{3+}*:*$Y_3Ga_5O_{12}$ *materials for spectrally multiplexed quantum memories,* Physical Review Letters **113**, 160501 (2014).

[27] M. Afzelius and C. Simon, *Impedance-matched cavity quantum memory,* Physical Review A **82**, 022310 (2010).

[28] M. Rančić, M. P. Hedges, R. L. Ahlefeldt, and M. J. Sellars, *Coherence time of over a second in a telecom-compatible quantum memory storage material,* Nature Physics **14**, 50 (2018).

5

PERSISTENT ATOMIC FREQUENCY COMB BASED ON ZEEMAN SUB-LEVELS OF AN ERBIUM-DOPED CRYSTALLINE WAVEGUIDE

Mohsen FALAMARZI ASKARANI, Thomas LUTZ, Marcel.li GRIMAU PUIGIBERT, Neil SINCLAIR, Daniel OBLAK, Wolfgang TITTEL

Long-lived sub-levels of the electronic ground-state manifold of rare-earth ions in crystals can be used as atomic population reservoirs for photon echo-based quantum memories. We measure the dynamics of the Zeeman sub-levels of erbium ions that are doped into a lithium niobate waveguide, finding population lifetimes at cryogenic temperatures as long as seconds. Then, using these levels, we prepare and characterize atomic frequency combs, which can serve as a memory for quantum light at 1532 nm wavelength. The results allow predicting a 0.1% memory efficiency, mainly limited by unwanted background absorption that we conjecture to be caused by the coupling between two-level systems (TLS) and erbium spins. Hence, while it should be possible to create an AFC-based quantum memory in Er^{3+}*:*Ti^{4+}*:*$LiNbO_3$*, improved crystal growth together with optimized AFC preparation will be required to make it suitable for applications in quantum communication.*

This chapter has been submitted to JOSA B and posted on arXiv:1907.07780v2.

5.1. INTRODUCTION

Cryogenically-cooled rare-earth-ion-doped (REI-doped) crystals have been extensively studied for their use in classical optical signal processing applications for several decades [1]. This is partially due to their convenient optical and spin-level structure, long population and coherence lifetimes, large inhomogeneous broadening, and their tunability with externally-applied fields [2]. More recently, this work has spawned applications in quantum signal processing, including photon echo-based quantum memories for light [3–9].

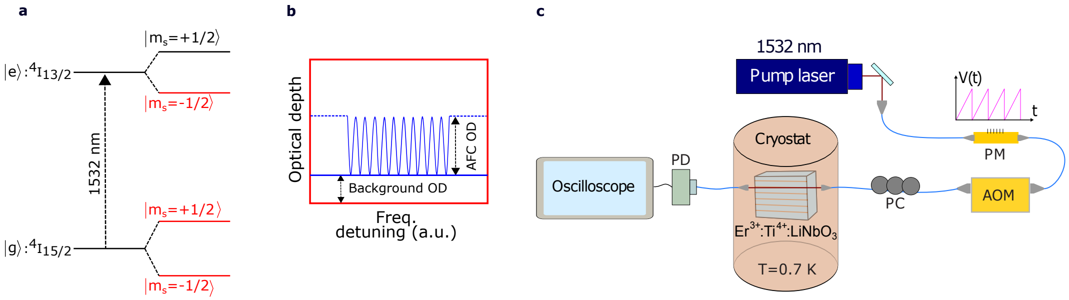

Figure 5.1: **a.** Simplified energy level structure of the $^4I_{15/2} \leftrightarrow {}^4I_{13/2}$ transition of Er^{3+}. Exited and ground levels are indicated with $|e\rangle$ and $|g\rangle$, respectively, and electronic Zeeman sub-levels with $|m_s = \pm 1/2\rangle$. To create an atomic frequency comb (a periodic modulation of the frequency-dependent optical depth into equally-spaced narrow peaks), persistent spectral holes are created (burned) by pumping all undesired population into shelving levels, *e.g.* $|g, m_s = +1/2\rangle$. **b.** An example of an AFC, showing the resulting spectral population grating. **c.** Experimental setup. Continuous-wave light at 1532 nm wavelength is directed through a phase-modulator (PM) and an acousto-optic modulator (AOM), which allow frequency and intensity modulation. After passing a polarization controller (PC), the light creates spectral holes and AFC structures in the erbium-doped lithium niobate waveguide, and furthermore allows probing previously created structures with the help of a photo-detector (PD) and an oscilloscope. The PM is driven by a serrodyne voltage V(t) modulation similar to that depicted in the plot.

Several such protocols, including the widely-employed atomic frequency comb (AFC) protocol [10], require frequency-selective optical pumping (or persistent spectral hole burning) of REIs into a long-lived energy level, referred to as a shelving level (see Fig.6.1a). Typically, this level is a spin (hyperfine) level within the electronic ground state manifold that features a much longer population lifetime than that of the optically-excited level. This allows waiting for excited atoms to decay at the end of the optical pumping sequence without loosing the spectral population grating in the ground state, which is key to quantum state storage with high fidelity and efficiency [11].

Among the REIs, Er^{3+} is the only one that features a transition from the ground level to an excited level at telecommunication wavelength of around 1.5 μm. Since Er^{3+} is a Kramer's ion, the ground level (more precisely, it's lowest-lying crystal field level) is split into two electronic Zeeman sub-levels under the application of a magnetic field. If a host crystal contains nuclear spins, these may couple to the Zeeman sub-levels of Er^{3+}, resulting in further splitting into superhyperfine levels [2]. Both Zeeman and superhyperfine levels are potentially useful as shelving levels for the AFC memory preparation, with the key requirement that they must feature a long population lifetime. But since the memory bandwidth assuming high-efficiency storage is limited by ground-state splitting, optical pumping into electronic Zeeman levels is preferred due to their larger splitting in a magnetic field.

Partially motivated by its remarkably long optical coherence lifetime of 4.4 ms [12], initial studies towards a telecommunication-wavelength quantum memory have focused on Er^{3+}:Y_2SiO_3 [13] and electronic Zeeman levels for spectral hole burning. However, their 130 ms population lifetime [14] (limited by Er^{3+} spin flip-flops [15]) in conjunction with 11 ms optical population lifetime have so far prevented reaching efficiencies in excess of 0.25 %. Later, AFC-based storage of entangled photons in an Er-doped SiO_2 fibre [16] was achieved by exploiting spin disorder, which reduces spin flip-flops between Zeeman levels compared to those in crystals. On the other hand, the amorphous nature of SiO_2 also leads to small optical coherence lifetimes, thereby restricting storage times to less than 100 nanoseconds. Furthermore, the disorder-induced inhomogeneous broadening of the spin-transition has limited storage efficiencies to similar values as in Er^{3+}:Y_2SiO_3 [17, 18]. More recently, storage of heralded single photons using AFCs in an Er- and Ti-doped $LiNbO_3$ (Er^{3+}:Ti^{4+}:$LiNbO_3$) waveguide was achieved by taking advantage of population shelving in superhyperfine levels [19]. However, as before, the efficiency did not exceed the percent level, this time due to remaining absorption in the AFC troughs caused by the complexity of the superhyperfine structure and excitation-induced spin relaxation [19]. In addition, the superhyperfine splitting limits the bandwidth for high-efficiency AFCs to around 100 MHz, even assuming magnetic fields of several Tesla. Finally, AFC-based storage of qubits encoded into attenuated laser pulses has been demonstrated using $^{167}Er^{3+}$:Y_2SiO_3. This work relied on spectral hole burning into nuclear spin levels of the ^{167}Er isotope [20], and the use of a nanocavity to reduce the lifetime of the excited level by means of the Purcell effect. However, the small storage bandwidth of 150 MHz, determined by the inhomogeneous linewidth of $^{167}Er^{3+}$:Y_2SiO_3, and the small efficiency of less than 1% supports the general conclusion that the creation of a workable quantum memory for telecommunication-wavelength photons remains an open challenge. An interesting possibility is the use of the same crystal in a magnetic fields of several Tesla [21], but, so far, no storage experiment has been reported.

Here we explore the generation of AFCs in Er^{3+}:Ti^{4+}:$LiNbO_3$ using Zeeman sub-levels for population shelving. First, we quantify the population lifetime of these levels using time-resolved spectral hole burning at a temperature of around 0.7 K and at magnetic fields of up to 1 kG. Next, we create AFCs that persist for up to a few seconds. However, the AFC structures are consistently marred by a significant absorption background, which restricts potential storage efficiencies. Probing the origin of this background, we conjecture, after exclusion of other causes, that it is due to the coupling between laser-induced excitation of two-level systems (TLS) and erbium spins, leading to decay of the ground-state population grating. We conclude that improved crystal growth together with optimized AFC preparation will be required to create an efficient and high-bandwidth quantum memory.

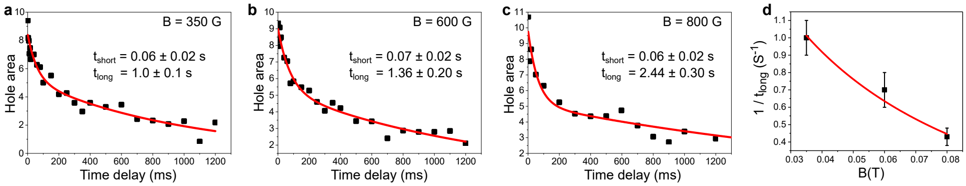

Figure 5.2: Time-resolved spectral hole decays at magnetic fields of **a.** 350 G, **b.** 600 G, and **c.** 800 G. **d.** Long-decay relaxation rate versus magnetic field.

5.2. EXPERIMENTAL DETAILS

Our experiments are performed using the $^4I_{15/2} \leftrightarrow {}^4I_{13/2}$ transition of Er^{+3}:Ti^{4+}:$LiNbO_3$, which is cooled to a temperature of around 0.7 K using an adiabatic demagnetization refrigerator. Details of the waveguide fabrication can be found in Ref. [19]. The waveguide is exposed to magnetic fields up to 5 kG oriented parallel to the c-axis of the crystal. The field lifts the Kramer's degeneracy of the ground and excited electronic levels of erbium, giving rise to Zeeman levels (see Fig. 6.1a for a simplified energy level scheme of Er^{3+}). To interact with the erbium ions, we use light from a continuous-wave laser at around 1532 nm wavelength. As shown in Fig. 6.1c, it is frequency and intensity modulated, and then fibre butt-coupled into and out of the waveguide.

For time-resolved spectral hole burning measurements we first optically-excite erbium ions within a narrow spectral bandwidth, detuned by 250 MHz w.r.t the unmodulated laser light, using pulses of around 300 ms duration. The resulting decay redistributes the ions among the Zeeman sub-levels of the ground state, resulting in a spectral hole. After a varying time delay that exceeds the 2.1 ms population lifetime of the $^4I_{13/2}$ excited level, we measure the decay of the area of the spectral hole (which is proportional to the number of shelved atoms) by linearly varying the frequency of the laser light during 1 ms over a 100 MHz-wide frequency window surrounding the hole. Frequency sweeps are achieved by using a phase modulator and serrodyning, resulting in a modulation efficiency at 1 GHz detuning of approximately 50%.

For AFC generation, we frequency and intensity modulate the excitation light to burn up to 130 spectral pits over a bandwidth of up to 6.4 GHz during 300 ms. Each spectral pit is detuned by 50 MHz from its nearest neighbour to create a periodic modulation in the inhomogeneously broadened atomic absorption spectrum. This frequency spacing of the spectral pits corresponds to an AFC storage time of 20 ns [10]. The absorption profile of the comb is read after a time delay of 30 ms by performing a frequency sweep over bandwidths of up to 6.4 GHz in 1 ms. All measurements are repeated 20 times, and hole and AFC absorption profiles are determined by averaging.

5.3. RESULTS AND DISCUSSION

5.3.1. POPULATION DYNAMICS OF GROUND STATE SUB-LEVELS

Time-resolved spectral hole burning is performed at fields of 350, 600, and 800 G. The time dependent decay of the hole area is plotted in Fig. 5.2, indicating the occupation and the population lifetime of the ground-state Zeeman sub-levels along with those of any other shelving level [17]. We find that the best fit corresponds to a double exponential decay in which the shortest decay exhibits a e^{-1} population lifetime of $t_{\text{short}} \approx 0.06$ s that is independent of the magnetic field, whereas the e^{-1} population lifetimes of the long decays are $t_{\text{long}} = 1.00$, 1.36, and 2.44 s for magnetic fields of 350, 600, and 800 G, respectively. The relative weights of the exponentials do not change with field. Note that we are unable to burn the hole to transparency and we also do not resolve any side-holes or anti-holes, which arise from pumping of atomic population between different, well defined, atomic levels [22].

The short, field independent decay is caused by population trapping in ground levels that couple only weakly to magnetic fields. Previous hole burning measurements [19], in conjunction with the temperatures and fields used here, suggest that these levels are likely superhyperfine levels arising from the coupling of Nb and Li spins of $LiNbO_3$.

The approximately linear field dependence of the population lifetimes of the long decays (t_{long}) suggests that it is governed by spin flips [17]. An increasing magnetic field causes more ions to become spin polarized at low temperatures, which leads to a reduced spin flip-flop probability. Furthermore, the spin inhomogeneous broadening increases with field and reduces the flip-flop rate since it is less likely for two neighboring spins to be resonant [17]. We fit the relaxation rate of the long decays $1/t_{long}$ using a model that describes the temperature (T) and field (B) dependence of spin flip-flops and inhomogeneous broadening [17]:

$$\frac{1}{t_{long}} = \frac{\alpha}{\Gamma_s + \gamma_s B} \operatorname{sech}^2\left(\frac{g\mu_B B}{2kT}\right). \tag{5.1}$$

The magnitude of the spin inhomogeneous broadening is described by a static term Γ_s and a field-dependent term $\gamma_s B$, g is the g-factor, μ_B the Bohr magneton, and α a scaling coefficient.

For a reliable fit of the limited experimental data shown in Fig. 5.2d, we assume $g = 15.13$, which was inferred from measurements of an Er^{3+}:$LiNbO_3$ bulk crystal [23, 24]. Furthermore, fixing the scaling factor of α at 10^9 S^{-2}, as in [17], we find static and field-dependent spin inhomogeneous broadenings of Γ_s=0.4±0.1 GHz and γ_s=14.5±3.0 GHz/T, respectively. The relatively large values are not surprising given the significant spin inhomogeneous broadening of the nuclear Zeeman levels of Tm^{3+} in a Ti^{4+}:$LiNbO_3$ waveguide [25]. These measurements imply significant magnetic disorder in Ti^{4+}:$LiNbO_3$, which is possibly due the inclusion of Ti^{4+}, near surface-related impurities, or the differences of congruent growth compared to other $LiNbO_3$ crystals [25].

5.3.2. CREATION OF AFCS USING ZEEMAN SUB-LEVELS

In order to assess the possibility for broadband quantum memory using Zeeman sub-levels as population reservoir, we generate AFCs with bandwidths between 0.2 and 6.4 GHz symmetrically around zero detuning. All AFCs are centred at 1532.05 nm (corresponding to a spectral region with an optical depth of 2 for light propagating perpendicular to the crystal c-axis), are created under the application of a 3 kG magnetic field (oriented along the crystal c-axis), and feature peak spacings of 50 MHz. Furthermore, the overall duration of the optical pumping cycle is kept constant. Fig. 5.3 shows a 200-MHz section of a 6.4-GHz wide AFC. Note the significant absorption background, which exponentially

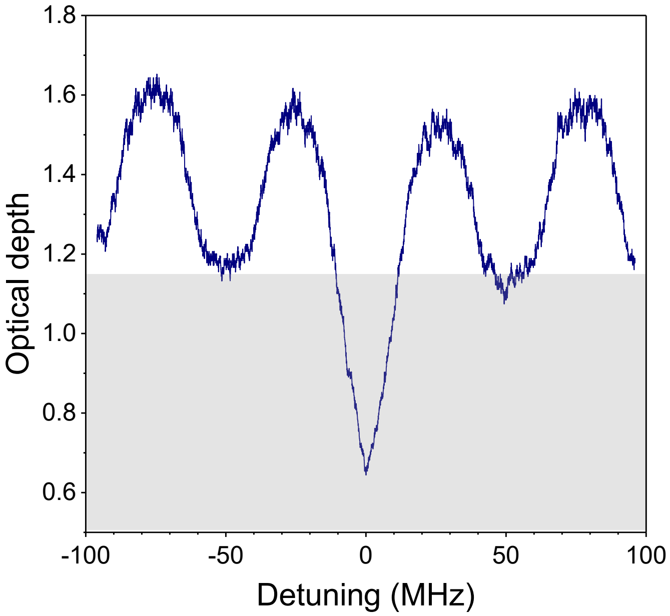

Figure 5.3: Absorption profile of 200 MHz-section of a 6.4 GHz-wide AFC at λ=1532.05 nm and B=3 kG. The grey shaded area indicates remaining background absorption.

reduces the storage efficiency of our AFCs compared to the case of no background [10]. The deep hole at zero detuning is due to optical pumping by unmodulated light leaking through the phase modulator. As shown in Fig. 5.4, we find that the background absorption, which is assessed at detunings between -100 and +100 MHz, increases when the bandwidth of the AFC increases.

5.3.3. DETERMINING THE ORIGIN OF THE BACKGROUND ABSORPTION

ANTI-HOLE BROADENING

One possible explanation for the bandwidth-dependent background absorption is that there is spectral overlap between broad anti-holes (caused by optical pumping) and the AFC. Provided the frequency difference between holes and anti-holes is larger than the anti-hole broadening, the spectral overlap—and hence the background absorption—increases as the AFC bandwidth approaches the hole-to-anti-hole splitting. This is the case in Er:LiNbO$_3$, for which the Zeeman level splitting at 3 kG exceeds 50 GHz and the anti-hole broadening at the same field is expected to be only around 5 GHz. However, the small AFC widths compared with the Zeeman splitting makes spectral overlap between AFCs and antiholes unlikely.

To fully rule out AFC background absorption due to inhomogeneous broadening of ground-state levels (whether arising from Zeeman splitting or not), we generate, at an optical depth of 0.8 (with light propagating parallel to the c-axis of the crystal), pairs of 200 MHz-bandwidth AFCs with varying detuning between their centre frequencies, up to 1.4 GHz. If the broadened anti-holes, created by the second AFC, indeed overlap

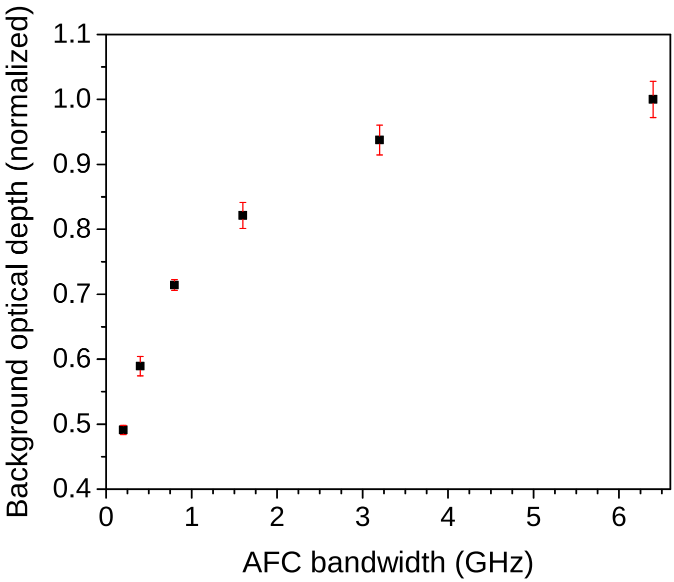

Figure 5.4: Average background absorption as a function of AFC bandwidth.

with the the first AFC, we expect to see an increase in background optical depth of the first AFC. This back-filling method is similar to the one used for characterization of the inhomogeneous broadening of Zeeman sub-levels in an Er-doped fibre [17]. Table. 5.1 quantifies the background absorption of the first AFC at different detunings between the two AFCs. We find that measured values do not increase but rather scatter around a mean of around 0.66. This confirms that the anti-hole broadening does indeed not explain the observed increase of background shown in Fig. 5.4 – at least not for AFC bandwidths up to around 1 GHz. Hence, another mechanism must be responsible, and we conjecture that it will also explain the background for large-bandwidths AFCs.

We note that the inhomogeneous broadening of the superhyperfine levels is too small at the applied magnetic fields to cause a constant absorption background [19], and their contribution to the observation in Fig. 5.4 can thus be ignored.

Table 5.1: **Background absorption for 200 MHz-wide AFCs and varying frequency difference. The case of a single AFC (zero detuning) is included for reference.**

AFC detuning (GHz)	background absorption
0	0.66 ± 0.01
0.6	0.60 ± 0.01
1.0	0.73 ± 0.03
1.4	0.66 ± 0.02

INSTANTANEOUS SPECTRAL DIFFUSION (ISD)

An alternative reason for the increase of background absorption with AFC bandwidth stems from the related increase of excited atoms during AFC preparation. (Even though the average laser power and pump-cycle-duration, i.e. the total energy of the pumping light, remain constant, the number of excited atoms grows due to the non-linear dependence of the absorption rate with the light power spectral density, which decreases with AFC bandwidth.) This may result in two undesired processes: instantaneous spectral diffusion (ISD) [26] (discussed below) and erbium spin flips [15] (discussed in the following sections).

Instantaneous spectral diffusion (ISD) can be introduced by optical pumping, during which Er^{3+} ions are promoted to the excited state, leading to a uncontrollable shift of the transition energies of nearby Er^{3+} ions compared to their unperturbed values. The consequence of addressing the latter ions during subsequent hole burning, is a smeared-out AFC with increased background. Indeed, as the cause for ISD—the presence of excited ions—will disappear at the end of the pumping sequence, transition frequencies will shift back to their unperturbed values, leading to a modification of the previously created absorption profile. ISD increases with the number of excited ions [26], which is consistent with the observed increase of the background absorption with bandwidth.

To characterise broadening and AFC background, which could potentially be due to ISD, we burn two 25 MHz-wide spectral holes with 200 MHz central frequency difference. We vary the laser excitation power used to create one of the holes, which we refer to as the pump hole, while constant power is used to burn the other, which we refer to as the probe hole. The width of the pump hole is expected to increase due to power broadening [2], and ISD would manifest itself by simultaneous broadening and shallowing of the probe hole. We plot the widths and depths of the two holes as a function of optical excitation power used for the pump hole in Fig. 5.5a and b, and find that the width of the probe hole increases by around 5 MHz. Additionally, we observe decrease in the depths of the pump and probe holes with increasing pump power (Fig. 5.5b). Note that due to the optical pumping the reduction of the pump hole depth with increasing pump power is less than that of the probe hole, which decreases by factor of three. The shallowing of the probe and pump holes is consistent with the increase in the background absorption of the AFCs with their bandwidths as shown in Fig. 5.4. However, the level of probe hole broadening of only 5 MHz neither explains the large shallowing of the probe hole nor the increased background optical depth observed in AFCs with 50 MHz tooth spacing (although it will impact the quality of AFCs with small peak spacing, i.e. AFCs that allow for longer storage times).

We also estimate the effect of ISD from measurements of a 0.1%Er^{3+}:$LiNbO_3$ bulk crystal [23]. Assuming a maximum laser excitation power of ~0.5 mW, 0.2% Er^{3+} concentration, and an ISD coefficient of $\sim 2\times10^{-13}$ Hz · cm^3/excited ion, we predict the maximum spectral broadening to be on the order of kHz. This value is three orders of magnitude smaller than the observed increase of the width of the probe hole in Fig. 5.5a. Hence, our experimental results and our estimate suggest that ISD is neither the cause for the observed spectral broadening of the probe hole, nor for the remaining background absorption of the probe hole and the AFCs. In the next sections we elaborate on two other power-dependent mechanisms that may cause these observations.

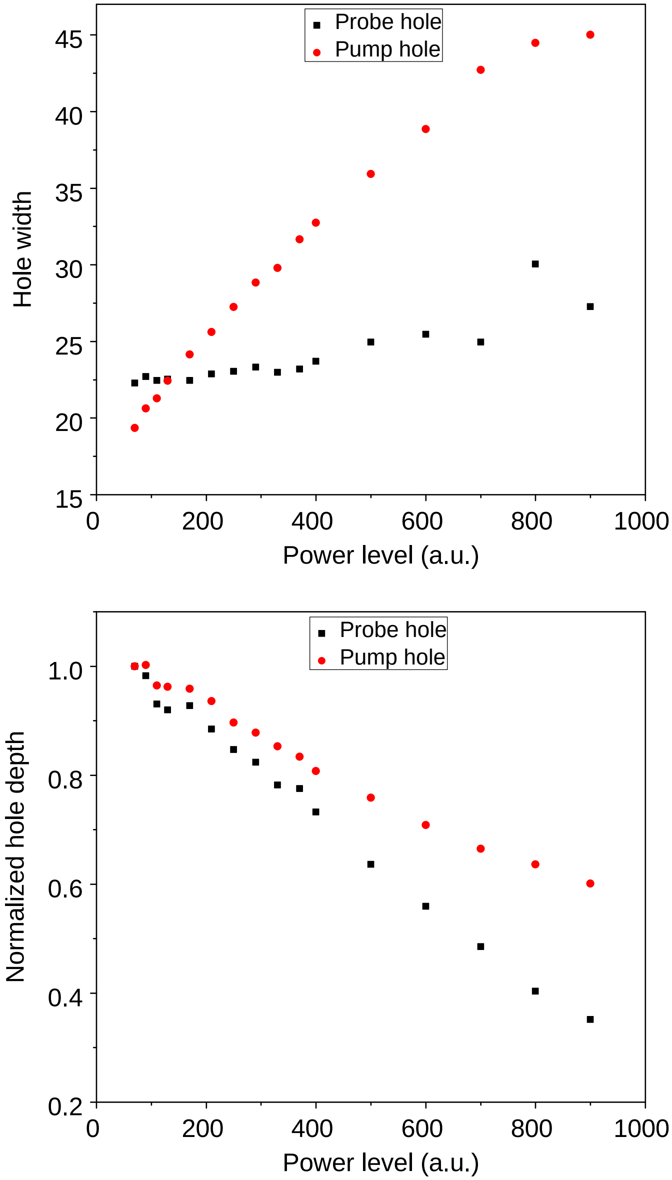

Figure 5.5: Laser excitation-induced change of a spectral hole. **a.** Widths and **b.** depths of the pump and probe holes (see text for details).

SPIN FLIP-FLOPS

Another process that could be affected by the increase of Er^{3+} excitation when creating AFCs of larger bandwidths is the number of spin flip-flops. In this case, spins in one ground-state sub-level (Zeeman shelving level) that are within the AFC bandwidth resonantly exchange state with other spins that are in the other ground-state sub-level and outside of the AFC bandwidth: one spin will be flipped up, the other flopped down. This leads to redistribution of the population within the AFC, and hence to background. However, as the spin flip-flop rate decreases with the sixth power of the distance between ER-ions, we estimate its contribution to be small. In fact, if we extrapolate results from [27] to an approximate Er-doping concentration of 3.6×10^{19} cm^{-3} (or 0.2%), we find a flip-flop rate of a few Hz – by far to little to explain the AFC background.

TLS-DRIVEN SPIN-FLIPS

Another power-dependent mechanism that may be responsible for the increase of the width of the probe hole and the AFC background is light-induced two-level system (TLS) excitation, which, in turn, may drive spin flips. In this case, the laser field first excites TLSs in $LiNbO_3$ [28]. The TLSs may subsequently decay into lower-energy states and emit phonons, which interact with the electronic spins of Er^{3+}, leading to spectral diffusion that can explain the observations in Fig. 5.4. We note that a similar effect was observed in Tm^{3+}-doped Ti^{4+}:$LiNbO_3$ [25].

In support of this hypothesis, we note that congruent $LiNbO_3$ is known to contain various impurities and imperfections, and previous measurements of REI-doped $LiNbO_3$ suggest significant lattice disorder. Such disorder could be the origin of the above-described TLSs [24, 25, 29, 30]. We also point out that laser-induced excitation and decay of TLS impurities determines photo-refraction in $LiNbO_3$. It is well-known that this effect is enhanced in waveguides compared to bulk crystals due to high confinement of the laser field and, consequently, larger light intensities. This is consistent with the fact that the emergence of an absorption background in AFCs due to spectral hole filling is not observed in bulk $LiNbO_3$.

5.3.4. DISCUSSION AND CONCLUSION

We experimentally study ground-state Zeeman sub-levels of Er^{3+} ions doped into a Ti^{4+}:$LiNbO_3$ crystalline waveguide as shelving levels for AFC-type quantum memory for light. Despite promising lifetimes in excess of a second, several changes are required to increase the storage efficiency for telecommunication-wavelength photons beyond the current state-of-the-art of around 1%. Most importantly, the memory efficiency, which is limited by the available optical depth (at most 2 in our waveguide) and the absorption background need to be improved. The former can be addressed using an impedance-matched cavity [31], and the absorption background may be reduced through optimization of the optical pumping procedure. This includes the use of optimized optical excitation power, laser scan rate, and magnetic field strength and direction, which may result in longer-lived Zeeman levels and a favourable branching ratio into the shelving level. But ultimately, it seems necessary to improve the $LiNbO_3$ crystal itself, e.g. by varying growth conditions, to reduce the number of two-level systems.

5.4. ACKNOWLEDGMENTS

The authors thank Wolfgang Sohler, Mathew George, and Raimund Ricken for providing the waveguide, and Jakob H. Davidson for help with aligning the waveguide and Gustavo Amaral and Erhan Saglamyurek for useful discussions. The authors also acknowledge support from Alberta Innovates (AI), the Alberta Major Innovation Fund, the Natural Sciences and Engineering and Research Council of Canada (NSERC), and the Dutch Organisation for Scientific Research (NWO). N.S. acknowledges funding from the AQT's Intelligent Quantum Networks and Technologies (INQNET) research program, and W.T. support as a Senior Fellow of the Canadian Institute for Advanced Research (CIFAR).

REFERENCES

[1] W. Tittel, M. Afzelius, T. Chaneliere, R. L. Cone, S. Kröll, S. A. Moiseev, and M. Sellars, *Photon-echo quantum memory in solid state systems,* Laser & Photonics Reviews **4**, 244 (2010).

[2] G. Liu and B. Jacquier, *Spectroscopic properties of rare earths in optical materials*, Vol. 83 (Springer Science & Business Media, 2006).

[3] A. I. Lvovsky, B. C. Sanders, and W. Tittel, *Optical quantum memory,* Nature Photonics **3**, 706 (2009).

[4] M. Gündoğan, P. M. Ledingham, K. Kutluer, M. Mazzera, and H. De Riedmatten, *Solid state spin-wave quantum memory for time-bin qubits,* Physical review letters **114**, 230501 (2015).

[5] N. Sinclair, E. Saglamyurek, H. Mallahzadeh, J. A. Slater, M. George, R. Ricken, M. P. Hedges, D. Oblak, C. Simon, W. Sohler, *et al.*, *Spectral multiplexing for scalable quantum photonics using an atomic frequency comb quantum memory and feed-forward control,* Physical review letters **113**, 053603 (2014).

[6] M. Sabooni, S. T. Kometa, A. Thuresson, S. Kröll, and L. Rippe, *Cavity-enhanced storage—preparing for high-efficiency quantum memories,* New Journal of Physics **15**, 035025 (2013).

[7] C. Clausen, I. Usmani, F. Bussières, N. Sangouard, M. Afzelius, H. de Riedmatten, and N. Gisin, *Quantum storage of photonic entanglement in a crystal,* Nature **469**, 508 (2011).

[8] E. Saglamyurek, N. Sinclair, J. Jin, J. A. Slater, D. Oblak, F. Bussieres, M. George, R. Ricken, W. Sohler, and W. Tittel, *Broadband waveguide quantum memory for entangled photons,* Nature **469**, 512 (2011).

[9] M. Afzelius, I. Usmani, A. Amari, B. Lauritzen, A. Walther, C. Simon, N. Sangouard, J. Minář, H. De Riedmatten, N. Gisin, *et al.*, *Demonstration of atomic frequency comb memory for light with spin-wave storage,* Physical review letters **104**, 040503 (2010).

[10] M. Afzelius, C. Simon, H. De Riedmatten, and N. Gisin, *Multimode quantum memory based on atomic frequency combs,* Physical Review A **79**, 052329 (2009).

[11] B. Lauritzen, S. Hastings-Simon, H. De Riedmatten, M. Afzelius, and N. Gisin, *State preparation by optical pumping in erbium-doped solids using stimulated emission and spin mixing,* Physical Review A **78**, 043402 (2008).

[12] T. Böttger, C. Thiel, R. Cone, and Y. Sun, *Effects of magnetic field orientation on optical decoherence in* $Er^{3+}:Y_2SiO_5$, Physical Review B **79**, 115104 (2009).

[13] B. Lauritzen, J. Minář, H. De Riedmatten, M. Afzelius, N. Sangouard, C. Simon, and N. Gisin, *Telecommunication-wavelength solid-state memory at the single photon level,* Physical review letters **104**, 080502 (2010).

[14] S. Hastings-Simon, B. Lauritzen, M. U. Staudt, J. L. M. van Mechelen, C. Simon, H. de Riedmatten, M. Afzelius, and N. Gisin, *Zeeman-level lifetimes in* $Er^{3+}:Y_2SiO_5$, Physical Review B **78**, 085410 (2008).

[15] T. Böttger, C. Thiel, Y. Sun, and R. Cone, *Optical decoherence and spectral diffusion at 1.5 µm in* $Er^{3+}:Y_2SiO_5$ *versus magnetic field, temperature, and* Er^{3+} *concentration,* Physical Review B **73**, 075101 (2006).

[16] E. Saglamyurek, J. Jin, V. B. Verma, M. D. Shaw, F. Marsili, S. W. Nam, D. Oblak, and W. Tittel, *Quantum storage of entangled telecom-wavelength photons in an erbium-doped optical fibre,* Nature Photonics **9**, 83 (2015).

[17] E. Saglamyurek, T. Lutz, L. Veissier, M. P. Hedges, C. W. Thiel, R. L. Cone, and W. Tittel, *Efficient and long-lived zeeman-sublevel atomic population storage in an erbium-doped glass fiber,* Physics Review B **92**, 241111 (2015).

[18] L. Veissier, M. Falamarzi, T. Lutz, E. Saglamyurek, C. W. Thiel, R. L. Cone, and W. Tittel, *Optical decoherence and spectral diffusion in an erbium-doped silica glass fiber featuring long-lived spin sublevels,* Physics Review B **94**, 195138 (2016).

[19] M. F. Askarani, M. G. Puigibert, T. Lutz, V. B. Verma, M. D. Shaw, S. W. Nam, N. Sinclair, D. Oblak, and W. Tittel, *Storage and reemission of heralded telecommunication-wavelength photons using a crystal waveguide,* Physical Review Applied **11**, 054056 (2019).

[20] I. Craiciu, M. Lei, J. Rochman, J. M. Kindem, J. G. Bartholomew, E. Miyazono, T. Zhong, N. Sinclair, and A. Faraon, *Nanophotonic quantum storage at telecommunications wavelength,* Physical Review Applied **12**, 024062 (2019).

[21] M. Rančić, M. P. Hedges, R. L. Ahlefeldt, and M. J. Sellars, *Coherence time of over a second in a telecom-compatible quantum memory storage material,* Nature Physics **14**, 50 (2018).

[22] S. Hastings-Simon, M. Afzelius, J. Minář, M. Staudt, B. Lauritzen, H. de Riedmatten, N. Gisin, A. Amari, A. Walther, S. Kröll, *et al., Spectral hole-burning spectroscopy in* $Nd^{3+}:YVO_4$, Physical Review B **77**, 125111 (2008).

[23] C. W. Thiel, R. M. Macfarlane, R. L. Cone, Y. Sun, T. Bottger, K. D. Merkel, and B. W. R, *Spectroscopy and dynamics of Er*$^{3+}$*:LiNbO*$_3$ *at 1.5 microns for quantum information and signal processing applications,* 10th Intl Meeting on Hole Burning, Single Molecule, and Related Spectroscopies: Science and Applications - HBSM (2009).

[24] C. Thiel, R. Macfarlane, T. Böttger, Y. Sun, R. Cone, and W. Babbitt, *Optical decoherence and persistent spectral hole burning in Er*$^{3+}$*: LiNbO*$_3$*,* Journal of Luminescence **130**, 1603 (2010).

[25] N. Sinclair, C. W. Thiel, D. Oblak, E. Saglamyurek, R. L. Cone, and W. Tittel, *Properties of a Tm-doped LiNbO*$_3$ *waveguide at low temperatures,* In preparation (2018).

[26] C. W. Thiel, R. M. Macfarlane, Y. Sun, T. Böttger, N. Sinclair, W. Tittel, and R. L. Cone, *Measuring and analyzing excitation-induced decoherence in rare-earth-doped optical materials,* Laser Physics **24**, 106002 (2014).

[27] E. S. Petersen, A. M. Tyryshkin, K. M. Itoh, H. Riemann, N. V. Abrosimov, P. Becker, H.-J. Pohl, M. L. Thewalt, and S. A. Lyon, *Measuring electron spin flip-flops through nuclear spin echo decays,* arXiv preprint arXiv:1709.02881 (2017).

[28] R. Jankowiak and G. Small, *Hole-burning spectroscopy and relaxation dynamics of amorphous solids at low temperatures,* Science **237**, 618 (1987).

[29] Y. Sun, C. Thiel, and R. Cone, *Optical decoherence and energy level structure of 0.1% Tm*$^{+3}$*: LiNbO*$_3$*,* Physical Review B **85**, 165106 (2012).

[30] L. Arizmendi, *Photonic applications of lithium niobate crystals,* physica status solidi (a) **201**, 253 (2004).

[31] M. Afzelius and C. Simon, *Impedance-matched cavity quantum memory,* Physical Review A **82**, 022310 (2010).

6

STORAGE AND REEMISSION OF HERALDED TELECOMMUNICATION-WAVELENGTH SINGLE PHOTONS USING A CRYSTAL WAVEGUIDE

Mohsen Falamarzi Askarani, Marcel.li Grimau Puigibert, Thomas Lutz, Varun B. Verma, Matthew D. Shaw, Sae Woo Nam, Neil Sinclair, Daniel Oblak, Wolfgang Tittel

Large-scale fibre-based quantum networks will likely employ telecommunication-wavelength photons of around 1550 nm wavelength to exchange quantum information between remote nodes, and quantum memories, ideally operating at the same wavelength, that allow increasing the transmission distances as a key element of a quantum repeater. However, the development of a suitable memory remains an open challenge. Here, we demonstrate the storage and reemission of single, heralded, 1532 nm-wavelength photons using a crystal waveguide. The photons are emitted from a photon-pair source based on spontaneous parametric down-conversion, and the memory is based on an atomic frequency comb of 6 GHz bandwidth, prepared through persistent spectral hole burning of the inhomogeneously broadened absorption line of a cryogenically-cooled erbium-doped lithium niobate waveguide. Despite currently limited storage time and efficiency, this demonstration represents an important step towards quantum networks that operate in the telecommunication band, and the development of integrated (on-chip) quantum technology using industry-standard crystals.

This chapter has been published in Phys. Rev. Applied 11, 054056 (2019).

6.1. INTRODUCTION

Many efforts towards future quantum networks [1] have focused on employing telecommunication-wavelength photons in the C-band (1530-1565 nm) due to their suitability for connecting remote nodes via existing and low-loss fibre infrastructure. The synchronization of information in such nodes is enabled by quantum memories that allow storing and later retrieving quantum information [2]. As such, quantum memories are essential for the operation of quantum repeaters, which promise the transmission of quantum information over large distances [3].

The push to realize long-distance quantum communication has been enabled by significant progress in developing quantum-optical technology [4]. However, a lot of this work is not compatible with C-band photons without the use of complexity-adding and potentially-lossy frequency conversion [5]. To avoid this conversion step, supplementary efforts have focused on developing quantum technology that operates in the telecom C-band, which has resulted in the development of efficient single-photon detectors [6] and single-photon sources [7], for example. Furthermore, significant progress towards quantum memories using various platforms has been made in the last decade [8]. One promising approach is based on cryogenically-cooled rare-earth-ion-doped crystals as they often feature suitable properties such as long optical and spin coherence times [9]. Achievements include storage of entangled photons [10, 11], teleportation into a quantum memory [12], storage in nano-fabricated structures[13], and storage assisted by impedance-matched cavities [14, 15]. In addition, quantum storage and signal processing has been demonstrated using thulium doped into an industry-standard titanium-indiffused lithium niobate waveguide [10] – a promising approach to efficient on-chip information processing. However, developing a C-band quantum memory, especially one that can be integrated on-chip, has turned out to be a challenging task.

One class of materials that has the potential to fill this gap is that of erbium-doped crystals. They are unique in that they offer a ground-to-excited level transition at around 1532 nm wavelength and optical coherence times up to 4.4 ms – the longest in any optical transition in a solid [16]. This has prompted the demonstration of a photon-echo quantum memory protocol with attenuated laser pulses at the single-photon level in Er:Y_2SiO_5 [17], but not for non-classical (single photon) light. The difficulty with erbium-doped materials is the relatively long lifetime of the excited level—up to ~11 ms—compared to that of sub-levels within the ground-state manifold (around 100 ms). This makes optical pumping to the latter—a necessary step in photon-echo quantum memory [2]—challenging and poses a significant obstacle to achieving high storage efficiency. This problem is partially solved in Er-doped fibres, which, due to their amorphous (rather than crystalline) structure, feature reduced spin-spin interactions and, as a result, extended ground-state (Zeeman-level) lifetimes [18]. This has allowed recent demonstrations of storage and reemission of non-classical and entangled states of light at telecommunication wavelengths [19]. However, despite the appeal of Er-doped fibres for all-fibre implementations, decoherence arising from their amorphous structure [20] currently restricts the storage time to about 50 nanoseconds, though improvements at ultra-low temperatures may be possible.

Other promising approaches to overcoming the limitations of erbium are the use of magnetic fields of several Tesla, where ground state lifetimes can exceed one minute [21], and crystals inside cavities with high quality factors and small mode volumes, which reduce the excited state lifetime by means of the Purcell effect [22]. But despite a lot of research aimed at developing quantum memory at telecommunication wavelength, the storage and reemission of non-classical light using an erbium-doped crystal, in particular a crystalline waveguide that can be integrated with telecommunication-industry devices, remains a yet-to-be-achieved goal.

Here we demonstrate quantum memory for heralded single photons at 1532.05 nm wavelength using an Er-doped lithium niobate waveguide created through titanium indiffusion. The heralded photons are generated using a photon-pair source based on spontaneous parametric down-conversion (SPDC), and storage and reemission relies on the atomic frequency comb (AFC) protocol [23] and optical pumping into superhyperfine levels, which have previously not been exploited towards this end. The nonclassical nature of the re-emitted (heralded) photons is verified by measuring the cross-correlation function $g_{12}^{(2)}$ with the heralding photons.

6.2. THE AFC QUANTUM MEMORY PROTOCOL

The storage and reemission process of single photons is based on the AFC protocol, which has underpinned a lot of progress towards efficient and broadband quantum memory during the past decade. For example, storage times as long as milliseconds [24], efficiencies as high as 56% [14], storage bandwidths of several GHz [10] and fidelities up to 99.9% [25] have been achieved.

An atomic frequency comb is comprised of a series of narrow spectral absorption lines that are equidistantly detuned by Δ (a 'comb' of absorption features) [23]. It can be prepared from an inhomogeneously broadened absorption line of rare-earth ions by frequency-selective optical pumping of population into long-lived auxiliary levels. The absorption of a photon by an AFC leads to a collective atomic excitation described by

$$|\Psi\rangle_A = \frac{1}{\sqrt{N}} \sum_{j=1}^{N} c_j e^{-i2\pi\delta_j t} e^{ikz_j} \left|g_1, ...e_j, ...g_N\right\rangle . \tag{6.1}$$

Here N is the number of ions and δ_j the detuning of the jth ion's transition frequency with respect to the carrier frequency of the incoming photon. The longitudinal position of the ions is denoted by z_j, and the coefficient c_j is related to the ion's excitation probability (i.e. it's position and transition frequency). After absorption, each term in Eq. (6.1) accumulates a phase that depend on the detuning $\delta_j = m_j\Delta$, where m_j is an integer. Consequently, all terms coherently rephase at a time $\tau = 1/\Delta$, leading to collective reemission of the photon in its original quantum state. Under certain conditions the reemission process can reach unit efficiency [23, 26, 27].

6.3. SPECTROSCOPIC CHARACTERIZATION

For AFC-based quantum state storage in an ensemble of absorbers, in our case rare-earth ions doped into a crystal, the storage medium has to meet several criteria. In addition to suitable level structure (e.g. absorption at the desired wavelength), they include

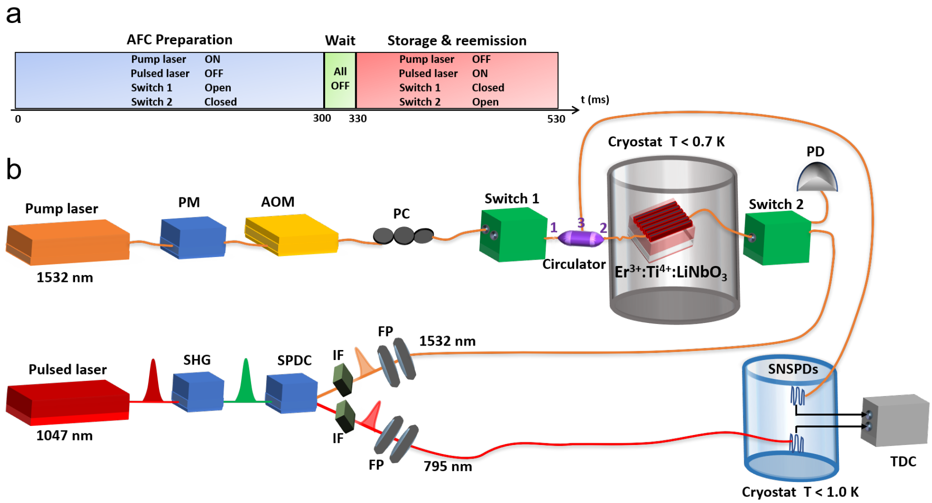

Figure 6.1: a) Experimental timing sequence. The sequence is continuously repeated during the experimental run. Switch 2 is closed (and connected to the photodetector, PD) during the AFC preparation for monitoring the AFC structure and for recording the frequency-depending optical depth shown in Figs. 6.2a and 6.3b. The experimental set-up consists of two main parts. The part depicted in the top half allows for optical pumping (spectral hole burning) and AFC generation – it consists of a pump laser, a phase modulator (PM), an acousto-optic modulator (AOM), a polarization controller (PC), optical switches, a circulator, and a photodetector (PD). The part in the bottom half depicts the heralded single photon generation and the detection setup – it consists of a pulsed pump laser, second harmonic generation (SHG), spontaneous parametric down conversion (SPDC), longpass filters (LF), Fabry-Perot cavities (FP), superconducting nanowire single-photon detectors (SNSPD), and a time-to-digital converter (TDC). See Appendix C to E for details of all components.

an inhomogeneously broadened absorption profile with a bandwidth that exceeds the inverse duration of the photons to be stored; the possibility for optical pumping into long-lived auxiliary shelving levels (so-called persistent spectral hole burning); and a coherence time in excess of the desired storage time.

To date, only a few spectroscopic studies of the low-temperature properties of the 1532 nm $^4I_{15/2} \leftrightarrow {}^4I_{13/2}$ transition of erbium-doped lithium niobate—both in bulk crystals as well as waveguides created by means of titanium indiffusion (see Appendix A for details about the waveguide fabrication)—have been reported [9, 28–31]. For light polarized orthogonal to the crystal's c-axis ($\mathbf{E}\perp\mathbf{c}$), the 1532 nm transition of Er:LiNbO$_3$ features a 180 GHz-wide inhomogeneously-broadened line, a 2 ms population lifetime of the $^4I_{13/2}$ level, and, at a temperature of 1.6 K and a magnetic field of 50 kG oriented parallel to the c-axis ($\mathbf{B}\|\mathbf{c}$), an optical coherence time of 117 μs [9, 30]. The same transition of Er^{3+} was studied in a Ti^{4+}:LiNbO$_3$ waveguide at 3 K, resulting in a 250 GHz-wide inhomogeneously broadened line, a population lifetime matching that of the bulk material, and a coherence lifetime of 18.2 μs in a 4 kG field oriented $\mathbf{B}\|\mathbf{c}$ [28]. We expect that the coherence lifetime of the waveguide increases and eventually equals that of the bulk crystal at lower temperatures and under the application of an optimized magnetic field, similarly to what we previously observed for a Tm^{3+}:Ti^{4+}:LiNbO$_3$ waveguide compared

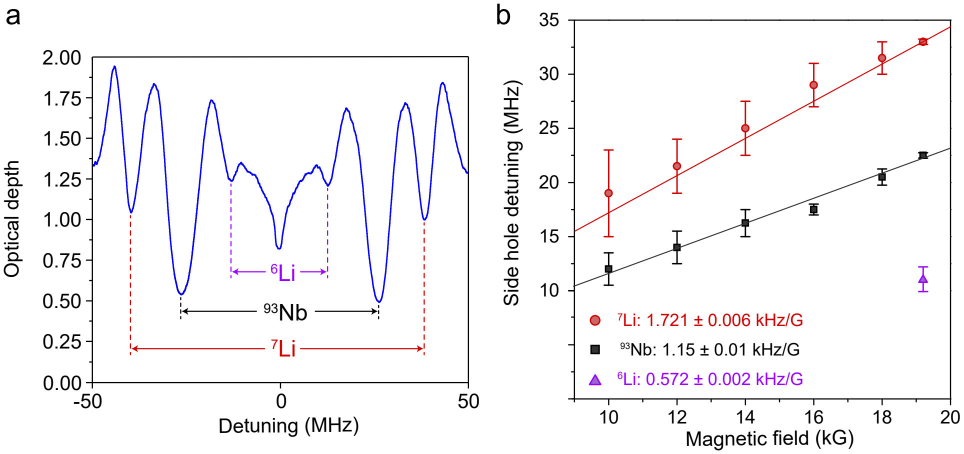

Figure 6.2: a) Optical depth over a 100 MHz-wide spectral range centered at 1532.05 nm after applying a 19 kG magnetic field. Side holes due to the interaction between the Er^{3+} electronic spin and ^{93}Nb, ^{6}Li, and ^{7}Li nuclear spins are visible. The apparent side-holes at ±50 MHz are due to an imperfect frequency sweep. b) Detuning of ^{7}Li and ^{93}Nb side holes as a function of the magnetic field. Side holes for ^{6}Li are resolved only at the highest field. Uncertainty bars indicate the difference between the detunings of the positive and negative side hole compared to the central hole.

to bulk Tm^{3+}:$LiNbO_3$ [32].

To identify long-lived auxiliary levels with lifetimes that significantly exceed that of the $^4I_{13/2}$ excited level, we perform spectral hole burning (SHB) to study the level structure and dynamics of Er^{3+}:Ti^{4+}:$LiNbO_3$ at various magnetic fields. Towards this end we excite the inhomogeneously broadened 1532 nm transition using a narrowband laser, and then read the frequency-dependent absorption profile by scanning the laser over a spectral interval centered at the excitation frequency. An absorption spectrum obtained at a magnetic field of 19 kG and taken after 30 s—a time that exceeds by far the lifetime of the $^4I_{13/2}$ level—is shown in Fig. 6.2a. Regions of increased (decreased) transparency that are detuned from the central hole (at the excitation frequency) are referred to as side- (anti-) holes – additional studies with varying waiting times between excitation and read-out reveal that they persist for several minutes.

To determine the cause of the level splitting and hence the sub-structure, we perform SHB at different magnetic fields with $\mathbf{B}\|\mathbf{c}$. Fig. 6.2b depicts the field-dependent detunings for three pairs of distinguishable side-holes. Fits yield values of 1.15±0.01, 1.721±0.006, and 0.572±0.002 kHz/G, respectively. This agrees with the superhyperfine coupling between the Er^{3+} electronic spin ($S = 1/2$) and the nuclear spins of ^{93}Nb ($I = 9/2$), ^{7}Li ($I = 3/2$), and ^{6}Li ($I = 1$) in the host crystal that was previously reported for an Er^{3+}:$LiNbO_3$ bulk crystal [30]. The side-hole positions are determined by the excited-level splitting, whereas the position of the anti-holes are given by the ground state splitting as well as by differences between ground and excited state splittings. These observations suggest the possibility for persistent spectral hole burning using, for the first time, superhyperfine levels.

In addition, we also found evidence of population transfer into long-lived electronic

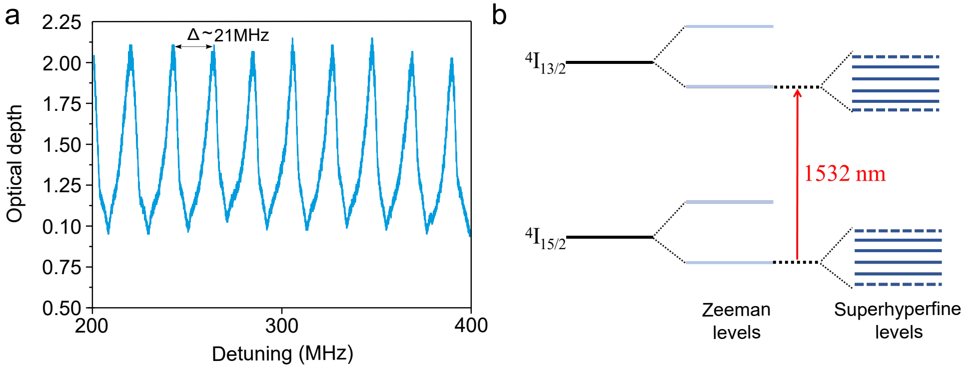

Figure 6.3: a) A 200 MHz wide section of our 6 GHz-bandwidth AFC. b) Simplified energy level diagram of erbium in lithium niobate. An AFC can be created by redistributing—optically pumping through the $^4I_{13/2}$ excited level—ions between superhyperfine levels of the $^4I_{15/2}$ ground state manifold.

Zeeman levels of erbium at small magnetic fields. However, a large absorption background in AFCs exceeding 1 GHz bandwidth prevented us from using these levels for shelving. For more information see [33].

6.4. HERALDED SINGLE PHOTON STORAGE

To demonstrate storage of single photons in the Er-doped crystal, we apply a magnetic field of 16.5 kG and $\mathbf{B}\|\mathbf{c}$ across the crystal, and create an AFC with approximately 21 MHz tooth spacing, i.e. a storage time of $\tau = 48$ ns. The tooth spacing was chosen such that the comb periodicity coincides with the excited-level splitting caused by the superhyperfine interactions between the erbium electronic spin and the nuclear spin of ^{7}Li and ^{93}Nb. The finesse of the comb – the ratio of tooth width γ to tooth spacing Δ – is two. Combined with the optical depths of the comb and the background obtained from the AFC trace in Fig. 6.3, it limits the AFC storage efficiency to around 1%. However, insufficient laser intensity at large detunings and hence non-optimized hole burning leads to a non-uniform AFC and an averaged AFC efficiency of around 0.1%.

Next, we generate 6 GHz wide heralded single photons at 1532 nm wavelength using spontaneous parametric down conversion (SPDC) of short, 523 nm laser pulses in a periodically-poled lithium-niobate crystal. This non-linear process results in the probabilistic generation of photon pairs at 795 nm and 1532 nm wavelength, and detecting a 795 nm photon hence indicates (heralds) the presence of another photon at 1532 nm. (The experimental setup is outlined in Fig. 6.1 and its components are described in detail in Appendix C.) These photons are then sent into, absorbed (stored) in, and re-emitted from the erbium memory after the pre-programmed time delay of 48 ns, see Fig. 6.4.

To demonstrate the non-classical nature of the re-emitted photons, and hence the memory, we measure the second-order cross-correlation function $g_{12}^{(2)} = \frac{P_{12}}{P_1 P_2}$. Here, the probability of detecting a coincidence between the two photons is P_{12}, and P_1 (P_2) are the probabilities of detecting the two photons individually (see Ref. [34] for more de-

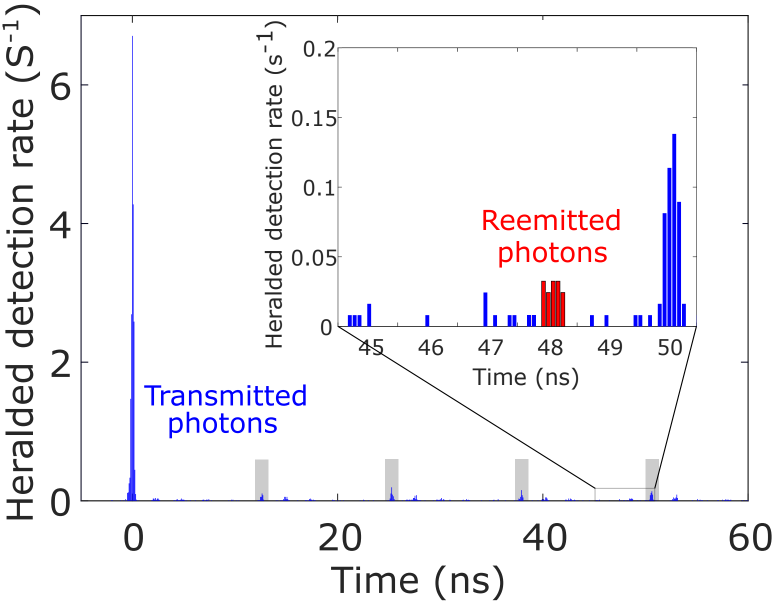

Figure 6.4: Storage and reemission of heralded single photons at telecommunication wavelength. The histogram depicts the time-resolved rate of coincidence detections of heralding 795 nm and heralded 1532 nm photons. The overall acquisition time is 2 min. The time axis is defined relative to the detection of 1532 nm photons that are directly transmitted (not absorbed) by the memory. Stored photons are re-emitted after 48 ns and cause the coincidence peak highlighted in red in the zoom in. The number of coincidences in the 500 ps-long window is 18±4.24, clearly exceeding the background of 1.9±0.45 per 500 ps window, obtained by averaging coincidences between 44.5 ns and 49.5 ns. The coincidence peaks at $t \approx 2.5, 5, 7.5, 10$ ns are due to spurious temporal modes of the pump laser – a consequence of imperfect alignment of the laser cavity – causing additional photon-pair generation by the SPDC crystal. The sequence of coincidence detection peaks is repeated every 12.5 ns, matching the 80 MHz repetition rate of the pulsed SPDC pump laser. These repeated patterns, often referred-to as accidental coincidences, are due to the detection of photons belonging to pairs that have been generated during different laser cycles.

tails). To verify the presence of non-classical correlations, $g_{12}^{(2)}$ must be greater than 2 [34, 35]. First, bypassing the waveguide, we determine $g_{12}^{(2)}$ of our photon pair source (without additional storage) to be around 20. It is limited by multi-pair emissions that are caused by the high pump intensity [35]. Repeating the measurement with re-emitted photons, we then find $g_{12}^{(2)}$=7.1±4 (see Appendix E for details). This demonstrates that non-classical correlations between the members of photon pairs remain throughout the storage process, i.e. that the memory indeed operates in the quantum domain.

6.5. DISCUSSION

While this result is promising, several improvements are necessary to create a quantum memory that can be used in a quantum repeater. First, the total system efficiency—evaluated by comparing the heralded photon detection rates measured with the full setup with that after circumventing the cryostat (including the memory)—is currently only of around 0.01%. This number is limited by a coupling efficiency of around 10% and, as mentioned above, the efficiency of the storage and reemission process (i.e. that of the AFC itself) of 0.1%. The latter is determined by several factors, including the lack of phase-matching that allows triggering backwards emission [23], low finesse (F=2) of the AFC due to the chosen pumping scheme, insufficient optical depth of the comb teeth, and a remaining absorption background, especially at large detuning.

The coupling efficiency can be improved by optimized matching of the modes guided by the fibre and the waveguide. Furthermore, the limited optical depth and the lack of phase matching can be countered with an impedance-matched cavity [26, 27]. However, this solution is not beneficial without reducing the remaining background loss, which we attribute to the complexity of the superhyperfine level structure and the possibility of laser-induced enhancement of spin relaxation [31, 33] – an effect that we have previously observed, and mitigated, in the creation of AFCs in Tm^{3+}:Ti^{4+}:$LiNbO_3$ [32].

We believe that further characterization of the atomic level structure and population dynamics, in particular through more detailed SHB measurements (e.g. with varying magnetic field strength and orientation), as well as optimization of the AFC preparation steps (e.g. using back-pumping [36] or spin-mixing methods [37]), will allow a significant reduction of the background absorption. Another possibility may be exploring persistent spectral hole burning into Zeeman levels [33]. Furthermore, wavelength-dependent measurements may allow the identification of ions belonging to different magnetic subclasses and featuring favorable (superhyperfine- or Zeeman-) levels. Ultimately, a lower sample temperature and erbium doping concentration could allow for more efficient SHB in addition to suppressing decoherence caused, e.g., by spin flip-flops.

Another limitation of the current demonstration is the storage time, which, as described above, is indirectly determined by the strength of the external magnetic field. More precisely, the field sets the splittimg of the superhyperfine levels, which in turn determines the frequency spacing between peaks and troughs of the AFC and hence the comb periodicity Δ. If this were the only factor, then using small magnetic fields would allow for arbitrarily small teeth spacing and hence arbitrarily long storage times. However, the minimum teeth spacing (and hence the maximum storage time) is given by the material's homogeneous linewidth (the inverse of the coherence time, possibly rendered worse by spectral diffusion), and – being the limiting factor in our case – instability of the frequency of the (free running) laser used for spectral hole burning. We estimate that locking to a stable reference cavity would allow increasing the storage time to a few μs, which could be further increased to hundreds of μsec by further reducing the temperature.

Finally, we note that our current approach does not allow photons to be re-emitted on-demand, which requires an additional step, i.e. the reversible, coherent, mapping to a third long-lived level [38]. Nonetheless, applications such as quantum repeaters may utilize memories of fixed storage times provided that spectral or spatial multiplexing is performed [39].

6.6. CONCLUSION

In conclusion, we have demonstrated the storage and reemission of heralded single photons at telecommunication-wavelength using a cryogenically-cooled erbium-doped lithium niobate waveguide. The non-classical nature of the storage process is demonstrated by a measurement of the cross-correlation coefficient between the heralding and the heralded photons after reemission. We employed an AFC that is based on optical pumping of atomic population into superhyperfine ground levels, and we have detailed the limitations as well as possible improvements of our memory, in particular its limited storage efficiency. Our work is a step towards on-chip quantum network technology operating in the important telecommunication C-band using standard telecommunication industry materials.

6.7. APPENDICES

6.7.1. APPENDIX A: ER-DOPED LITHIUM NIOBATE WAVEGUIDE

To fabricate the Er^{3+}:Ti^{4+}:$LiNbO_3$ waveguide, z-cut congruent $LiNbO_3$ is Er-doped over a length of 10 mm by indiffusion of a vacuum-deposited (electron-beam evaporated) 8 nm-thick Er layer at 1130 °C for 150 h in an Ar-atmosphere. This step is followed by a post-treatment in Oxygen (1 h) to get a full re-oxidization of the crystal. Er substitutes for Li when incorporated into the $LiNbO_3$ lattice. The indiffusion results in a 3.6×10^{19} cm^{-3} near-surface concentration and a Gaussian concentration profile that features a 1/e penetration depth of 8.2 μm [40]. Next, the waveguide is created by indiffusion of Ti. To do this, a 98 nm-thick titanium layer is deposited on the Er-doped surface of the $LiNbO_3$ substrate using electron beam evaporation. From this layer, 7 μm-wide Ti strips are defined by photo-lithography and chemical etching, and subsequently in-diffused at 1060 °C for 8.55 h. This process leads to a single-mode waveguide with a 4.5×3 μm full-width-at-half-maximum intensity distribution for transverse magnetic-polarization. Note that an analogous procedure, which is detailed in Ref. [10], was used to fabricate the similar Tm^{3+}:Ti^{4+}:$LiNbO_3$ waveguide.

For our experiments, the Er^{3+}:Ti^{4+}:$LiNbO_3$ waveguide is mounted in an adiabatic demagnetization refrigerator that can be operated at temperatures of around 0.6 K (Fig. 6.1). A magnetic field oriented $\mathbf{B}\|\mathbf{c}$ of up to 20 kG is applied using a solenoid. Light is coupled into, and out of, the waveguide by fibre butt-coupling. The overall in-out coupling transmission of our cryogenic setup is around 10% (measured at a wavelength of 1532.05 nm).

6.7.2. APPENDIX B: SHB AND AFC PREPARATION

Time-dependent SHB is performed by exciting a subset of ions within a few-MHz-broad spectral region of the inhomogeneously-broadened absorption line using continuous-wave laser light at 1532.05 nm wavelength. The experimental setup is depicted in the top half of Fig. 6.1b. Optical pumping then leads to a modification of the absorption profile, which is characterized by sweeping the frequency of the light across the spectral hole using a phase modulator and serrodyne modulation. This allows characterization of level spacings and, if repeated after various delays, population dynamics.

The AFC is generated by optical pumping during 300 ms, as illustrated by the timing sequence in Fig. 6.1a. During this stage, the laser light is frequency-swept over a 6 GHz bandwidth by serrodyne phase-modulation while its intensity is modulated using an AOM. This procedure creates features of high (low pump power intensity) and low (high pump power intensity) absorption, as shown in Fig. 6.3 for a magnetic field of 16.5 kG and $\mathbf{B}\|\mathbf{c}$. A 30 ms time delay following the optical pumping step (see Fig. 6.1a) ensures that no noise-inducing photons that are spontaneously emitted from the $^4I_{13/2}$ excited-level mask the stored and re-emitted photons. Finally, photons are repetitively stored and re-emitted after 48 ns during a 200 ms time interval (see Fig. 6.1a). The closing of the first optical switch (which is open during the AFC preparation) in conjunction with the circulator allows suppressing stray pump light during the storage and reemission of the heralded single photons. Note that the light polarization and the magnetic field orientation are, respectively, set perpendicular and parallel to the c-axis of the crystal, i.e. $\mathbf{E}\perp\mathbf{c}$ and $\mathbf{B}\|\mathbf{c}$.

6.7.3. APPENDIX C: SPDC-BASED HERALDED SINGLE PHOTON SOURCE

As shown in Fig. 6.1, the creation of photon pairs begins with a mode-locked laser that emits pulses of 6 ps-duration at a rate of 80 MHz and a wavelength of 1047 nm. These pulses are frequency-doubled to 523.5 nm by means of second harmonic generation using a PPLN crystal and then used to pump a second PPLN crystal phase-matched for SPDC and creating frequency-correlated photon pairs at 795 nm and 1532 nm wavelength. After passing through an interference filter that removes the remaining 523 nm light, a dichroic mirror separates the photons from each pair. Finally, the bandwidth of each photon is reduced by filtering: we employ a 12 (6) GHz bandwidth fibre-Bragg grating (Fabry-Perot filter) for filtering the 1532 (795) nm photons. The 1532 nm photons are coupled into the waveguide (the second optical switch is open at this stage) and then stored. After reemission, they are detected by a superconducting nanowire single-photon detector (SNSPD) [41]. The heralding 795 nm photon is directly detected by another SNSPD.

6.7.4. APPENDIX D: DATA ACQUISITION AND $g^{(2)}$ MEASUREMENT

To collect data we employ a start-stop triggering method using a time-to-digital converter (TDC). The TDC starts with the detection of the heralding 795 nm photons, and it stops with the detection of heralded 1532 nm photons after being transmitted through, or re-emitted from, the waveguide. The TDC generates a histogram (shown in Fig. 6.4) that indicates the number of coincidence detections as a function of time delay between the start and the stop.

The measured coincidence rate before adding the memory was around 2300 s^{-1}. It is determined by the repetition rate of the pump laser (80 MHz), the mean photon-pair generation probability per pump pulse (1.6%), and several factors that limit the probability for detecting the created photons. They are the coupling efficiencies into fibre of around 70% for photons of both wavelength; transmission of the photons through long-pass filters (85% for both wavelength) and Fabry Perot cavities (40% and 60%), bandwidth mismatch between the pump and down-converted photons (17% and 35%) [42]; and detection efficiencies of the single photon detectors of around 70%. All brackets denote first the respective value for 795 nm, and then for 1532 nm photons. The multiplication of these factors leads to a predicted coincidence rate of 3170 s^{-1} – not far from the measured result. We attribute the difference to loss in fibre connectors and underestimation of the effect of bandwidth mismatch. Including the quantum memory system efficiency of 0.01%, and 33% extra loss due to an additional optical switch and a circulator then leads to a calculated coincidence rate for re-emitted photons of around 0.21 s^{-1}. This approximately matches the experimental value of 0.16 s^-1 that can be extracted from the coincidence peak centered around 48 ns in Fig. 6.4.

As explained in more detail in [43], the cross correlation function $g_{12}^{(2)}$ can be evaluated directly from the histogram by comparing true and accidental coincidence rates:

$$g_{12}^{(2)} = \frac{P_{12}}{P_1 P_2} = \frac{R_{true}}{R_{acc}}.$$

Here, R_{true}, which is proportional to P_{12}, denotes the coincidence detection rate of photons emitted simultaneously. These coincidences are represented by the peak at t=48 ns. Furthermore R_{acc} denotes the rate of accidental coincidences – it is proportional to P_1P_2 and the coincidences are represented by the peaks highlighted in gray in Fig. 6.4. For increased accuracy, we evaluated R_{acc} by averaging over five accidental coincidence peaks.

We note that an adsorber that is part of the cryogenic system broke shortly after we started measuring. This made it impossible to improve the data depicted in Fig. 6.4 and hence the cross-correlation function.

6.7.5. APPENDIX E: SUPERCONDUCTING NANOWIRE SINGLE-PHOTON DETECTORS (SNSPDS)

The SNSPDs used in our experiment feature a detection efficiency of around 70%, a time resolution of around 100 ps, a dead time of approximately 100 ns, and a dark count rate of 10-20 Hz. The signal created by each SNSPD is first amplified, shaped to a square pulse by a comparator, and then sent to a digital delay generator. The generator's two outputs are connected to the TDC and a counter.

6.8. ACKNOWLEDGMENTS

The authors thank Wolfgang Sohler, Mathew George, and Raimund Ricken for providing the Er^{3+}:Ti^{4+}:$LiNbO_3$ waveguide, Francesco Marsili for assistance with development of the SNSPDs, Jakob H. Davidson for help with aligning the waveguide, and Gustavo Amaral and Erhan Saglamyurek for useful discussions. This work is funded through Alberta Innovates Technology Futures (AITF), the National Science and Engineering Research Council of Canada (NSERC), and the Defense Advanced Research Projects Agency (DARPA) Quiness program. W.T. furthermore acknowledges funding by the Netherlands Organization for Scientific Research (NWO) and as a Senior Fellow of the Canadian Institute for Advanced Research (CIFAR), and V.B.V. and S.W.N. partial funding for detector development from the Defense Advanced Research Projects Agency (DARPA) Information in a Photon (InPho) program. Part of the detector research was carried out at the Jet Propulsion Laboratory, California Institute of Technology, under a contract with the National Aeronautics and Space Administration (NASA).

REFERENCES

[1] H. J. Kimble, *The quantum internet,* Nature **453**, 1023 (2008).

[2] A. I. Lvovsky, B. C. Sanders, and W. Tittel, *Optical quantum memory,* Nature photonics **3**, 706 (2009).

[3] N. Sangouard, C. Simon, H. De Riedmatten, and N. Gisin, *Quantum repeaters based on atomic ensembles and linear optics,* Reviews of Modern Physics **83**, 33 (2011).

[4] J. L. O'brien, A. Furusawa, and J. Vučković, *Photonic quantum technologies,* Nature Photonics **3**, 687 (2009).

[5] S. Tanzilli, W. Tittel, M. Halder, O. Alibart, P. Baldi, N. Gisin, and H. Zbinden, *A photonic quantum information interface,* Nature **437**, 116 (2005).

[6] C. M. Natarajan, M. G. Tanner, and R. H. Hadfield, *Superconducting nanowire single-photon detectors: physics and applications,* Superconductor science and technology **25**, 063001 (2012).

[7] T. Müller, J. Skiba-Szymanska, A. Krysa, J. Huwer, M. Felle, M. Anderson, R. Stevenson, J. Heffernan, D. A. Ritchie, and A. Shields, *A quantum light-emitting diode for the standard telecom window around 1,550 nm,* Nature communications **9**, 862 (2018).

[8] F. Bussières, N. Sangouard, M. Afzelius, H. De Riedmatten, C. Simon, and W. Tittel, *Prospective applications of optical quantum memories,* Journal of Modern Optics **60**, 1519 (2013).

[9] C. Thiel, T. Böttger, and R. Cone, *Rare-earth-doped materials for applications in quantum information storage and signal processing,* Journal of Luminescence **131**, 353 (2011).

[10] E. Saglamyurek, N. Sinclair, J. Jin, J. A. Slater, D. Oblak, F. Bussieres, M. George, R. Ricken, W. Sohler, and W. Tittel, *Broadband waveguide quantum memory for entangled photons,* Nature **469**, 512 (2011).

[11] C. Clausen, I. Usmani, F. Bussières, N. Sangouard, M. Afzelius, H. de Riedmatten, and N. Gisin, *Quantum storage of photonic entanglement in a crystal,* Nature **469**, 508 (2011).

[12] F. Bussières, C. Clausen, A. Tiranov, B. Korzh, V. B. Verma, S. W. Nam, F. Marsili, A. Ferrier, P. Goldner, H. Herrmann, *et al.*, *Quantum teleportation from a telecom-wavelength photon to a solid-state quantum memory,* Nature Photonics **8**, 775 (2014).

[13] T. Zhong, J. M. Kindem, J. G. Bartholomew, J. Rochman, I. Craiciu, E. Miyazono, M. Bettinelli, E. Cavalli, V. Verma, S. W. Nam, *et al.*, *Nanophotonic rare-earth quantum memory with optically controlled retrieval,* Science **357**, 1392 (2017).

[14] M. Sabooni, S. T. Kometa, A. Thuresson, S. Kröll, and L. Rippe, *Cavity-enhanced storage—preparing for high-efficiency quantum memories,* New Journal of Physics **15**, 035025 (2013).

[15] P. Jobez, I. Usmani, N. Timoney, C. Laplane, N. Gisin, and M. Afzelius, *Cavity-enhanced storage in an optical spin-wave memory,* New Journal of Physics **16**, 083005 (2014).

[16] T. Böttger, C. Thiel, R. Cone, and Y. Sun, *Effects of magnetic field orientation on optical decoherence in* Er^{3+}:Y_2SiO_5, Physical Review B **79**, 115104 (2009).

[17] B. Lauritzen, J. Minář, H. De Riedmatten, M. Afzelius, N. Sangouard, C. Simon, and N. Gisin, *Telecommunication-wavelength solid-state memory at the single photon level,* Physical review letters **104**, 080502 (2010).

[18] E. Saglamyurek, T. Lutz, L. Veissier, M. P. Hedges, C. W. Thiel, R. L. Cone, and W. Tittel, *Efficient and long-lived zeeman-sublevel atomic population storage in an erbium-doped glass fiber,* Physical Review B **92**, 241111 (2015).

[19] E. Saglamyurek, J. Jin, V. B. Verma, M. D. Shaw, F. Marsili, S. W. Nam, D. Oblak, and W. Tittel, *Quantum storage of entangled telecom-wavelength photons in an erbium-doped optical fibre,* Nature Photonics **9**, 83 (2015).

[20] L. Veissier, M. Falamarzi, T. Lutz, E. Saglamyurek, C. W. Thiel, R. L. Cone, and W. Tittel, *Optical decoherence and spectral diffusion in an erbium-doped silica glass fiber featuring long-lived spin sublevels,* Physical Review B **94**, 195138 (2016).

[21] M. Rančić, M. P. Hedges, R. L. Ahlefeldt, and M. J. Sellars, *Coherence time of over a second in a telecom-compatible quantum memory storage material,* Nature Physics **14**, 50 (2018).

[22] E. Miyazono, T. Zhong, I. Craiciu, J. M. Kindem, and A. Faraon, *Coupling of erbium dopants to yttrium orthosilicate photonic crystal cavities for on-chip optical quantum memories,* Applied Physics Letters **108**, 011111 (2016).

[23] M. Afzelius, C. Simon, H. De Riedmatten, and N. Gisin, *Multimode quantum memory based on atomic frequency combs,* Physical Review A **79**, 052329 (2009).

[24] P. Jobez, C. Laplane, N. Timoney, N. Gisin, A. Ferrier, P. Goldner, and M. Afzelius, *Coherent spin control at the quantum level in an ensemble-based optical memory,* Physical review letters **114**, 230502 (2015).

[25] Z.-Q. Zhou, W.-B. Lin, M. Yang, C.-F. Li, and G.-C. Guo, *Realization of reliable solid-state quantum memory for photonic polarization qubit,* Physical review letters **108**, 190505 (2012).

[26] M. Afzelius and C. Simon, *Impedance-matched cavity quantum memory,* Physical Review A **82**, 022310 (2010).

[27] S. A. Moiseev, S. N. Andrianov, and F. F. Gubaidullin, *Efficient multimode quantum memory based on photon echo in an optimal qed cavity,* Physical Review A **82**, 022311 (2010).

[28] A. D. Abazari, *Photon echo quantum memory and state transformation,* M.Sc. Thesis - University of Calgary (2009).

[29] C. W. Thiel, R. M. Macfarlane, R. L. Cone, Y. Sun, T. Bottger, K. D. Merkel, and B. W. R, *Spectroscopy and dynamics of Er^{3+}:$LiNbO_3$ at 1.5 microns for quantum information and signal processing applications,* 10th Intl Meeting on Hole Burning, Single Molecule, and Related Spectroscopies: Science and Applications - HBSM (2009).

[30] C. Thiel, R. Macfarlane, T. Böttger, Y. Sun, R. Cone, and W. Babbitt, *Optical decoherence and persistent spectral hole burning in er^{3+}:$linbo_3$,* Journal of Luminescence **130**, 1603 (2010).

[31] T. Böttger, C. W. Thiel, Y. Sun, R. M. Macfarlane, and R. L. Cone, *Decoherence and absorption of Er^{3+}:$KTiOPO_4$ (KTP) at 1.5 μm,* Journal of Luminescence **169, Part B**, 466 (2016).

[32] N. Sinclair, D. Oblak, C. W. Thiel, R. L. Cone, and W. Tittel, *Properties of a rare-earth-ion-doped waveguide at sub-kelvin temperatures for quantum signal processing,* Physical review letters **118**, 100504 (2017).

[33] M. F. Askarani, T. Lutz, M. G. Puigibert, N. Sinclair, D. Oblak, and W. Tittel, *Persistent atomic frequency comb based on zeeman sub-levels of an erbium-doped crystalline waveguide,* In preparation (2019).

[34] S. Fasel, O. Alibart, S. Tanzilli, P. Baldi, A. Beveratos, N. Gisin, and H. Zbinden, *High-quality asynchronous heralded single-photon source at telecom wavelength,* New Journal of Physics **6**, 163 (2004).

[35] P. Tapster and J. Rarity, *Photon statistics of pulsed parametric light,* Journal of Modern Optics **45**, 595 (1998).

[36] M. Nilsson, L. Rippe, S. Kröll, R. Klieber, and D. Suter, *Hole-burning techniques for isolation and study of individual hyperfine transitions in inhomogeneously broadened solids demonstrated in* $Pr^{3+}:Y_2SiO_5$, Physical Review B **70**, 214116 (2004).

[37] B. Lauritzen, S. Hastings-Simon, H. De Riedmatten, M. Afzelius, and N. Gisin, *State preparation by optical pumping in erbium-doped solids using stimulated emission and spin mixing,* Physical Review A **78**, 043402 (2008).

[38] M. Afzelius, I. Usmani, A. Amari, B. Lauritzen, A. Walther, C. Simon, N. Sangouard, J. Minář, H. De Riedmatten, N. Gisin, *et al.*, *Demonstration of atomic frequency comb memory for light with spin-wave storage,* Physical review letters **104**, 040503 (2010).

[39] N. Sinclair, E. Saglamyurek, H. Mallahzadeh, J. A. Slater, M. George, R. Ricken, M. P. Hedges, D. Oblak, C. Simon, W. Sohler, *et al.*, *Spectral multiplexing for scalable quantum photonics using an atomic frequency comb quantum memory and feed-forward control,* Physical review letters **113**, 053603 (2014).

[40] I. Baumann, R. Brinkmann, M. Dinand, W. Sohler, L. Beckers, C. Buchal, M. Fleuster, H. Holzbrecher, H. Paulus, K.-H. Müller, *et al.*, *Erbium incorporation in* $LiNbO_3$ *by diffusion-doping,* Applied Physics A **64**, 33 (1996).

[41] F. Marsili, V. B. Verma, J. A. Stern, S. Harrington, A. E. Lita, T. Gerrits, I. Vayshenker, B. Baek, M. D. Shaw, R. P. Mirin, *et al.*, *Detecting single infrared photons with 93% system efficiency,* Nature Photonics **7**, 210 (2013).

[42] J. Jin, M. G. Puigibert, L. Giner, J. A. Slater, M. R. Lamont, V. B. Verma, M. Shaw, F. Marsili, S. W. Nam, D. Oblak, *et al.*, *Entanglement swapping with quantum-memory-compatible photons,* Physical Review A **92**, 012329 (2015).

[43] A. Kuzmich, W. Bowen, A. Boozer, A. Boca, C. Chou, L.-M. Duan, and H. Kimble, *Generation of nonclassical photon pairs for scalable quantum communication with atomic ensembles,* Nature **423**, 731 (2003).

7

CONCLUSION AND OUTLOOK

Erbium-doped host materials are promising candidates to serve as quantum memories operating at telecommunication wavelength for quantum repeaters. Towards an ultimate workable telecom-compatible quantum memory, spectroscopic investigations and storage demonstrations over different host materials should be implemented, which would reveal the capabilities of these materials to be the final candidate. We have reported such studies in two different erbium-doped host materials in this thesis. We also outline potential future projects, including the optimization of the current materials, exploration of other potential telecom-compatible materials, and other applications of erbium-based host materials.

7.1. SUMMARY OF RESULTS

In this thesis, four experiments have been reported. Here, I will summarize the outcomes of each.

- We have investigated coherence properties of an erbium-doped fiber in view of quantum memory applications using spectroscopic techniques such as two- and three-pulse photon echos. A maximum coherence time of 300 ns has been found at 600 mK, which is mainly limited by the intrinsic features of glassy materials, namely two-level-systems (TLSs). Extrapolating observations, ultra low temperatures could reduce the effect of TLSs and thereby significantly increase the coherence time. Another important outcome of this study is that we have found coherence times at small magnetic fields (around 500 G) at which Zeeman lifetimes can be as long as seconds. Hence, we identified operating conditions at which good coherence and the possibility for spectral hole burning exist simultaneously.

- We have implemented a hybrid quantum channels composed of two AFC-based quantum memories functioning at different wavelengths and a wavelength non-degenerate SPDC-based entangled photon-pair source. More precisely, we have shown entanglement preservation after storage of photonic time-bin qubits in these two quantum memories; one is a thulium-doped crystal operating at 794 nm wavelength and the other is an erbium-doped fibre operating at 1535 nm wavelength. Moreover, the violation of the CHSH Bell-inequality after storage and re-emission has been shown to demonstrate the non-locality.

- We have characterized lifetime of ground-state Zeeman levels and their applicability for AFC-based quantum memory in an erbium-doped lithium niobate crystal waveguide. We have found the longest lifetime achieved for ground-state Zeeman levels in any erbium-doped crystal. We have also created AFC structures using these levels as long-lived population reservoir. Surprisingly, we have observed an increase in the background optical depth of the AFCs with the AFC bandwidth, leading to reduction in the memory efficiency. Spectroscopic methods have been employed to diagnose the mechanisms causing this detrimental effect. We have conjectured that laser-induced excitation of TLSs leads to relaxation of erbium ions in the ground-state Zeeman levels, resulting in an increasing background optical depth with increase in the AFC bandwidth.

- We have reported quantum storage using an erbium-doped lithium niobate crystal waveguide. Heralded telecom-wavelength photons, generated from a SPDC-based single photon source, are stored in the AFC-based waveguide quantum memory. The non-classical nature of the re-emitted photons has been proven by measuring second-order cross correlation function. Although we found low efficiency and short storage time; this work represented the first demonstration of quantum storage in an erbium-doped crystal.

7.2. POTENTIAL FUTURE PROJECTS

Improvement of the current erbium-based quantum memories
There are many obstacles that prevent one to achieve a workable erbium-based quantum memory using echo-based memory schemes, including the AFC scheme. The main difficulty is to find a proper long-lived shelving level. In the ideal case, such a level needs a lifetime that is much greater than the excited level lifetime and preferably no spin-inhomogeneous broadening; the former enhances the optical pumping efficiency and the latter prevents spectral hole-filling. Both factors play significant roles to achieve a quantum memory with high storage efficiency. Regarding the erbium-doped fiber quantum memories, further decreasing the temperatures may increase not only the coherence time, which is an upper-bound for storage time, but also the storage efficiency, by minimizing the effect of the two-level-system. Furthermore, a larger magnetic field would help diminishing the effect of spin flip-flops and thereby enhance the storage efficiency and storage time. Regarding the erbium-doped lithium niobate crystal, the main issue is the presence of a large background optical depth, which impedes achieving a high efficient quantum memory. This damaging effect is due to defects and imperfections in the host crystal, which makes it a quasi-amorphous host. The obvious solution to tackle such an issue is to improve the crystal growth, which would yield a crystal with less defects and imperfections. Also, temperature- and magnetic field-dependent spectroscopic studies may reveal other potentially-damaging effects.

Exploring telecom-wavelength transitions in other REI-doped materials
Another path towards workable telecom-compatible quantum memories is to explore other materials to find a suitable telecom-wavelength transition. One of the potential REI-doped materials are thulium-doped crystals, in which the transition from the $^3F_4$ to $^3H_4$ level is around 1450 nm wavelength. In this case, the $^3H_6$ level, which is the ground state in thulium, can be employed as the shelving level, with infinite lifetime for, in particular, AFC-based quantum memories. Moreover, since the transition frequency from the $^3H_6$ to the $^3F_4$ level is on the order of 100 THz, there would be no phonon-induced population relaxation between these two levels. As a result, the optical pumping could be performed highly efficiently. However, a large numbers of spectroscopic measurements would be required to asses the suitability of this in the context of quantum memory not yet studies transition.

Telecom-wavelength REI-doped materials as telecom-to-microwave quantum transducers
Recently, much attentions have been drawn towards building quantum transducers via which microwave photons are converted into optical photons, most importantly to telecom-wavelength photons. Such transducers can be utilized to connect widely-spaced superconductor-based quantum computers through flying telecom-wavelength qubits, as well as to perform a deterministic Bell-state measurement through a CNOT gate at half distance between two superconducting qubits. O'Brien and et al. devised a proposal that allows one to build a transducer via erbium-doped materials relying on photon-echo based memory schemes. In this proposal, three ground state sub-levels are required to implement the quantum transducer; two of which are employed for the engineering of the absorp-

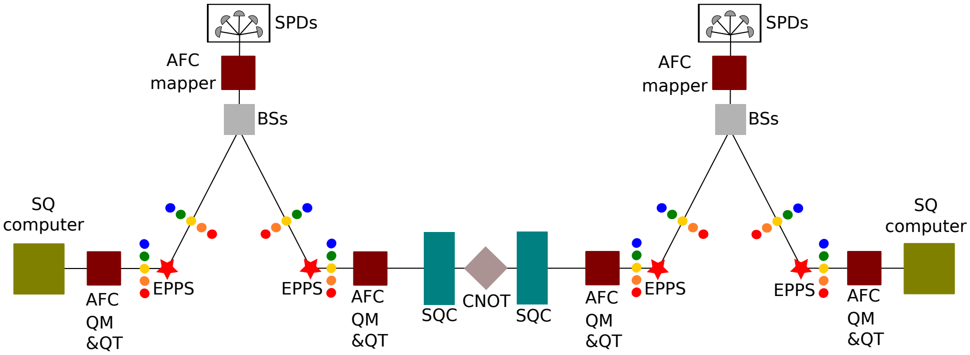

Figure 7.1: Schematic of a spectrally-multiplexed quantum repeater architecture, including future projects discussed in the text, and making use of erbium-doped materials. These materials can be employed as spectrally-multiplexed quantum memories, spectrally-multiplexed quantum transducers, and frequency-to-space mappers. BS, SPD, AFC QM & QT, SQC, and SQ computer stand for beam-splitter, single photon detector, atomic frequency comb quantum memory and quantum transducer, superconducting quantum circuit, and superconducting quantum computer, respectively. EPPSs are spectrally-multiplexed entangled photon-pair sources at telecom-wavelength. These sources and spectrally-multiplexed QMs are utilized to increase the entanglement distribution rate across the repeater links. The AFC mapper is a telecom-compatible spectrally- and spatially-multiplexed device that is used to map spectral modes to spatial modes. The AFC QT is employed to transduce bidirectionally telecom-to-microwave photons, which is also responsible feed-forward mode mapping; the selected optical frequency mode is transduced to its respective microwave mode. SQCs are superconducting qubit through which deterministic entanglement swapping is performed by means of a a CONT gate. All the elements inside the dotted rectangle are placed on a superconducting microwave resonator. See [1–4] for detailed description of the individual parts.

tion profile via spectral hole burning, and the other one is used to couple optical coherence to microwave coherence. Provided problems with fast relaxation can be solved, superhyperfine sub-levels of erbium may be utilized towards this end.

A telecom-compatible frequency-to-space mapper

In a spectrally-multiplexed quantum repeater architecture, the photonic Bell-state measurement potentially involves arrays of diffraction gratings, frequency-to-space mappers, and single photon detectors. Unfortunately, diffraction gratings suffer from their low spectral resolution. Alternatively, REI-doped materials with engineered-absorption profile via spectral hole burning can also be utilized to serve as frequency-to-space mappers; they offer high resolutions as they possess narrow homogeneous linewidths over a broad frequency range [4]. Furthermore, these devices are required to be telecom compatible which makes erbium-doped materials a prime candidate.

REFERENCES

[1] N. Sinclair, E. Saglamyurek, H. Mallahzadeh, J. A. Slater, M. George, R. Ricken, M. P. Hedges, D. Oblak, C. Simon, W. Sohler, *et al.*, *Spectral multiplexing for scalable quantum photonics using an atomic frequency comb quantum memory and feed-forward control,* Physical Review Letters **113**, 053603 (2014).

[2] M. G. Puigibert, G. Aguilar, Q. Zhou, F. Marsili, M. Shaw, V. Verma, S. Nam, D. Oblak,

and W. Tittel, *Heralded single photons based on spectral multiplexing and feed-forward control,* Physical Review Letters **119**, 083601 (2017).

[3] C. O'Brien, N. Lauk, S. Blum, G. Morigi, and M. Fleischhauer, *Interfacing superconducting qubits and telecom photons via a rare-earth-doped crystal,* Physical Review Letters **113**, 063603 (2014).

[4] V. Crozatier, G. Gorju, V. Lavielle, A. Louchet, F. Bretenaker, T. Chaneliere, F. Goldfarb, and J.-L. L. Gouët, *Solid state atomic processors for light,* Journal of the European Optical Society - Rapid publications **3** (2008).

A

SUPPLEMENTARY INFORMATION FOR CHAPTER 4

This appendix complements the results reported in chapter 4, which presents the experiment where entanglement and nonlocality between disparate solid-state quantum memories mediated by photons has been demonstrated.

A detailed schematic of our setup is shown in Fig. A.1. In the following we explain the different components.

TIME-BIN ENTANGLED PHOTON-PAIR SOURCE

To generate time-bin entangled photon pairs, we employed a 1047 nm wavelength laser (pump laser) emitting 6 ps-long pulses at an 80 MHz repetition rate. A small part of this signal was sent to a photo-detector that created the reference clock for all measurements. The remaining portion of the pump laser light was directed to a 2 cm-long periodically-poled lithium niobate crystal (PPLN), phase-matched for second-harmonic generation (SHG). The then 18 ps-long pulses, centered at 523.5 nm wavelength, traveled through an unbalanced free-space Mach-Zehnder interferometer (MZI) whose path-length difference corresponded to 1.4 ns travel time difference, thereby creating pulses of light in early and late temporal modes (or time-bins). The emerging pulses were used to pump a second 2 cm long PPLN crystal, where, with small probability of around 1.6%, spontaneous parametric down conversion (SPDC) occurred, in which a pump photon is annihilated and a photon pair is created in the maximally entangled state $|\phi\rangle = \frac{1}{\sqrt{2}}(|ee\rangle + |\ell\ell\rangle)$.

As determined by energy conservation and phase-matching, the down-converted photons' wavelengths were centered around 794 nm and 1535 nm – compatible with our quantum memories. Prior to storage, the 1535 nm photons were filtered to 8 GHz bandwidth using an air-spaced Fabry-Perot cavity (FP) in order to match the bandwidth of the erbium memory. In the case of the 794 nm photons, we took advantage of the fact that the inhomogeneous broadening of Tm in $LiNbO_3$ extends beyond the 10 GHz-wide AFC: photons outside the AFC bandwidth will be absorbed by Tm ions, eventually be spontaneously re-emitted into random directions, and hence have a negligible probability to reach the detector. This enables restricting the photons' bandwidth without the need for an external filter and thereby reduces complexity and loss. Unfortunately, this approach is not possible in the case of erbium because the fibre guides the absorbed and spontaneously emitted photons (outside the AFC's bandwidth) preferentially towards the detector, thus creating noise.

QUANTUM MEMORIES

KRAMERS AND NON-KRAMERS IONS

When doped into inorganic crystals, rare-earth elements generally form triply positively (3+) charged ions. Ions with and odd and even number of electrons in their 4f orbital are referred to as Kramers and non-Kramers ions, respectively. Er^{3+} and Tm^{3+} are, in this order, examples for these two classes. In the following, we will discuss the principal differences between Kramers and non-Kramers ions, and their impact on the use as quantum memory and quantum transduction.

As they have a half-integer spin, Kramers ions feature an unquenched electronic magnetic moment. When doped into crystals, this results in rapid spin-spin relaxation (spin flip-flops) at small magnetic fields, where the spin levels are equally thermally populated. However, by increasing the magnetic field (and hence the electronic Zeeman level splitting), spin-lattice relaxation becomes dominant due to a rapidly growing phonon density of states. Both relaxation mechanisms shorten the electron spin level

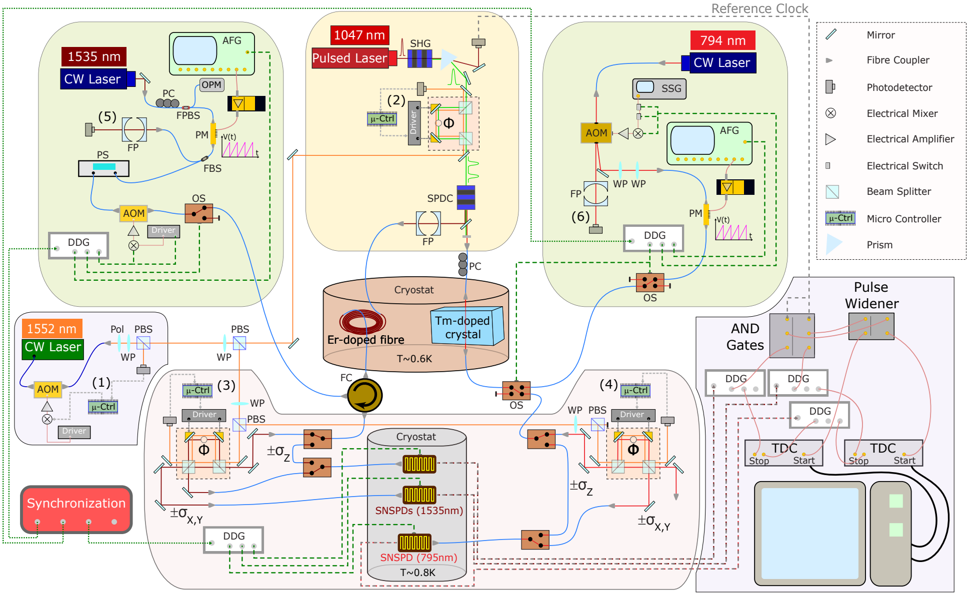

Figure A.1: The figure is divided into six panels that compose the four parts described in the main text: top left panel: erbium preparation; top center panel: photon pair source; top right panel: thulium preparation; bottom center panel: measurement, analysis and detection; bottom left panel: stabilization source; bottom right panel: electronics and computer software. Red and dark-red lines denote 794 nm and 1535 nm nm photons traveling in free space, respectively, and orange lines denote stabilization light. The blue wavy lines depict optical fibers for both wavelengths. All other lines depict electronic cables. SSG: synthesized signal generator; Driver: multipurpose signal driver.

lifetime, thereby limiting the efficiency of the optical pumping and, as a consequence, the suitability of Kramers ions at small or moderate magnetic fields for AFC-based quantum memory.

However, at magnetic fields in excess of a few Tesla, only the lowest electronic Zeeman level is thermally populated, resulting in the absence of spin flip-flops. As has been shown recently, it is then possible to use long-lived hyperfine levels (arising from the coupling between nuclear and electronic spins) for efficient optical pumping[1].

Note that the high magnetic-field sensitivity of the electronic Zeeman splitting of Kramers ions makes them interesting for optical-to-microwave transduction[2, 3] since a transition of a few GHz—the typical level spacing of superconducting qubits—can be achieved by a small external magnetic field. This benefits coherence times of the closely-located superconducting qubits.

Conversely, non-Kramers ions, which do not possess electron spin sub-levels owing to a quenched electronic magnetic moment, appear more suitable for photon-echo-based quantum memory due to their long-lived nuclear Zeeman and hyperfine levels. Their usefulness for optical-to-microwave transduction is limited due to the small magnetic field-dependence of their nuclear Zeeman splittings and hence the need for large magnetic fields to achieve a level splitting of a few GHz.

Note that it is reasonable to assume that the fundamental difference between the two types of rare-earth ions affects the sensitivity of a particular ion's spectroscopic properties to host imperfections. Hence, a good host crystal for one ion is not necessarily a good one for an ion from the other class.

THE AFC PROTOCOL

When a single photon in a well-defined temporal mode is collectively absorbed by ions in an AFC at time $t = 0$, the result is a so-called Dicke state of the form

$$|\psi\rangle_A = \frac{1}{\sqrt{N}} \sum_{j=1}^{N} c_j e^{-i2\pi n_j \Delta \cdot t} e^{ik\cdot z} |\mathrm{g}_1, ..., \mathrm{e}_j, ..., \mathrm{g}_N\rangle . \tag{A.1}$$

Here, g denotes the atomic ground state and e the excited state, k is the wave number and z the propagation direction of the light, and $j = 1..N$ labels the ions interacting with the photon with weighted amplitudes c_j (c_j depends on the ion's detuning $n_j\Delta$ with respect to the centre frequency of the photon and on its position within the absorbing medium)[4].

ERBIUM DOPED FIBRE - AFC PREPARATION

Continuous-wave telecommunication-wavelength light at 1535 nm (Er-memory preparation light) was injected from a diode laser into a single-mode optical fibre. A polarization controller (PC) and a fibre-coupled polarization beam splitter (FPBS) with one of its outputs connected to an optical power meter (OPM) allowed controlling the intensity in the second output of the FPBS. The light was then directed to a phase modulator (PM), employed to serrodyne shift its frequency in discrete intervals (each defining a region in which spectral hole-burning took place). The PM was driven by an arbitrary function generator (AFG) connected to an electrical amplifier, allowing for shifts up to ± 10 GHz.

After the PM, the light went through a polarization scrambler (PS) with scrambling frequency of 6 kHz, used to address all erbium ions despite their randomly oriented transition dipole moments (this is caused by the amorphous SiO_2 host). In-between the PS and the erbium-doped fibre, an acousto-optic modulator (AOM) was placed. It was driven by 500 ms-long electrical pulses that were synchronized to the master clock. The amplitude of the pulses could be controlled for optimal AFC preparation. In addition, we also inserted a latch-mode optical switch (OS) and a fibre-pigtailed circulator (FC). The OS was connected to port #1 of the FC while port #2 was connected to the Er-doped fibre, and port #3 to the analyzers.

The Er-doped fibre was exposed to a 1500 G magnetic field, which lifts the degeneracy of the electronic ground state and creates two long-lived Zeeman levels with second-long lifetimes.

The interaction between the modulated pump light and the erbium ions leads to frequency-selective persistent spectral hole burning, and, after 1000 repetitions of the 500 μs-long burning sequence, to an 8-GHz-wide AFC (see Fig. A.1 in the main text for a 1 GHz-wide central section). After a wait time of 200 ms, included to ensure the decay of ions from the excited level (avoiding spontaneously emitted photons during the subsequent step), we repeatedly sent, stored (for 6 ns), and retrieved members of photon pairs for a total of 700 ms. During this phase of the experimental cycle, the optical switch was toggled to prevent memory preparation light from leaking into the single-photon detectors. See Fig. A.2 for a timing diagram.

To read the AFC, port #3 of the FC was connected to a photo-detector followed by an oscilloscope. After the preparation of the AFC, a reading waveform was applied to the PM, which scanned the laser frequency across the prepared spectral structure from -1 to +1 GHz while transmission was monitored. To calibrate the measured optical depth (OD), and hence estimate the AFC efficiency, we recorded the transmitted intensity of another 2 ms-long pulse that burned a narrow spectral section to complete transparency.

THULIUM-DOPED LITHIUM NIOBATE CRYSTAL - AFC PREPARATION

Visible-wavelength light at 794 nm (Tm-memory preparation light) was generated by a diode laser. To obtain a clean spatial mode, the beam was coupled into and out of a single-mode optical fibre. The light was then directed to a single-pass AOM, creating 20 ms-long pulses, and the deflected first-order beam steered to a set of wave-plates for polarization control before being coupled into a fibre-pigtailed PM. Similar to the Er memory preparation, the PM was driven by an AFG and an electrical amplifier for serrodyne shifting. Each sweep took 1 ms and was repeated 20 times per preparation sequence (see Fig. A.2).

After serrodyne shifting in the PM, the light was directed to two fibre-pigtailed optical switches that allowed for routing collimated memory preparation light and single-photons in and out of the crystal while avoiding leakage of the classical light into the waiting and storage periods.

The crystal was cooled to 0.6 K and exposed to a 125 G magnetic field aligned along its C_3 axis, resulting in two nuclear Zeeman sub-levels. Due to their long lifetimes, on the order of minutes, the interaction between the preparation light and the thulium ions leads

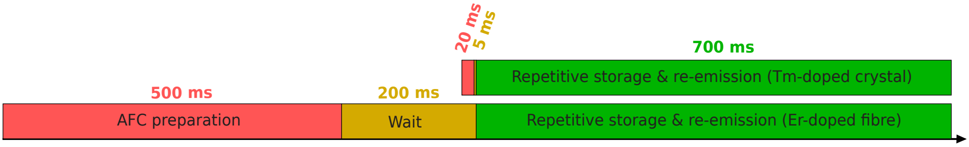

Figure A.2: Shown are synchronized preparation, wait and storage periods for the two memories.

to persistent spectral holes and allowed creating a 10-GHz-wide AFC (see Fig. 1 in the main text for a 1 GHz-large central section). After a waiting time of 5 ms to avoid spontaneous emission noise, a 700 ms-long storage period was started during which many photons were stored and re-emitted 32 ns later. However, due to spurious modulation of the AFC with periods different from Δ=1/32 ns ~31 MHz, there were two additional moments at which partial rephasing occurred, namely after half and twice the intended storage time $1/\Delta$ (see Fig. 2 in the main text). This is confirmed by the Fourier transform of the measured AFC structure, shown in Fig. A.3.

OPTIMIZATION OF MAGNETIC FIELD

To optimize an AFC for quantum state storage, it is necessary to carefully set the magnetic field to which an ensemble of rare-earth-ions is exposed. In the case of two different ensembles, this implies the need to tune both fields individually. However, in this investigation both fields were created by the same superconducting solenoid (the field difference is due to the ensembles being in different locations with respect to the solenoid), and individual adjustment, and hence optimization of the individual storage efficiencies, was impossible. Instead, we chose a setting that resulted in the best overall efficiency.

More precisely, the erbium-doped fibre requires a magnetic field of around 1500 G to allow for quantum state storage (at other fields spin relaxation prevents efficient optical pumping, as discussed above).

At this setting, the field at the location of the Tm-crystal is only around 125 G, leading to small nuclear Zeeman splitting. As is always the case if the ground state splitting is smaller than the AFC bandwidth, optical pumping must be tailored to transfer atomic populations from troughs of the AFC to neighboring teeth. Hence, storage time—given by the inverse tooth spacing— and level splitting are not independent anymore. In addition, such cross-pumping results in a finesse (the ratio between the teeth spacing and the teeth width) of 2, thereby limiting the storage efficiency[4]. In short, the storage time and the maximum efficiency of the Tm memory are both determined by the need to expose the Er memory to a particular magnetic field. However, since the ground-state electronic Zeeman splitting of erbium exceeds the AFC bandwidth, the storage time in the erbium memory is only limited by the coherence time – it is not determined by the level splitting.

SYSTEM AND DEVICE EFFICIENCIES

The analysis of the internal efficiencies of the two memories was conducted based on the following two methods. First, by comparing the detection rate of the recalled photons at the output of the cryostat with that of all photons input into the cryostat, we calculated

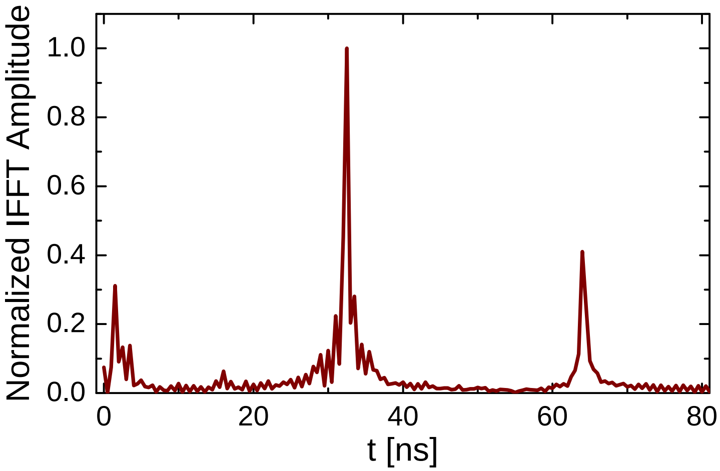

Figure A.3: Inverse Fourier transform of the Tm AFC spectrum (a 1 GHz-broad section is shown in the inset of Fig. 1d in the main text), showing possible recall times of 16ns, 32 ns and 64 ns.

the system efficiency: $\eta_{\text{system}} = R_{out}/R_{in}$. In addition to the actual probability for absorbing and re-emitting photons—the internal efficiency— the system efficiency also includes fibre transmission and, for the Tm memory, coupling in and out of the crystal. To estimate the latter two (jointly referred-to as η_{coupling}), we burned a fully transparent spectral hole in the absorption profile of the rare-earth ions using strong light, and then evaluated the ratio of output power over input power: $\eta_{\text{coupling}} = P_{out}/P_{in}$. The internal efficiency can then be calculated using $\eta_{\text{device}} = \eta_{\text{system}}/\eta_{\text{coupling}}$.

In the case of the erbium-doped fiber, the input count rate was 417 Hz, and the rate of retrieved photons behind the cryostat was 1.8 Hz (both rates were measured in coincidence with the heralding photon). This translates approximately into a 0.1% system efficiency. Taking into account a 20% coupling efficiency, we find a internal efficiency of 0.5%. For the thulium-doped crystal quantum memory, identical measurements resulted in 0.4% for the system and 2.0% for the internal efficiency.

Alternatively, we estimated the internal efficiency through the analysis of the AFC spectral profile, which we obtained as described in the *AFC preparation* section of the Methods (see Fig. 1 in the main text for two examples). The values of the optical depth of the remaining background due to imperfect optical pumping (d_0) and the optical depth of the teeth (d_1), as well as the Finesse (F) was inferred by fitting a train of Gaussian functions to the acquired profiles. Then, by using[4]

$$\eta_{device} = (d_1/F)^2 e^{-d_1/F} e^{-7/F_2} e^{-d_0}, \tag{A.2}$$

we calculated the internal efficiency. We found 0.5% for the erbium memory and 2% for the thulium memory, consistent with the values estimated using the first method.

OPTIMIZATION OF MEMORY WAVELENGTHS

The coincidence count rates in our experiments depend on several interrelated factors, which have to be optimized jointly: the need for energy correlations between the pho-

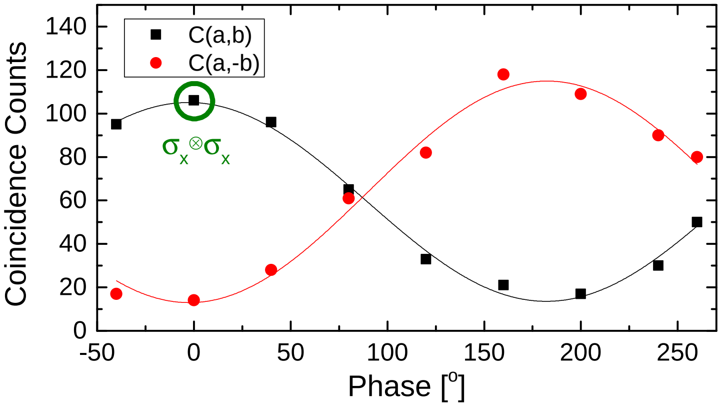

Figure A.4: Visibility curve taken by fixing the phases of the pump and 1535 nm interferometers to 0, and sweeping the 794 nm interferometer's piezo voltage, i.e. phase. The y-axis shows coincidences between the clock signal, and detections of the re-emitted 794 nm and transmitted 1535 nm photons. The accumulation time per data point was 60 seconds. The set of phases that define the $\sigma_x \otimes \sigma_x$ projection corresponds to the point of the curve where C(a,b) is maximum and C(a,-b) minimum.

tons belonging to each pair, and the wavelength-dependent storage efficiencies in both memories. To optimize the rate, we measured the device efficiencies as a function of the wavelengths of the two photons produced by the source. The results are presented in Table A.1.

CONTROL AND STABILIZATION

The experimental setup depicted in Fig. A.1 contains many individual elements that must be controlled to ensure physical parameter stability—in particular wavelengths, intensities and phases—throughout the measurements. Four feedback loops were used, allowing for intensity stabilization of the laser used for phase stabilization of various interferometers ((1) in Fig. A.1); phase stabilization of the pump interferometer ((2) in Fig. A.1); and phase stabilization of the two analyzing interferometers ((3) and (4) in Fig. A.1). Furthermore, to assure that the wavelengths of the lasers used for memory preparation were stable, wavelength control was required ((5) and (6) in Fig. A.1).

INTENSITY STABILIZATION – FEEDBACK LOOP 1

Continuous-wave light was generated by a fibre-coupled and internally frequency-locked 1532 nm wavelength laser. After passing through a fibre-pigtailed AOM, used to modulate the light intensity, it was collimated and sent through a bulk-optics polarizer, a wave-plate and a PBS. One output was subsequently used for interferometer stabilization (see below), and the other coupled to a free-space variable-gain photo-detector. To stabilize the intensity of the light in the former output, the detector signal was used as a parameter for the AOM's modulation signal.

PHASE STABILIZATION – FEEDBACK LOOPS 2-4

The frequency- and intensity-stabilized light, split into three individually intensity-controlled beams, was injected into and detected behind each interferometer. Due to interference, any phase variation then caused a variation of the light intensity measured by the corresponding detector. In turn, this allowed locking the interferometers to specific phases using piezo-mounted mirrors.

Fig. A.4 displays typical single detection rates (accumulated during 60 seconds per data point) in the case where the pump interferometer and the interferometer analyzing the 1535 nm photons were fixed, and the phase of the 794 nm interferometer was swept from 0^o to 360^o; the set of phases that corresponds to the $\sigma_x \otimes \sigma_x$ projector is highlighted.

LASER STABILITY MONITORING – CIRCUITS 5 AND 6

To ensure wavelength stability of the 1535 nm memory preparation laser, we collected a fraction of the emitted light using a fiber beam splitter (FBS) inserted behind the PM. This light was then directed to a Fabry-Perot (FP) optical cavity, detected by a photodetector, and monitored on an oscilloscope. This allowed us to observe fluctuations of the laser's wavelength. The wavelength of the 794 nm preparation laser was similarly monitored by another FP cavity.

DATA COLLECTION AND ANALYSIS

PHOTON DETECTION AND DATA COLLECTION

The 794 nm and 1535 nm photons were detected using tungsten silicide (WSi) superconducting nanowire single-photon detectors (SNSPDs) cooled inside a sorption fridge to ~0.8K. Each detector's efficiency was optimized for the wavelength of the detected photons[5]. The average photon-detection efficiency, including fibre loss inside the cryostat, was measured to be 70 % for all detectors. The temporal jitter of all detectors was around 250 ps, and the dark count rates below 100 Hz. To adjust arrival times of detection signals at the TDC, digital delay generators (DDGs) were placed at the outputs of the SNSPDs (see Fig. A.1), and to avoid detections of leaked preparation light, the detectors were only enabled during the storage period.

As the 80 MHz clock rate was too high to start the TDC, we instead used a downsampled version generated from an AND gate that additionally received signals from 1535 nm photon detections. All non-relevant start signals, i.e. starts that were not associated with photon pair detections, were discarded.

ACQUISITION OF CORRELATIONS

Most of the data is recorded in the form of coincidence counts (per time) or rates. By a coincidence we mean detections in two detectors (labelled 1 for the 1532 nm and 2 for the 794 nm detector) that are separated by some time δt. Let us denote the probability for such a coincidence with detections at time t and $t+\delta t$ as $P_{12}(t; t+\delta t)$. If we define the time when detector 1 detects a photon to be 0, we can simplify $P_{12}(0; 0+\delta t) = P_{12}(\delta t)$.

In the experimental setup the optical and electronics delays have been aligned such that photons generated as members of the same photon pair will, before storage, be detected in coincidence at $\delta t = 0$. The second-order cross-correlation function can be expressed as $g_{12}^{(2)}(\delta t) = P_{12}(\delta t)/P_1(0)P_2(\delta t)$, where $P_1(0)$ and $P_2(\delta t)$ denote the probabilities of individual detection at the two times relevant for the coincidence detection. Experimentally, rather than ensuring these individual detection probabilities and the calculation the normalization constant, it is more convenient to extract the product $P_1(0)P_2(\delta t)$ from the coincidence detection data. To do this we note that the repetition period of our pump laser is 12.5 ns. Moreover, since the photon-pair generation process is spontaneous, there are no statistical correlations between subsequently emitted pairs. Hence, the coincidence detection probability $P_{12}(0;12.5ns)$ equals the product of the probabilities for individual detections of two uncorrelated photons (i.e. photons from independent pairs emitted 12.5 ns apart): $P(0;12.5\text{ ns}) = P_1(0)P_2(12.5\text{ ns})$.

Such coincidences are commonly referred to as accidental coincidences, and the coincidence rates are identical for any time difference that is an integer multiple of the repetition period, $\delta t = n \times 12.5$ ns ($\mathrm{n} \in \mathbb{Z} \neq 0$). Furthermore, since the probability to detect individual photons is the same for all repetitions, $P_2(12.5\text{ ns}) = P_2(0)$. It is now easy to see that $g_{12}^{(2)}(0) = P_{12}(\delta t = 0)/P_{12}(\delta t = 12.5\text{ ns})$. In other words, we can assess the cross-correlation function as the ratio between "true" coincidences and "accidental" coincidences.

The central assumption in our further data analysis is that cross-correlations, caused by photons from the source, must obey the same principle regardless the value of δt, i.e. we can write $g_{12}^{(2)}(\delta t) = P_{12}(\delta t)/P_{12}(\delta t + 12.5\text{ ns})$. This allows us to express $g_{12}^{(2)}(\delta t)$ as a ratio of coincidence count rates [6]

$$g_{12}^{(2)}(\delta t) = \mathrm{R}(\delta t)/\langle \mathrm{R}(\delta t + 12.5\mathrm{ns})\rangle_{\mathrm{n}}, \tag{A.3}$$

where $P_{12}(\delta t) = \alpha \mathrm{R}(\delta t)$ with a proportionality factor α that cancels in $g_{12}^{(2)}$, and "$\langle .. \rangle_{\mathrm{n}}$" denotes averaging over several repetition periods n, in order to reduce the statistical uncertainty of the measurement. Specifically, we chose $n = \{[-5,-1],[1,5]\}$.

Fig. 2 of the main text depicts cross-correlation functions for different δt, calculated according to Eq. (A.3). For this measurement we align the timing such that, without storage, the transmitted photons are in coincidence for $\delta t = 0$. With storage, however, we herald using detections of 1535 nm photons that have been stored for 6 ns. Hence, we expect the non-absorbed 795 nm photons to be in coincidence at $\delta t = -6$ ns, with accidental coincidences at $\delta t = (-6 + n \times 12.5)$ ns. The stored and recalled 795 nm photons will, on the other hand, give rise to coincidences at $\delta t = (32-6)$ ns = 26 ns, with accidental coincidences at $\delta t = (26 + n \times 12.5)$ ns. Fig. 2 of the main text shows that the $g_{12}^{(2)}$ only exceeds the classical bound at the two aforementioned delays as well as at $\delta t = 10$ ns and $\delta t = 56$ ns, which are erroneously re-emitted photons due to AFC imperfections (see Fig. A.3). An important observation is that even if the accidental coincidence peaks are large, the corresponding cross-correlation remain well below the classical bound, reflecting independent (non-quantum) nature of the detections.

Another interesting feature is that the cross correlation after storage is significantly larger [$g_{12}^{(2)}(26\text{ ns}) = 53 \pm 8$] than before storage [$g_{12}^{(2)}(-6\text{ ns}) = 3.9 \pm 0.1$]. To understand this, let us point out that, in order to minimize loss, we decided to spectrally filter the 794 nm photons only using the AFC memory, and not to put any filter cavity directly behind the source (as in the case of the 1535 nm photons). Hence, coincidences between filtered heralding photons at 1535 nm and unfiltered 794 nm photons (before storage) will contain significant contributions from uncorrelated 794 nm photons outside the AFC bandwidth. However, these contributions are eliminated when measuring coincidences with recalled 794 nm photons because these photons must be spectrally overlapped with the AFC and, thus, match the spectrum of the heralding photons. This explanation is supported by the data in Fig. A.5 for the values of $g_{12}^{(2)}(\delta t)$ for the source (no storage) and for the stored and re-emitted photons, both as a function of the pump power. For this measurement, the cross-correlation for the source was measured with a matching FP etalon in the 794 nm photon arm and, hence, only true coincidences were recorded. In this case, the $g_{12}^{(2)}(0)$ for the non-stored photons agrees within the experimental uncertainty with that of the stored photons. Note that this measurement was taken at the highest pump-power, which was also used for the $g_{12}^{(2)}(0)$ measurement shown in Fig. 2 of the main text.

The $g_{12}^{(2)}(0)$ values for the stored photons in Fig. A.5 also highlight the influence of background noise in our measurement. Without storage, $g_{12}^{(2)}(0)$ follows the expected inverse dependence on pump power – the smaller the pump power the larger $g_{12}^{(2)}(0)$. For the stored photons, however, the trend is oppositve, and $g_{12}^{(2)}(0)$ decreases as the pump power is reduced. This is because the coincidence rate after storage is small enough such that the background noise starts to dominate.

QUBIT ANALYSIS

Free-space interferometers with path-length differences identical to that of the pump interferometer and controlled relative phases were used to project individual qubits of the entangled state onto superposition states $\frac{1}{\sqrt{2}}(|e\rangle + e^{i\theta}|\ell\rangle$, where the phase θ was established as described in Fig. A.4. Apart from the active phase stabilization described above, the phase of the interferometers was passively stabilized by temperature controlling its enclosure. Alternatively, to measure qubits in the canonical bases, i.e. $|e\rangle$ and $|\ell\rangle$, the interferometers were replaced by a short fibre, and the photon arrival time was recorded.

To reconstruct two-photon density matrices, we measured several bipartite projectors composed of individual projections onto eigenstates of combinations of the Pauli operators σ_x, σ_y and σ_z. In the case of temporal mode encoding, this is done by means of interferometers with suitably-chosen phases (for σ_x and σ_y), or delay lines (for σ_z), respectively.

ENTANGLEMENT OF FORMATION, PURITY AND FIDELITY CALCULATION

The entanglement of formation is defined as

$$E_F(\rho) = H\left(0.5 + 0.5\sqrt{1 - C^2(\rho)}\right), \tag{A.4}$$

where $H(x) = -x\, log_2(x) - (1-x)\, log_2(1-x)$ and $\mathrm{C}(\rho)$ is the concurrence, which is defined as

$$C(\rho) = \max\{0, \lambda_1 - \lambda_2 - \lambda_3 - \lambda_4\}.$$

The λ_i's are the eigenvalues of the reconstructed density matrix shown in Fig. 3 of the main text.

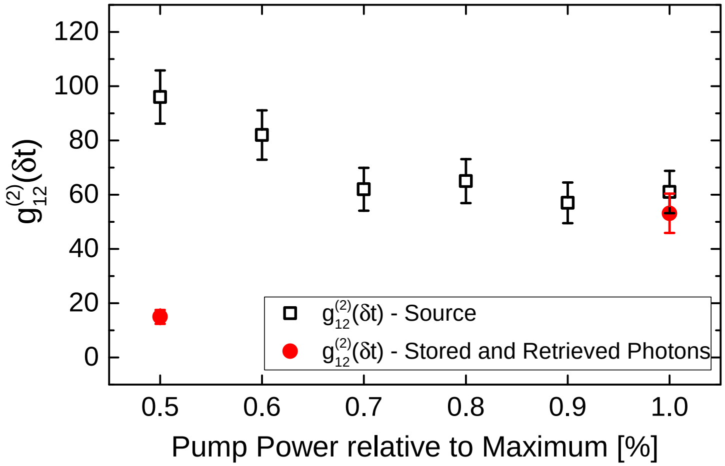

Figure A.5: Measured $g^{(2)}_{12}(\delta t)$ for different values of the pump power. As expected, the value of $g^{(2)}_{12}(\delta t)$ for the source increases with decreasing pump power. However, to achieve a higher SNR, we used the highest available pump power throughout all measurements involving quantum memories.

The fidelity between ρ and σ is

$$F(\rho,\sigma) = \left(\mathrm{Tr}\left(\sqrt{\sqrt{\rho}\sigma\sqrt{\rho}}\right)\right)^2 \tag{A.5}$$

and the purity of a state ρ is

$$P = \mathrm{Tr}(\rho^2). \tag{A.6}$$

BELL-INEQUALITY TEST

The four correlation coefficients that compose S in Eq. 2 of the main text were measured as

$$E(a,b) \;=\; \frac{C(a,b) - C(a,-b)}{C(a,b) + C(a,-b)} \tag{A.7}$$

using projectors $a = \sigma_x$, $a' = \sigma_y$, $b = (\sigma_x + \sigma_y)$, and $b' = (\sigma_x - \sigma_y)$. As explained in more detail in [7], these projections correspond to detecting photons in specific outputs of interferometers with appropriately chosen phases. Tables A.2 and A.3 present the individual values acquired for Quantum State Tomography and CHSH-Bell inequality tests, respectively.

λ_{signal} [nm]	λ_{idler} [nm]	η_{TM}	η_{ER}	$\eta_{\text{TM}} \times \eta_{\text{ER}}$
795.15	1534.05	0.93%	0.50%	0.0095%
794.85	1535.17	1.87%	0.48%	0.0182%
794.68	1535.80	2.00%	0.50%	0.0200%
794.55	1565.29	1.49%	0.49%	0.0148%

Table A.1: Efficiency versus wavelength for pairs of wavelengths available in the SPDC source.

	$\sigma_z \otimes \sigma_z$	$\sigma_z \otimes \sigma_x$	$\sigma_z \otimes \sigma_y$	$\sigma_x \otimes \sigma_z$	$\sigma_x \otimes (\sigma_x + \sigma_y)$	$\sigma_x \otimes (\sigma_x - \sigma_y)$
P_{in} %	49.55±2.48	25.51±0.43	24.96±0.43	26.85±0.41	41.72±1.08	40.15±1.06
P_{out} %	48.21±2.48	25.00±5.89	24.49±7.07	25.00±5.10	40.91±6.82	42.50±10.31
	$\sigma_x \otimes \sigma_y$	$\sigma_y \otimes \sigma_z$	$\sigma_y \otimes \sigma_x$	$\sigma_y \otimes (\sigma_x + \sigma_y)$	$\sigma_y \otimes (\sigma_x - \sigma_y)$	
P_{in} %	23.82±0.57	27.15±0.42	25.22±0.59	8.66±0.58	40.39±1.05	
P_{out} %	22.22±5.56	25.26±5.16	26.39±6.05	6.82±3.94	40.00±8.16	
	$\sigma_z \otimes \sigma_{-z}$	$\sigma_z \otimes \sigma_{-x}$	$\sigma_z \otimes \sigma_{-y}$	$\sigma_x \otimes \sigma_{-z}$	$\sigma_x \otimes (\sigma_{-x} + \sigma_{-y})$	$\sigma_x \otimes (\sigma_{-x} - \sigma_{-y})$
P_{in} %	2.26±0.10	23.37±0.42	23.63±0.41	20.81±0.36	9.04±0.50	9.85±0.53
P_{out} %	2.30±0.54	26.39±6.05	26.53±7.36	27.08±5.31	9.09±3.21	7.50±4.33
	$\sigma_x \otimes \sigma_{-y}$	$\sigma_y \otimes \sigma_{-z}$	$\sigma_y \otimes \sigma_{-x}$	$\sigma_y \otimes (\sigma_{-x} + \sigma_{-y})$	$\sigma_y \otimes (\sigma_{-x} - \sigma_{-y})$	
P_{in} %	26.18±0.60	20.48±0.36	24.78±0.59	41.34±1.26	9.61±0.51	
P_{out} %	27.78±6.21	24.21±5.05	23.61±5.73	43.18±9.91	10.00±4.08	
	$\sigma_{-z} \otimes \sigma_z$	$\sigma_{-z} \otimes \sigma_x$	$\sigma_{-z} \otimes \sigma_y$	$\sigma_{-x} \otimes \sigma_z$	$\sigma_{-y} \otimes \sigma_z$	
P_{in} %	2.15±0.11	24.45±0.43	24.74±0.42	28.16±0.42	28.54±0.43	
P_{out} %	2.17±0.53	23.61±5.73	24.49±7.07	26.04±5.21	25.26±5.16	
	$\sigma_{-z} \otimes \sigma_{-z}$	$\sigma_{-z} \otimes \sigma_{-x}$	$\sigma_{-z} \otimes \sigma_{-y}$	$\sigma_{-x} \otimes \sigma_{-z}$	$\sigma_{-y} \otimes \sigma_{-z}$	
P_{in} %	46.03±0.41	26.66±0.44	26.67±0.44	24.18±0.39	23.83±0.39	
P_{out} %	47.31±2.46	25.00±5.89	24.49±7.07	21.88±4.77	25.26±5.16	

Table A.2: Joint-detection probabilities used for the reconstruction of the density matrices before (in) and after (out) storage.

FUTURE IMPROVEMENTS

In order to meet the benchmarks imposed by a spectrally-multiplexed quantum repeater[8], the storage time and storage efficiency have to be significantly improved for both the Tm- as well as the Er-doped memory.

The simplest implementation that allows one to achieve in principle unit storage efficiency is the use of an impedance-matched cavity[9] in which the reflectivity of the front mirror is determined by the round-trip loss in the rare-earth-ion doped crystal (the back mirror is assumed to be 100% reflective). This idea has very rapidly enabled increasing the quantum memory efficiency from a few percent to 56% [10]. In addition, the cavity also restricts the AFC bandwidth to the cavity linewidth, and spectral modes

	$a \otimes b$	$a \otimes b'$	$a' \otimes b$	$a' \otimes b'$
E_{in} %	60.59±1.34	64.39±1.27	-61.56±1.31	65.40±1.48
E_{out} %	68.73±11.29	63.03±8.22	-59.28±10.32	68.07±10.34

Table A.3: Correlation coefficients used to test the CHSH-Bell inequality.

to resonances spaced by the cavity free-spectral range. Calculations based on reasonable parameters for crystal length (e.g. 1 mm) and optical depth (e.g. two) result in an AFC width on the order of 1 GHz and memory channels spaced by around 5 GHz. These are values that allow the use of our current photon pair source without modification.

The optical coherence time—the fundamental limit to the storage in optical coherence—of the 795 nm transition in Tm:$Y_3Ga_5O_{12}$ (Tm:YGG) at 1.2 K approaches 500 μs, a factor of 15 more than in Tm:$LiNbO_3$ at the same temperature, with further improvements expected at lower temperature[11]. Paired with long-lived nuclear Zeeman levels, allowing for efficient optical pumping, and a simple sub-level structure, this makes this crystal a very promising memory candidate for a quantum repeater architecture based on spectral multiplexing[8]. In particular, when combined with an impedance-matched cavity, quantum state storage with 90% efficiency during a time on the order of 100 μsec – sufficient for an elementary link length in excess of 20 km – can be expected.

Er-doped Y_2SiO_5 (Er:YSO) features the longest optical coherence time of an impurity in a solid-state material, around 4.4 ms. This is an improvement by more than a factor of 10^4 compared to Er:SiO_2. However, as mentioned in the *Kramers and non-Kramers ions* section of the Methods, due to significant spin-spin and spin-lattice relaxation, a quantum memory has so far not been demonstrated in this crystal. But it has very recently been discovered that the application of a 6 T magnetic field across a ^{167}Er:Y_2SiO_5 crystal results in a hyperfine sub-level lifetime exceeding 1 min and an optical pumping efficiency of 95%, making it very promising for storage of telecommunication wavelength photons[1]. Hence, quantum state storage with 90% efficiency during a ms using optically-excited coherence should be possible. Moreover, instead of increasing the hyperfine sub-level lifetime in order to make AFC-based quantum memories possible, one could also reduce the excited level lifetime by means of the Purcell effect in a nanocavity[12].

Note that by replacing the currently used host materials $LiNbO_3$ and SiO_2 by YGG and YSO, no significant changes to the preparation procedure of the quantum memories are necessary. Furthermore, adding an impedance-matched cavity to the memory adds the requirement for proper mode-matching, which, however, constitutes no significant technical problem. It should also be noted that the spectral multiplexing scheme proposed in [8] does not rely on on-demand recall – reemission after a predetermined storage time (given by the inverse AFC teeth spacing), is sufficient. In short, our proof-of-principle demonstration can readily be translated into workable quantum technology by employing optimized host materials and suitable cavities.

REFERENCES

[1] M. Rančić, M. P. Hedges, R. L. Ahlefeldt, and M. J. Sellars, *Coherence time of over a second in a telecom-compatible quantum memory storage material,* Nature Physics **14**, 50 (2018).

[2] C. O’Brien, N. Lauk, S. Blum, G. Morigi, and M. Fleischhauer, *Interfacing superconducting qubits and telecom photons via a rare-earth-doped crystal,* Physical review letters **113**, 063603 (2014).

[3] X. Fernandez-Gonzalvo, Y.-H. Chen, C. Yin, S. Rogge, and J. J. Longdell, *Coherent*

frequency up-conversion of microwaves to the optical telecommunications band in an Er: YSO crystal, Physical Review A **92**, 062313 (2015).

[4] M. Afzelius, C. Simon, H. De Riedmatten, and N. Gisin, *Multimode quantum memory based on atomic frequency combs,* Physical Review A **79**, 052329 (2009).

[5] L. Redaelli, G. Bulgarini, S. Dobrovolskiy, S. N. Dorenbos, V. Zwiller, E. Monroy, and J.-M. Gérard, *Design of broadband high-efficiency superconducting-nanowire single photon detectors,* Superconductor Science and Technology **29**, 065016 (2016).

[6] A. Kuzmich, W. Bowen, A. Boozer, A. Boca, C. Chou, L.-M. Duan, and H. Kimble, *Generation of nonclassical photon pairs for scalable quantum communication with atomic ensembles,* Nature **423**, 731 (2003).

[7] E. Saglamyurek, N. Sinclair, J. Jin, J. A. Slater, D. Oblak, F. Bussieres, M. George, R. Ricken, W. Sohler, and W. Tittel, *Broadband waveguide quantum memory for entangled photons,* Nature **469**, 512 (2011).

[8] N. Sinclair, E. Saglamyurek, H. Mallahzadeh, J. A. Slater, M. George, R. Ricken, M. P. Hedges, D. Oblak, C. Simon, W. Sohler, *et al.*, *Spectral multiplexing for scalable quantum photonics using an atomic frequency comb quantum memory and feed-forward control,* Physical Review Letters **113**, 053603 (2014).

[9] M. Afzelius and C. Simon, *Impedance-matched cavity quantum memory,* Physical Review A **82**, 022310 (2010).

[10] M. Sabooni, Q. Li, S. Kröll, and L. Rippe, *Efficient quantum memory using a weakly absorbing sample,* Physical Review Letters **110**, 133604 (2013).

[11] C. W. Thiel, N. Sinclair, W. Tittel, and R. Cone, Tm^{3+}:$Y_3Ga_5O_{12}$ *materials for spectrally multiplexed quantum memories,* Physical Review Letters **113**, 160501 (2014).

[12] T. Zhong, J. M. Kindem, J. G. Bartholomew, J. Rochman, I. Craiciu, E. Miyazono, M. Bettinelli, E. Cavalli, V. Verma, S. W. Nam, *et al.*, *Nanophotonic rare-earth quantum memory with optically controlled retrieval,* Science **357**, 1392 (2017).

SUMMARY

The quantum internet, when finally deployed, will enable a plethora of new applications such as theoretically proven secure communication and networked quantum computing, much the same as its classical counterpart whose development began back in the 1990’s. The task of creating a globe-spanning quantum network, however, is proving a rather difficult task due to the detrimental effect of loss on photon transmission. This problem can in theory be solved using so-called quantum repeaters. In one of the most well-known configurations, the long-distance span is divided into smaller segments—so-called elementary links—at whose ends pairs of entangled photons are generated. One photon per pair is stored in a quantum memory, and the second member is transmitted via optical fiber to a remote measurement stations positioned at the centre of the segment. There, a joint measurement of the two photons, one from each end, then heralds the distribution of entanglement between the two quantum memories, i.e. heralds entanglement over the elementary link. In the final step, all neighbouring links are combined via a second joint measurement, and end-to-end entanglement is created.

The fact that transmission loss in optical fiber is smallest around 1550 nm wavelength has affected classical communication technology, and, for the same reason, it puts constraints on quantum communications. In particular, it compels the development of quantum memories that are compatible with telecommunication wavelength.

Large ensembles of cryogenically cooled rare-earth ions (REI) doped into solid-state host materials are promising material candidates for building optical quantum memories due to their unique properties. These include long optical and spin coherence times, absorption lines with large inhomogeneous broadening, and their strong coupling to light. Even more appealing is the fact that erbium, a rare-earth element, exhibits an absorption window at telecommunication wavelength as well as some of the longest optical coherence times, offering a great starting point for the development of a telecom-compatible quantum memory. Furthermore, the well-known atomic frequency comb (AFC) quantum memory protocol can take advantage of its broad absorption profile, and, in turn, produces broadband quantum memories. Therefore, erbium-based quantum memories relying on the AFC protocol can potentially yield quantum memories with the following features: telecom-compatibility; broadband operation; high efficiency; and long storage time.

A necessary step towards unlocking the sought-after potential of erbium-based quantum memories is the spectroscopic investigation of host materials doped with this REI. The work reported in this thesis includes several such studies, as well as proof-of-principle demonstrations of key elements of a quantum repeater using erbium-doped materials. In particular, after a short introduction in chapter 1, chapter 2 elaborates on the important features of REIs in view of quantum memory and introduces several useful and widely-employed spectroscopic tools. The goal is to prepare the readers for the spectroscopic investigations described in chapters 3 and 5. In addition, chapter 2 discusses different quantum memory protocols and their characteristics to provide the necessary background for the quantum storage demonstrations reported in chapters 4 and 6.

In chapter 3, I describe experimental studies of coherence properties of an erbium-doped fiber using two well-known spectroscopic techniques, namely the two-pulse photon echo and the three-pulse photon echo. These studies revealed that the main limitation to long coherence times—and hence storage time—is caused by intrinsic features of the amorphous (glassy) host such as two-level-systems (TLS)s. The investigation also includes the development of a theoretical model to predict the behaviour of TLSs with respect to temperature and magnetic field. The second spectroscopic study, reported in chapter 5, concerns the experimental investigation of population relaxation between ground-state Zeeman sub-levels in an erbium-doped lithium niobate crystal waveguide. We found the longest Zeeman level lifetimes among reported erbium-doped crystals. Furthermore, we have created AFC structures using these levels and observed significant residual absorption, which would limit the storage efficiency. We conjectured this detrimental effect to be due to laser-induced excitation of TLSs, which leads to population relaxation.

Chapter 4 reports on entanglement distribution between hybrid quantum systems, i.e., between quantum memories based on two different REIs, namely erbium and thulium. Most importantly, we have observed non-locality between two photons after storage and re-emission from these different solid-state quantum memories. In chapter 6, we have demonstrated quantum storage of single, heralded telecommunication photons using an erbium-doped lithium niobate crystal waveguide. Non-classicality was verified using the second-order cross correlation function.

In short, we have demonstrated key properties of Er-based quantum memory such as entanglement and non-locality. However, our investigations have also revealed limitations of the studied erbium-doped materials, in particular small storage efficiencies and short storage times. We anticipate that our findings will guide future work with erbium-doped materials, including with other crystals, and with crystals within a different environment such as a nano-sized cavity or magnetic fields of several Tesla. We believe that it will be possible to find conditions under which the exciting goal of quantum memory for telecommunication-wavelength photons can be reached.

SAMENVATTING

Het kwantuminternet, wanneer het gelanceerd wordt, zal een overvloed van applicaties met zich mee brengen. Zoals beveiligde communicatie, dat theoretisch bewezen is, en kwantum netwerk berekeningen. Dit is vergelijkbaar met zijn klassiek tegenhanger, waar de ontwikkelingen al in de jaren 90 zijn begonnen. Het doel om een wereldwijde kwantumnetwerk te bouwen blijkt gecompliceerd te zijn door het ongewenste verlies van uitgezonden fotonen. Dit probleem kan in theorie worden opgelost met zogenaamde kwantum herhalers. In één van de meest bekende configuraties wordt de lange afstand opgebroken in kleinere segmenten, de zogenaamde elementaire link, waar aan elk uiteinde een verstrengelde foton paar wordt gegenereerd. Eén foton per paar wordt opgeslagen in een kwantum geheugen en elk andere foton wordt overgedragen door een optische fiber naar een afgelegen metingstation, dat gepositioneerd is op het middelpunt van het segment. Vervolgens, wordt daar een gezamenlijke meting van de twee fotonen, die elke van een ander uiteinde komen, dat kondigt de verdeling van de verstrengeling tussen twee kwantum geheugens aan. Dit is beter bekend als aangekondigde verstrengeling over de elementaire link. In de laatste stap worden alle naastgelegen linken aan elkaar verbonden door een tweede gezamenlijke meting. Hiermee is een complete verstrengeling van eind tot eind gecreëerd.

Het feit dat het overdragingsverlies in een optische fiber het kleinst is rond een golflengte van 1550 nm, beïnvloed de klassiek communicatie technologie. Dit geldt ook voor kwantum communicatie. De ontwikkeling van kwantum geheugens wordt hierdoor gedwongen om het met de telecommunicatie golflengte te verenigen.

De meest veelbelovende kandidaten voor het bouwen van een optische kwantum geheugen zijn grote verzamelingen van cryogeen gekoelde zeldzame aarde-ionen (ZAI) gedoteerd in vaste stof materialen, door hun unieke eigenschappen. Deze hebben lange optische en spin coherentietijd, absorptie lijnen met grote inhomogene verbreding en sterke koppeling met licht. Een interessantere feit is dat erbium, een zeldzame aarde-ionen , heeft een absorptie interval dat waar de telecommunicatie golflengte onder valt. En het heeft ook één van de langste optische coherentietijd, dit biedt een veelbelovend start punt voor het ontwikkelen van een verenigbare telecom kwantum geheugen. Bovendien, de welbekende atomische frequentie kam (AFK) kwantum geheugen protocol kan gebruik maken van zijn brede absorptie profiel en kan vervolgens breedband kwantum geheugens produceren. Dus, op erbium gebaseerde kwantum geheugens die afhankelijk zijn van de AFK protocol hebben de potentie om kwantum geheugens te maken met de volgende eigenschappen: vereniging met telecom golflengtes, werking op breedband, hoge efficiëntie en lange opslag tijd.

Een essentiële stap naar het ontgrendelen van de potentie van erbium gebaseerde kwantum geheugens is het spectroscopisch onderzoeken van materialen gedoteerd met deze zeldzame aarde-ionen (ZAI). Deze thesis bevat verscheidene onderzoeken en ook het bewijzen en uitvoeren van sleutel elementen van een kwantum herhaler gemaakt van erbium gedoteerde materialen. Na een korte introductie in hoofdstuk 1, ligt de nadruk in hoofdstuk 2 vooral op de belangrijke eigenschappen van ZAI in het perspectief van kwantum geheugens en introduceert verschillende handige en wijd gebruikte spectroscopische technieken. Het doel is om de lezer voor te bereiden voor spectroscopische onderzoeken die beschreven worden in hoofdstuk 3 en 5. In hoofdstuk 2 wordt ook gediscussieerd over verschillende kwantum geheugen protocollen en zijn karakteristieke eigenschappen voor de benodigde achtergrondkennis van kwantum geheugen demonstraties, die worden beschreven in hoofdstuk 4 en 6.

In hoofdstuk 3, beschrijf ik experimentele onderzoeken naar coherentie eigenschappen van erbium gedoteerde fiber met behulp van twee bekende spectroscopische technieken, namelijk de twee-puls foton echo en de drie-puls foton echo. Uit deze studies zijn aangetoond dat de voornaamste limitatie tot lange coherentietijd, en dus ook lange opslagtijd, wordt veroorzaakt door intrinsieke eigenschappen van de vormloze materiaal zoals het twee-level-systeem (TLS). Het onderzoek bevat ook de ontwikkeling van een theoretisch model om het gedrag van TLSs onder invloed van temperatuur en magnetisch veld te voorspellen. Het tweede spectroscopisch onderzoek, in hoofdstuk 5, gaat over experimenteel onderzoek naar populatie relaxatie tussen grondtoestand Zeeman levels in een erbium gedoteerd lithium niobate kristal met een golfgeleider (waveguide). We hebben de langste Zeeman level levensverwachting gevonden in vergelijking met eerder gevonden resultaten van erbium gedoteerd kristal. Bovendien, hebben wij een AFK structuur gecreëerd met behulp van deze levels en een significante overgebleven absorptie, dit limiteert de opslag efficiëntie. Wij vermoeden dat dit schadelijke effect veroorzaakt wordt door de laser-geïnduceerde excitatie van TLSs, dit zet de populatie relaxatie in werking.

In hoofdstuk 4 wordt voornamelijk vermeld over verstrengeling distributie tussen hybride kwantum systemen, i.e., tussen twee verschillende ZAI's gebaseerde kwantum geheugens, namelijk erbium en thulium. Het meest belangrijke dat we hebben geobserveerd is non-lokaliteit tussen twee fotonen na het opslaan en heruitzenden van de verschillende vaste-stof kwantum geheugens. In hoofdstuk 6 hebben wij kwantum opslag van enkele aangekondigde telecommunicatie fotonen tussen erbium gedoteerd lithium niobate kristal met golfgeleider aangetoond. Kwantum correlatie, tweede orde kruis correlatie functie, is geverifieerd.

In het kort, wij hebben sleutel eigenschappen van Er gebaseerde kwantum geheugens zoals verstrengeling en non-lokaliteit aangetoond. Echter, onze onderzoeken hebben ook limitatie van de bestudeerde erbium gedoteerde materialen, voornamelijk kleine opslag efficiëntie en korte opslag tijden laten zien. Wij anticiperen dat onze vindingen toekomstig werk met erbium gedoteerde materialen, inclusief met andere kristallen en met kristallen in een andere omgeving, zoals op nanoschaal holte of magnetische velden van verscheidene Tesla zal gidsen. Wij geloven dat het mogelijk is om de juiste omstandigheden te vinden waaronder het fantastische doel van kwantum geheugen voor fotonen met telecommunicatie golflengte kan worden bereikt.

ACKNOWLEDGEMENTS

First and foremost, I would like to thank *Allah* for giving me strength, knowledge, and perseverance to accomplish my studies.

I would like to express my sincere appreciation and gratitude to those who have guided, helped, supported, and accompanied me during the course of my PhD. I shall be forever indebted to your contributions and you will never be forgotten.

I dedicate this dissertation to my mother, *Maryam*, for all her love, sacrifice, and selflessness from my childhood until now. Love you mom.

LIST OF PUBLICATIONS

4. *Persistent atomic frequency comb based on Zeeman sub-levels of an erbium-doped crystal waveguide.*
   M. F. Askarani, T. Lutz, M. G. Puigibert, N. Sinclair, D. Oblak, and W. Tittel, arXiv:1907.07780v2.

3. *Entanglement and no-locality between disparate solid-state quantum memories mediated by photon.*
   M. G. Puigibert*, **M. F. Askarani***, J. H. Davidson, V. B. Verma, M. D. Shaw, S. W. Nam, T. Lutz, G. C. Amaral*, D. Oblak, and W. Tittel, arXiv:1905.08184.

2. *Storage and reemission of heralded telecommunication-wavelength photons using a crystal waveguide.*
   M. F. Askarani, M. G. Puigibert, T. Lutz, V. B. Verma, M. D. Shaw, S. W. Nam, N. Sinclair, D. Oblak, and W. Tittel, Phys. Rev. Applied **11**, 054056 (2019).

1. *Optical decoherence and spectral diffusion in an erbium-doped silica glass fiber featuring long-lived spin sublevels.*
   L. Veissier*, **M. Falamarzi***, T. Lutz, E. Saglamyurek, C. W. Thiel, R. L. Cone, and W. Tittel, Phys. Rev. B **94**, 132 (2016).

---

*Equally contributing authors

CURRICULUM VITÆ

Mohsen FALAMARZI ASKARANI

23-01-1989	Born in Esfahan, Iran.

EDUCATION

2003–2007	High School *Harati, Esfahan, Iran*
2007–2011	Bachelor of Science in Physics *University of Mazandaran, Iran*
2011–2013	Master of Science in Physics *Sharif University of Technology, Iran* Thesis: Investigation on optical properties of photonic quasi-crystal fiber Supervisor: Prof. dr. A. Bahrampour
2015–2018	PhD candidate in Physics *University of Calgary, Canada* Thesis:Telecom-wavelength quantum memories in rare earth ion-doped materials for quantum repeaters Promotor: Prof. dr. W. Tittel
2018–2019	Doctorate in Physics *Delft University of Technology, The Netherlands* Thesis: Telecom-wavelength quantum memories in rare earth ion-doped materials for quantum repeaters Promotor: Prof. dr. W. Tittel Co-promotor: Prof. dr. R. Hanson